ELECTROMICROFILTRATION FOR SEPARATION OF MINERAL PARTICLES IN DAIRY PROCESSING

A thesis presented in partial fulfillment of the requirement for the degree of

MASTER OF TECHNOLOGY

in

FOOD ENGINEERING

In the Institute of Food, Nutrition & Human Health,

Massey University, Albany campus,

New Zealand

By

Frank G.uan Feng Qin

June 1999

Abstract

Electromicrofiltration, where an external electric field is imposed on a traditional microfiltration unit, has been studied for several years. Reports in this field have covered the filtering separation of china clay, kaoline, anatase and a surfactant from water. Some recent investigations concerning the utilization of electromicrofiltration for bioseparations has led to a growing interest in applying this method to dairy processing. The objective of this work was to explore the characteristics of an electromicrofiltion unit and examine the potential of utilizing this for mineral (calcium phosphate) removal in the dairy industry. Two stainless steel membranes with nominal pore sizes of 5μm and 25μm, respectively, were used in this study. This material provides the membrane with some unique properties such as electrical conductivity; resistance to high pressure operation and backflushing; and resistance to chemical cleaning agents. Alamin particles, a by-product separated from whey, was used as the primary feed particle. The average particle size is about 5μm and the chemical composition is mainly calcium phosphate. Another particle, calcite (calcium carbonate), was used for comparison. Experiments were performed on a laboratory electromicrofilter (the tubular membrane dimension is 380mm in length and 13.5mm in diameter) in which the voltage(0-50V) and current (0-3A), transmembrane pressure (0-250kPa), and crossflow velocity (0-3m/s) could be measured and controlled.

Between 20% ~ 100% transient improvement in permeate flux was obtained when an electric field was applied. For example, the permeate flux increased from 120LMH to 165LMH at the condition of 50kPa transmembrane pressure, 36V/cm electric field strength and 2.28m/s crossflow velocity, in which the membrane was negatively charged and the solution was pH=7. This polarity was used because the zeta potentials for most of the colloid or particulate material in the dispersed system are generally negative in the normal pH range (pH=4~8). The permeate flux gain was largely voltage and particle concentration dependent. The principle of this was further studied and two mechanisms influencing flux were identified: (1) the electricstatic repulsion to the particles or colloids by the charged membrane; and (2) the displacing effect of the cathodic gas bubble on the deposited particles. Microscopic

examination showed that the electrophoretic speed of Alamin particles around 1μm in size under 36V/cm electric strength was ~43μm/s. However, continuous application of the electric field was found raised the permeate to pH 11 or higher; this appeared to reduce the solubility of calcium salt in the solution, and eventually caused more severe fouling as fine particles precipitated and obstructed the membrane. Therefore pulsatile application of electric field is recommended. On the other hand, formation of the gas bubbles caused an additional false permeate increase of about 25(LMH) for a 1A membrane current in this electromicrofiltration unit.

Using a positively charged membrane, in contrast, acidified the permeate to pH 3~3.5 and resulted in dissolution of the deposited calcium salts. For this reason the steady state permeate flux was improved. For example, the permeate flux for the Alamin solution (0.7%w/v) was 103(LMH) at 100 mins after filtration start if no electric field was applied, but at the same condition the permeate flux was 190(LMH) if the membrane was positively charged at 33V/cm field strength. However, the anodic corrosion was evident if chloride ion (Cl^-) was proved above a minimal valum in the solution. This hamful aspect had been emphsised in this research, and the use of a titanium anode is suggesed to avoid corrosion in the future studies. Moreover, anodic oxidation and its potential to change the chemical nature of the filtrated substance must be take into consideration when applying electriofiltration in a bioseparation processes.

A hydrodynamic analysis revealed that the flow pattern over the whole membrane module was fully developed turbulent flow at 2.28m/s crossflow velocity. The thickness of the laminar sub-layer on the membrane wall was about 81μm, which is roughly one order larger than the mean particle size in this study. The drag force acting on a deposit particle was estimated as 2.33×10^{-9} (N), which is 230 times higher than the static electric field force, and the electric field repulsing force acting on a deposit mean size particle is 9 times higher than the particle self weight. The sum of these forces inhibited the particle from depositing on the membrane surface. Considering that the nominal membrane pore sizes used (5μm and 25μm, respectively) was relatively large (around 0.2-1μm only for normal MF) and the particle size

distribution, the fouling mechanism is more likely to be pore plugging rather than the cake formation on the surface.

Investigation of cleaning methods showed that the effectiveness of backflushing was basically pressure dependent. A 30kPa backflushing pressure restored 85% of filtration performance for the 25μm membrane; and a stop-and-restart operation(in which about 15mm H_2O column backpressure was provided by the permeate) restored approximately 60% of its filtration performance. However over 250kPa backflush pressure was needed to restore 85% of filtration performance on the 5μm membrane. Use of backflushing can greatly reduce the consumption of chemical cleaners and it is recommended the membrane be charged as an anode when performing the backflushing operation. This can be an effective alternative to acid cleaning if the backflushing water has less than 0.1ppm chloride ion content.

Lastly the formation of the cathode deposit on the membrane as the electric field was applied was observed to act as a 'formed-in-place' dynamic filtering layer, and its potential application may be worth investigation in a future study.

Keyword: membrane; sintered stainless steel; microfiltration; electrofiltration; separation; electric field; dairy processing

Acknowledgments

First and foremost I wish to thank my supervisor John Mawson for his direction and encouragement over the last one and half years. His scrupulousness and experience benefited me a lot.

I also wish to acknowledge Industrial Research Limited (NZ) for the sponsorship of this project and my study.

Designing and establishing a suitable experimental apparatus is an important job for scientific research. The equipment used in this study was setup by the engineers in Messay University; the sintered stainless steel membranes were provided by Industrial Research Limited (NZ); and the filtration substance — 'Alamin' was supplied by the NZ Dairy Board. I would like to thank all those people who had given so much assistance. They are greatly appreciated.

This research work was carried out in the microbiology laboratory of Massey University, Albany campus. The laboratory technician Miss Joann Smith gave a lot assistance for the routine laboratory work. Dr. Jayantha Wimalasena, the technician of the chemistry laboratory, helped me obtain chemicals when needed, and Mr. Joe Wang, the technician of the Physics Department, used his skill to fix problems and give advice on what I planed to do. These impacts benefited me a lot. The research would have not been completed without their help.

I would like to thank Mr. John Evans for his help and communication to improve my understanding to the work and study environment.

I also wish to thank my friend Mr. Anthony W.Y. Wu and his wife Ms. Dang Ming Chen for their time, understanding and encouragement to my study.

Finally, to my wife Wanny and my daughter Jenni. Without their constant support, love and encouragement during my study, this thesis would never have been completed.

Table of Contents

List of Figures

List of Tables

1. Introduction

1.1. Brief Review of The Research and Development of Membrane Separation

In membrane separations, the characteristics of the membrane itself are always central to the performance of the process. The membrane must be semi-permeable, that is permeable to the solvent or some solutes, but present a barrier to other mixture components. Pressure-driven membrane separation comprises a continuum of processes designed to separate particles or solutes of different sizes by utilization of membranes containing appropriately sized pores. Scientific research on membranes commenced over 160 years ago[1]. In 1823, Dutrochet gave a correct explanation of osmosis and dialysis, and in 1867 and 1877 Traube and Pfeffer made the first quantitative studies on osmosis. At about the same time, Graham discovered that oxygen-enriched air can be produced by arranging a membrane between a reservoir of pressurized air and another reservoir of unpressurized air. Although artificial semi-permeable membranes had been made before the middle of last century, their low initial permeate flux, poor selectivity, liability to fouling and high cost meant this technology did not find application in industry until relatively recently.

On a technical scale[2], membranes were initially used in very few processes, for example, for the recovery of NaOH by dialysis from waste water containing hemicellulose from the viscose-rayon industry. Another well known example of an early large-scale application of membrane processes is the separation of U^{235} , U^{238} and UF_6 by gas permeation using porous ceramic membranes. Many membranes used in the early stage of developing the technology were homogeneous in structure (Figure 1-1).

The situation changed rapidly after the early 1960's, when Loeb and Sourirajan developed a new polymeric membrane with higher permeate flux[3]. These possessed an asymmetric structure with a dense skin layer on top and a porous backing matrix beneath. Pore sizes of the active skin layer were around 100 nm, and the thickness was about 0.2~0.5 μm. The backing porous layer was about 50~100 μm in thickness and 0.1~1 μm in pore size. Since the active skin was very thin, resistance to the flow was lower, and its surface characteristics restricted pore plugging (Figure 1-2). These asymmetric membranes were usually made by the phase-inversion method[4]. The first industrial use of asymmetric membranes was for sea water

desalination by reverse osmosis in the early 1960's[3] , which proved to be efficient and energy-saving. This was considered to be a breakthrough in membrane science and technology and since then all industrially developed nations have started major research programs for the development of high-performance membranes and modules. Progress made in sea and brackish water desalination, followed by the successful transfer of the experience gained to other small- and large-scale separation processes, has resulted in membrane processes now being commonly regarded as a standard unit operation in many industries [5, 30].

In recent years some new types of membranes, such as the composite membrane, were developed and attracted wide attention. The composite membrane is a modified form of asymmetric membrane, which usually comprises a very permeable UF membrane with a very thin, highly-selective dense layer of anther polymer applied on top of it (Figure 1-3).

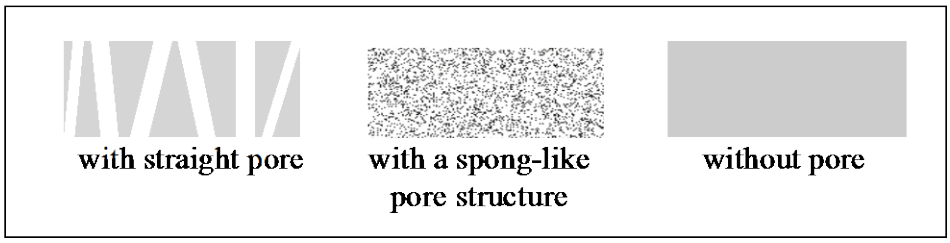

Figure 1-1. Schematic diagram of homogeneous membrane

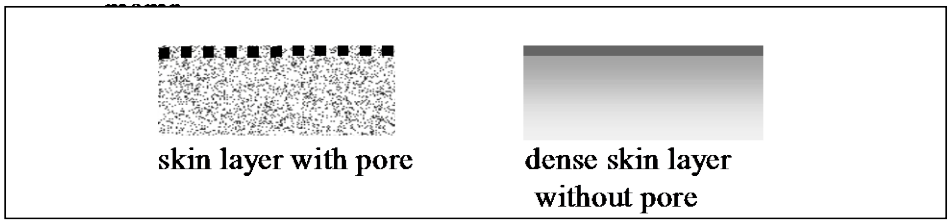

Figure 1-2. Schematic diagram of asymmetric membrane

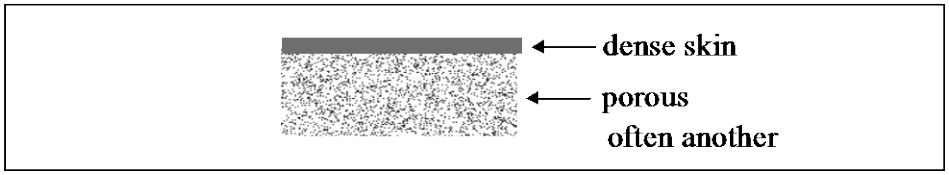

Figure 1-3. Schematic diagram of a composite membrane

Another recent development in membrane technology is the application of inorganic membranes in food and bioprocessing. These can be considered the third generation of membranes for pressure driven filtration after the cellulose acetate and other polymer (mainly polysulfone) membranes. Porous inorganic membranes are made from powders which are

sintered to give them the unique construction and rigidity. Today, all the industrial inorganic membranes are of a tubular configuration with different hydraulic diameters and support layer thicknesses. The membranes are asymmetric and are composed of a thick sintered porous structure which serves as a mechanical support for the thin filtering layer. The filtering layer may be made of the same material as the support or from a different material (composite membrane). The surface layer of inorganic membranes for MF and UF is made from a powder suspension, while for NF and some UF membranes this is a sol-gel layer. The membrane composition , the sintering process, and the tubular design make inorganic membranes highly resistant to organic and inorganic solvents, high pressure (15~40 bar) and high temperature (>200°C). This resistance allows the use of aggressive oxidizing cleaners and vapour sterilization. These characteristics make inorganic membranes are appealing to the food and biotechnology industries, despite their present somewhat limited range of pore sizes.

It was almost two decades after Loeb and Siurirajan[3] presented their desalination membrane when the first account on an industrial application of an inorganic membrane for the concentration of milk proteins for cheese-making by UF was published[6]. During this time, researchers investigated the flux decline phenomena of organic membranes and developed much filtration theory and also established the terms used to describe flux and fouling. The same concepts were later justifiably adopted to describe the behaviour of inorganic membranes, as operation with inorganic membranes does not differ very much from working with polymeric membranes, except for the lack of membrane compaction.

Although these inorganic membrane have some disadvantages compared to polymeric ones, especially with respect to the requirement of high pumping capacities (as tube bores are relative large), large floor area and high price per square meter of membrane, they find competitive uses in the processing of various dairy streams[28]. According to Crull[19] , if the market is categorized according to the three main types of membranes, that is, polymeric, carbon composite and alumina, then the ceramic membranes appear competitive to polymeric ones in total process cost (total investment plus operation), especially at the higher pore sizes (that is, MF and some UF operations) and in comparison with carbon membranes.

Other inorganic membrane types are also available, for example, the formed-in-place (FIP) membrane is based on a metallic or ceramic porous support. A filtering layer is formed on this

porous support from a metal ion solution by depositing the ion on the surface while circulating the solution through the filtration module. For example, a ZrO_2 dynamic layer is formed in a two-step process. In the first step a metal hydrous oxide layer is filtered onto a porous support from a dilute solution of the salt of the Zr(IV) ion. In the second step, a dilute solution of poly(acrylic acid) is filtered on the hydrous oxide layer beginning at pH 2 and increasing the pH to 7[19]. Another membrane made of anodized γ-alumina in a flat-sheet 'capillary pore structure', 45~60 μm thick and a narrow pore size distribution of 0.2 μm has been used for experimental purposes[25,26]. But neither the formed-in-place membranes nor the corrosion liable γ-alumina units have not yet found uses in food or dairy industry.

However, two kinds of stainless steel membrane module incorporated in the "Micro-Steel" and "Scepter" caustic recovery system have found application in dairy industry [36] and textile industry [37], respectively. The former was designed to remove suspended solid from clean-in-place (CIP) solutions used for evaporators and other processing equipment. Typical fluxes are 190LMH for 80% recoveries and power requirements are 20- 25 hp. A dairy plant using only 100 gal per day of 50% caustic could see a payback period of less than a year. The later has been used in several textile mills to recover and reuse 90 – 95% of the caustic solution, resulting in significant saving in chemicals, energy, and waste treatment cost. At a caustic price of $400/ton, a 14,000 gal per day system can save $300,000 per year.

Power metallurgy is used to produce porous stainless steel (SS). For the Scepter stainless steel membrane mentioned above, which is a tubular module developed by Graver Separation, Inc., titania (TiO_2) is sintered on the porous SS on the inside of the tubes to form a permanent MF membrane of about 0.1μm or larger pore size. If necessary, the TiO_2-SS composite can serve as the base for the manufacture of UF or NF membrane by using the formed-in-place (FIP) technique. For example, zirconium oxide or other food-grade polymers result in UF membrane with an MWCO of 20,00-80,000, depending on the chemical.

1.2. Project Background

The fact that particles in almost all colloidal or dispersed systems are more or less electrically charged has raised interest in electrofiltration based on MF and UF. In these processes an electric field is applied to enhance the separation through the mechanism of rejecting colloids at the membrane surface. For this purpose some membrane modules were specially designed and made to meet the need of electric introduction and insulation.

In fact interest in utilizing an external electric field to enhance membrane separation dates back to 1960's when Bier filed a patent for an apparatus suitable for continuous electrophoretic separation, purification and concentration of colloidal solutions [27]. Recent work at Massey University in which Reeve studied the electrofiltration processes by employing a sintered stainless steel membrane achieved some promising results [15]. This work lead to further interest in the application of electrofiltration in dairy processing. The current project was a natural continuation of this research , and was sponsored by Industrial Research Limited (NZ) [29].

2. Literature Review

2.1. Research and Development of Electromicrofiltration

Since most fine particulate substances acquire a surface electric charge when in contact with a polar medium, an electric double layer (EDL)[7] is formed in the vicinity around the particle surface (Figure 2-1). Electrofiltration makes use of this electrokinetic property to increase the rate of filtration by imposing a DC electric field over the region of the separating surface.

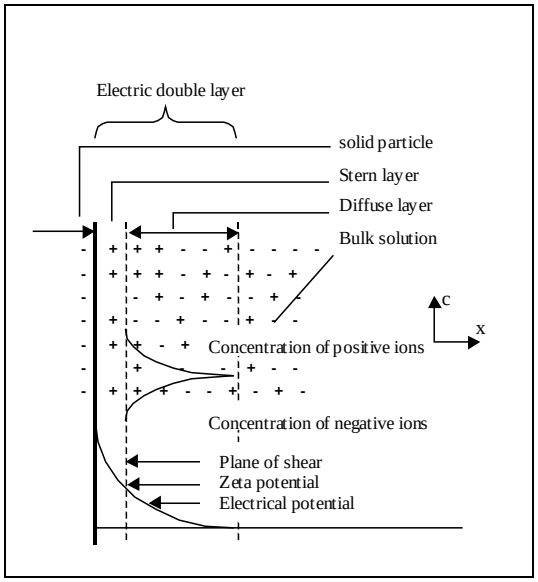

Figure 2-1. Diagram of the electric double layer adjacent to a negatively charged surface

Early this century Gouy and Chapman postulated that diffuse layers of ions exist near solid surfaces and extend into the liquid phase [7]. When the particle moves relative to the liquid, the innermost layer of ions moves with it; at the plane of shear the so called zeta potential exists and its magnitude depends on several factors. In general, the greater the charge and the concentration of the counter-ions the lower the zeta potential, but counter-ions of high charge can cause complete charge reversal. The zeta potential, which can be measured with a commercial zeta meter, characterizes the effectiveness of the particles in repelling each other or in being repelled by the charged membrane. While at the microscopic level a particle's charge influences the distribution of nearby ions; at the macroscopic level, as the size of the particles decrease, the repulsion/weight ratio increases rapidly (which stabilizes the dispersed system as a result), and filtration or separation of particles from a liquid generally becomes more difficult.

Zeta potential also affects the interaction between the particle and membrane based on the electrostatic attraction or repulsion (although there are many other factors which can influence the deposition of particles or molecules onto the membrane).

Electrofiltration is in fact a modification of the traditional dead-end filtration or cross-flow filtration, which provides an additional driving force for particle separation, i.e. electrophoresis under the influence of an applied electric field. This field can be introduced to the existing filtration processes by proper design of the membrane model. When the field is applied to MF or UF, the process is called electromicrofiltration (EMF) or electroultrafiltration (EUF), respectively. Table 2-1 shows some typical membrane processes and a simplified representation of electrofiltration in a dead-end filter is shown in Figure 2-2.

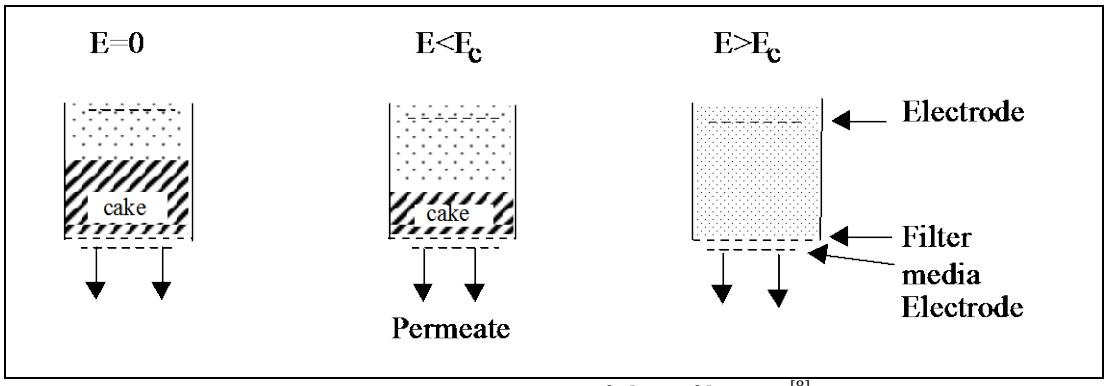

Figure 2-2. Representation of electrofiltration [8]

Table 2-1. Some important membrane separation processes*

Processes	Diagrams	Permeating substance	Driving force	Retention
Osmosis	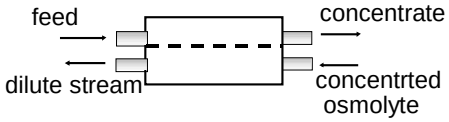	water	Concentration Difference	solute
Dialysis	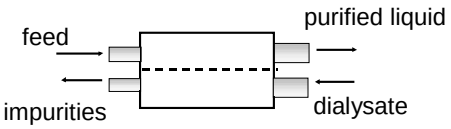	ions and low molecules (e.g. urea)	Concentration Difference	M.W.>1000 solute or suspension
Electro-dialysis	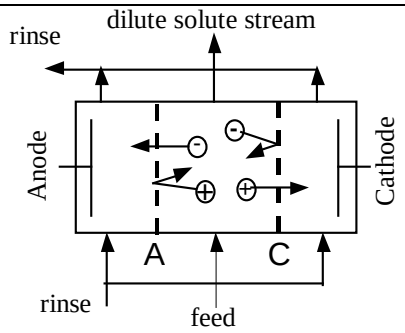	Ions	Electro-Potential (1~2V/cell)	non-ions and large molecules
Reverse osmosis	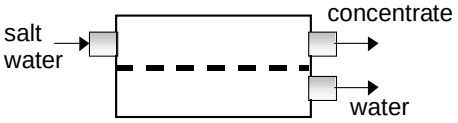	Water	Pressure (1~8Mpa)	solute and suspension M.W.>100
Nanofiltration				M.W.>300 - 400
Micro-filtration	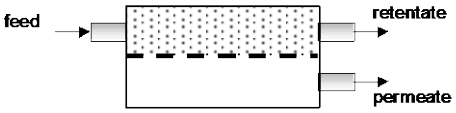	water and solute	Pressure (~0.1Mpa)	suspensions (silicate, bacteria)
Ultra-filtration	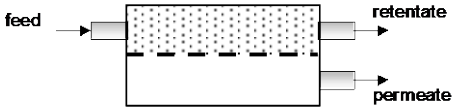	water and salt	Pressure (0.1~0.6MPa)	large bio-molecules, colloids
Gas permeation	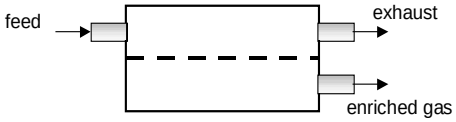	gas and vapour	Pressure (0.1~10MPa)	rejected gas or vapour

* note: ------- represent for membranes. **A**: anion transfer membrane. **C**: cathode transfer membrane.

From 1986 to 1995 Wakeman and his co-worker [8,9,10] reported their results for electromicrofiltration of china, clay and anatase particles. Remarkable improvements in filtration performance were made both in continuous and pulsed electric field application (Figure 2-3). For example, increases in permeate flux of 250-650% were obtained under the application of 50V DC (i.e. 167V/cm field strength, Figure 2-4). The separation of a double chain cationic surfactant from water with electromicrofiltration was also studied[11]. The results further verified that in the presence of the electric field the permeate flux and rejection reach steady state faster compared to the case without electric field (Figure 2-5). However, the early work of Wakeman's group did do not pay sufficient attention to the effect of gas generated by electrolysis on the permeate flux and to the other electrochemical aspects of the feed solution, for the phenomenon of transient permeate flux increase[11] was not adequately explained and there was no gas releasing passage on the permeate side.

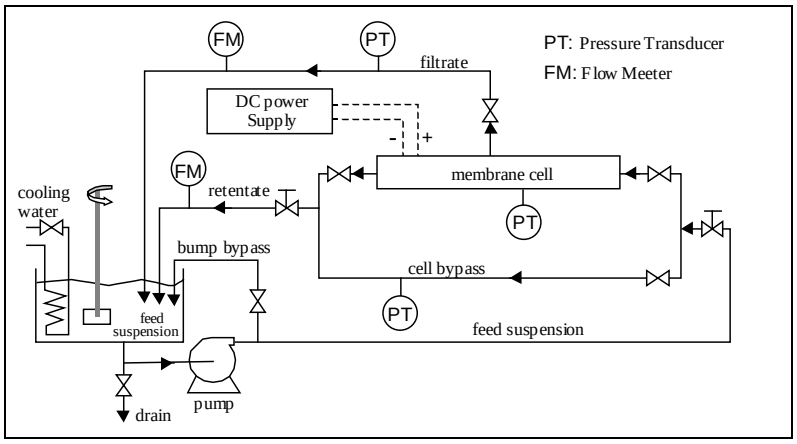

Figure 2-3 Schematic diagram of the crossflow electrofiltration flow circuit[10] .

In addition to the transmembrane pressure, cross flow velocity, solute concentration, the electric field strength and electrode current are key control variables in electrofiltration processes. It is considered that there are three operating regimes of an electromicrofilter with regards to electric field strength [12,13]. Henry et al (1977) proposed that a critical voltage exists for a given electromicrofiltration system. When the electrofiltrater operates under the critical voltage (E=0 or E<critical field strength, Figure 2-2(a) and (b)), there is a net accumulation of particles on the membrane surface and cake fouling will develop (assuming the particle size is larger than the membrane pore size) . Whereas, if electrofiltration operates above this critical voltage, the tendency of particles to migrate away from the membrane will surpass the particle migration

toward the membrane, and eventually prevent or eliminate caking (Figure 2-2(c)). Although the zeta potential of particles and the operating transmembrane pressure are know to affect the value of critical voltage, data of critical voltages have not yet been reported.

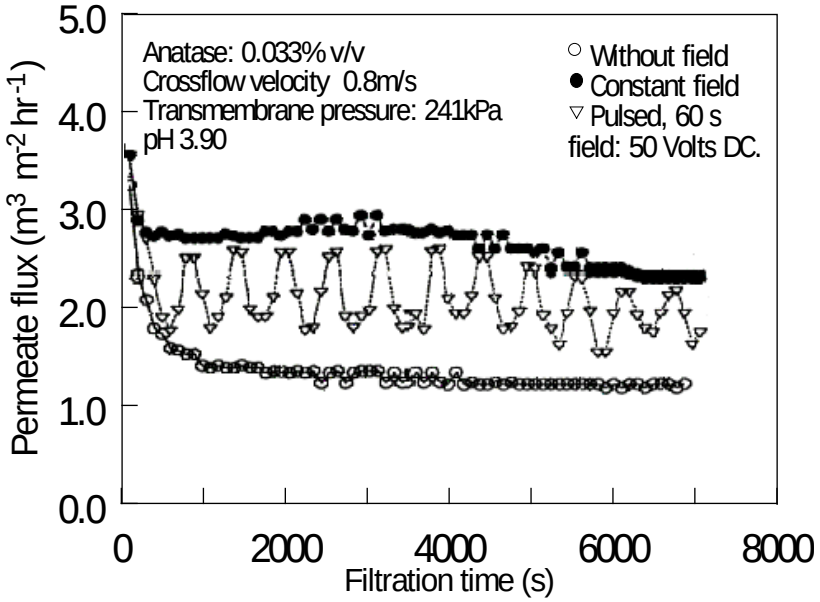

(a)

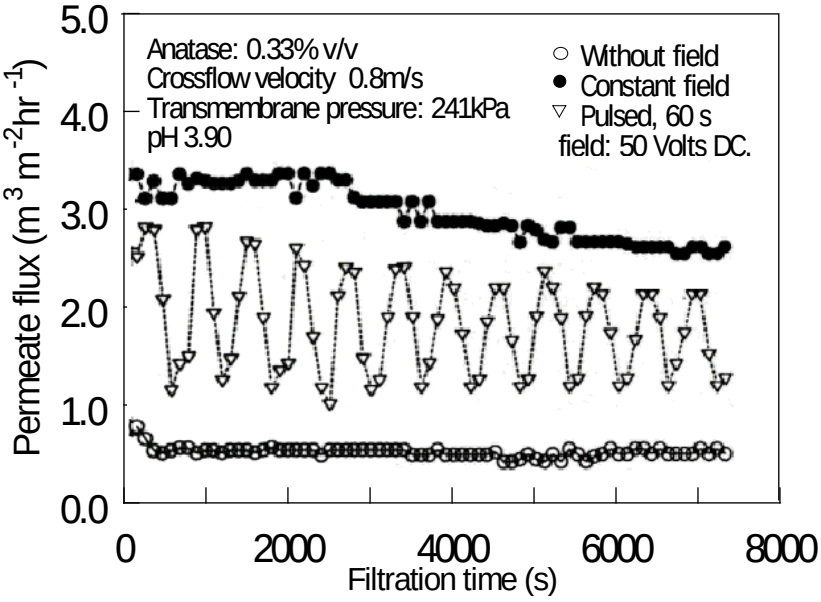

(b)

Figure 2-4 Comparisons of permeate flux decline curves for the filtration of anatase suspensions with no added field, a constant field, and a pulsed field. The feed concentrations were (a) 0.033%v/v, and (b) 0.33%v/v [10].

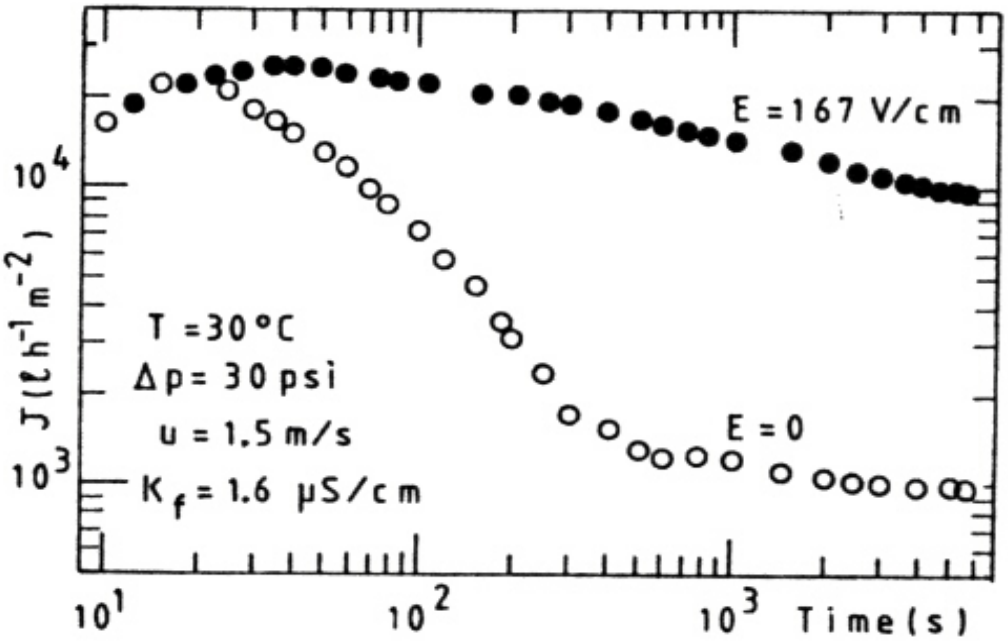

Figure 2-5. The effect of electric field on the decay of permeate flux for the filtration of double chain cationic surfactant from water (J(t)) [11]

The critical voltage is defined as an electric potential in which the net force driving the particle to deposit onto the membrane is balanced by the electric repulsion [12]. The value of critical voltage is affect by the zeta potential of the particle and the operating condition, principally the transmembrane pressure. The electric repelling force acting on the particle is a product of the electric field strength and the net charge of the particle[7], which is proportional to its zeta potential. Thus a higher zeta potential corresponds to a stronger electric repulsion in a given field strength, and hence a lower critical voltage. On the other hand, a more highly charged counter-ions or high ionic strength in the solution will compress the electric double layer and reduce the particle zeta potential.

Bowen and Hughes et al[31]. studied the relationship of the zeta-potential of an inorganic membrane and the pH of the solution, as well as the dependence on pH of the amount of the protein bovine serum albumin (BSA) adsorbed on such a membrane. When the electric properties of this membrane (aluminum oxide) were altered by an external electric field, the filtration rate was improved [17,32,].

Radovich et al [14,15] developed a mathematical model to predict flux behaviour under the influence of an external electric field for BSA undergoing UF. The model uses the values of the solution and solvent fluxes for normal UF and the electrophoretic properties of the solute to predict the electroultrafiltration flux. The discrepancy between predicted and observed behaviour was found to be 7.5% for this model.

Many types of electrofilter have been used for investigating different separations. The possible module configurations vary between applications and are limited by the properties of electric conductivity of the membrane. Figure 2-2, 2-6 and 2-7 shows some of the basic configurations of electrofilters.

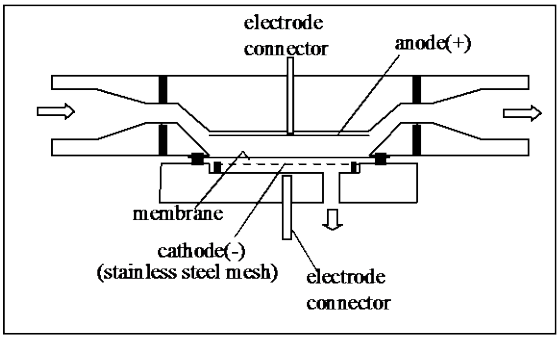

Figure 2-6. Flat sheet configuration[32]

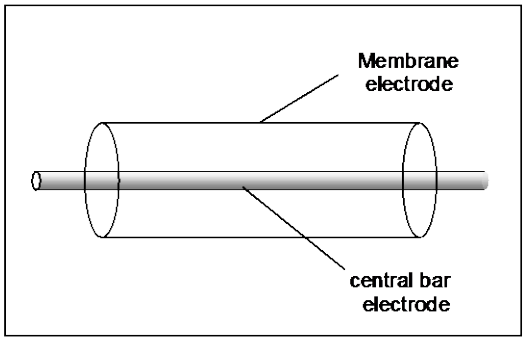

Figure 2-7. Tubular configuration

As mentioned before, stainless steel membranes or supports are preferred by many researchers [16,17,8,9,10,15] as this offers the advantage of being a good conductor of electricity, relatively cheep, and easy to clean.

Sintered stainless steel membranes used in earlier investigations carried out by Massey University have shown some promising results in bioseparation processes[15]. These initial characterization experiments were performed on a sintered stainless steel membrane with a nominal pore size of 25μm . This is large compared to many microfiltration membranes (more typical pore size are in the range of 0.1- 2μm), and as a result high permeate fluxes were noted throughout the investigation (e.g. the initial permeate flux > 10^5 LMH). A 0.7%(w/v) calcium carbonate solution with a Dp_{50} of 25μm was used as the main test fluid, while bakers yeast suspension was used in some experiments. The effects of cross flow velocity (1.1-1.6m/s), pH (6-9), ionic strength (0.017-0.145) and electric field strength (0-40V/cm) on permeate flux were

examined along with the interactions between these variables. Considerable improvement in membrane performance was noted when a 40V/cm electric field was applied to the membrane: the average steady state flux when the membrane was charged was found to be approximately double that of when no charge was applied. The rate of flux decline and the time taken to reach steady state flux were also significantly reduced in the presence of an electric field.

However, when comparing these results to Wakeman and co-workers, the effects of the electric field obtained by Reeve were less than that seen by Wakeman. The possible reasons may be: 1) Different field strengths were used. 167V/cm voltage gradient was used by Wakemen, but 40V/cm by Reeve; 2) Different feed materials were used. The anatase (TiO_2) particle used by Wakemen has a much lower water solubility than the calcite ($CaCO_3$) particle used by Reeve in the full range of pH. Dissolved $CaCO_3$ would separate out on the cathodized membrane as the permeate pH increased by electrolysis, resulting in additional fouling; and 3) Different membrane structure and pore size were used. The membrane used in Wakeman's experiment was a composite: a 0.2μm rated Nuclepore polycarbonate membrane was placed on the top of the porous stainless steel as the filtering medium, and pore plugging was unlikely occur because of the particle mean size was 5μm. In contrast, the membrane used by Reeve did not has a polymer skin. The nominal mean pore size was 25μm which was approximately the same with the particle mean size, thus pore plugging might become the main fouling mechanism. In this case an external electric field is less effective to inhibit pore plugging because the field strength always approaches zero inside the pore mouth of the stainless steel membrane (This effect is illustrated in section 5.5. and Figure 5-15 in this thesis).

2.2 The Application of Electrofiltration in Dairy Industry

Membrane processes have been widely used in dairy industry for various separation purposes, such as [18] : whey protein concentration; milk protein fractionation and concentration; bacterial reduction in milk and brine; partial demineralization of whey; reduction of lipids in whey protein concentrates. By taking the advantage of electric rejection, electrofiltration has great potential to enhance the existing filtration processes (e.g. by increasing the throughput in existing plants or by reducing production cost), or to develop new fractionated products based

on differences in molecular charge. Since one of the major problems and limitations of membrane processes are considered to be membrane fouling and cleaning[19], this technology has aroused interest with regard to its application in dairy processes. Membrane fouling in dairy processes can be identified as due to minerals, proteins or lipids, and the cooperating effects of these. This research will focus on mineral fouling, especially by calcium and phosphate and the potential to recover these component from whey.

The concentration of calcium and inorganic phosphate in milk are relatively high[20], approximately 30 and 20 mmol/l, respectively, and the behaviour of these ions dominates the mineral equilibrium in milk. Approximately two-thirds of the calcium and one half of the inorganic phosphate are colloidal. It is presumed that all colloidal inorganic calcium is partly incorporated in micellar calcium phosphate(MCP), whereas colloidal calcium is partly incorporated in the MCP and partly bound directly to the casein and to a lesser extent the whey proteins. Calcium may also interact with lipid material. The structure of MCP is complex and not clearly identifiable with any known form of calcium phosphate. Citrate, magnesium and active groups on the caseins appear to play a role in MCP, and MCP may have unique properties that are different from those of any other form of calcium phosphate.

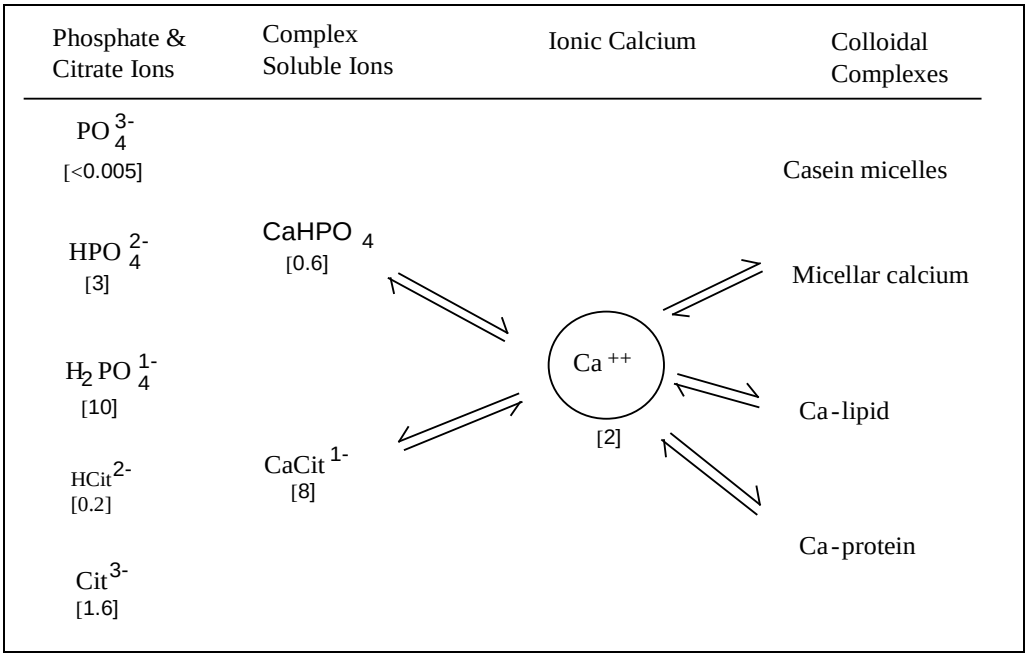

Figure 2-8. Calcium and inorganic phosphate equilibria in milk with the equilibria associated with the calcium highlighted. The number in square brackets are calculated concentrations of the specific ions (mmol/l) [19]

The remaining calcium and inorganic phosphate exist in a variety of forms within the aqueous phase of the milk, with $CaCit^{1-}$ and $H_2PO_4^{1-}$ being in the highest concentration (Figure 2-8).

This portion of the calcium and phosphate passes through a UF membrane whereas the colloidal material is retained.

The aqueous phase of milk is supersaturated with respect to most of the calcium salts (Table 2-2) and is thermodynamically unstable. However, although precipitation of calcium phosphate must eventually take place, equilibrium is obtained very slowly[15].

Mineral precipitation is a complex phenomenon. Although, thermodynamically, precipitation from milk or whey should occur, the kinetics of such reactions are often very slow and the presence of inhibitors in the solution may limit precipitation. Furthermore, both the driving force for precipitation (thermodynamically and kinetically) and the likely form of the precipitated calcium salt are affected by the pH, the temperature and the concentration of all of the ions in solution. Precipitation is more likely at high pH, high temperature and high calcium concentration.

Protein and other minerals appear to stabilize the calcium phosphate in solution [20]. The equilibria described in Figure 2-8 are applicable only to the milk system, which is strongly buffered to calcium activity. When the caseins are removed, as in the case of whey, the equilibria are disrupted and mineral precipitation is far more likely because of the lower buffering capacity of the whey proteins. Precipitation is even more likely in a whey or milk permeate from which the whey proteins have also been removed.

Lyster[21], based on a computer calculation of the ions equilibrium in milk, predicted that milk solution was supersaturated with respect to hydroxyapatite above pH 6 at all temperatures and above pH 4 at high temperatures. Only around pH 5-6 and at low temperatures was the solution supersaturated with respect to tricalcium citrate. If precipitation of hydroxyapatite is prevented due to inhibition or slow kinetics, then the precipitation of other calcium salts is possible. Although the study gives an indication of what salt form may precipitate, precipitation is extremely complex and accurate predictions on what calcium salt may precipitate or when are almost impossible.

Table 2-2. Various forms of precipitated calcium salts [19]

Formula	Name	Code	Solubility product, K_s

$CaHPO_4$	Dicalcium(monetite)	DCP	$1.26x10^{-7}$
$CaHPO_4 \cdot 2H_2O$	Dicalcium phosphate dehydrate(brushite)	DCPD	$2.49x10^{-7}$
$Ca_4H(PO_4)_3 \cdot 2.5H_2O$	Octacalcium phosphate	OCP	$1.05x10^{-47}$
β-$Ca_3(PO_4)_2$	Tricalcium phosphate(whitlockite)	TCP	$1.15x10^{-29}$
Amorphous $Ca_3(PO_4)_2$	Tricalcium phosphate	ACP	$2.3c10^{-29}$ est.
$Ca_5(HO)(PO_4)_3$	Hydroxyaphate	HAP	$1.8x10^{-58}$
	Micellar calcium phosphate	MCP	---
$Ca_3(Cit)_2 \cdot 4H_2O$	Tricalcium citrate	CCIT	$2.3x10^{-18}$
$Ca_3(Cit)_2 \cdot 6H_2O$	Tricalcium citrate	CCIT	---

Table 2-3. Composition of whey and whey permeate[22]

	Sweet whey	**Permeate**	**Acid whey**	**Permeate**
solids, %	6.7	5.7	6.42	5.8
Gross composition (solids basis)				
lactose, %	74.7	85.9	68.5	74.1
protein, %	8.9	0.2	8.3	0.3
ash, %	7.8	8.8	9.3	9.7
fat, %	3.7	0.1	0.8	0.1
lactic acid, %	2.0	2.5	7.3	7.6
non-protein N, %	0.05	0.04	0.05	0.05
Minerals (solids basis)				
Ca, mg/100g	470	1450	540	1360
Mg, mg/100g	100	143	100	130
Na, mg/100g	750	758	680	580
K, mg/100g	2342	2340	1840	2225
P, mg/100g	580	464	640	850
Zn, ug/100g	193	4300	58	298
Fe, ug/100g	340	550	209	200
Cu, ug/100g	66	50	15	14
Ma, ug/100g	9	15	3	2

Cl, mg/100g	~100*			

* From J N Clark, Uork JN(1988) NZ J.Dairy Sci. Tech.23, p.310

As noted, mineral precipitate is more likely to occur in whey or whey permeate. This is of particular significance as whey processing is one of the major application of membrane

separations in food processing. Whey arises from cheese or casein production and the composition of the whey and whey permeate is shown in Table 2-3. One of the characteristics of this is the high content of calcium and phosphorous. Precipitation of Ca^{+2} and $(PO_4)^{-3}$ can be promoted and the separation of precipitate from whey will produce 'Alamin', a white powder with complex composition (mainly calcium phosphate) and chemical properties. Generally, this is produced by adjusting the pH(>6.5) and heating the whey; the deposit is then removed by centrifugation, but a MF process may be a possible alternative for this. In order to investigate the possibility of MF process and its membrane fouling, Alamin was employed as the suspended material for the electromicrofiltration process in this research.

3. Experimental Apparatus and Materials

3.1. Experimental Apparatus

The experimental apparatus comprised a cross-flow microfiltration membrane module, a 30 litre feed tank, a pump with 0.75kw AC three phase motor, a tubular heat-exchanger, valves, a pair of pressure transducers (0~4bar), and a XTRAVERT® AC motor speed controller (mode X302, PDL Electronic LTD, Napier, NZ). Figure 3-1 show the assembled apparatus and a typical arrangement of the system is illustrated in Figure 3-2. Further details on main components and system operation are given below.

3.1.1. Membrane Module

Two sintered stainless steel membranes supplied by Industrial Research Limited (NZ) were used in this work. This material gave the membrane some unique features when compared to polymeric membranes including high resistance to chemical cleaners, electrical conductivity and the ability for high-pressure operation. The difference between the membranes was their mean pore size: the smaller pore membrane was nominally 5μm, and the larger pore size unit was nominally 25μm. The membrane and the central bar (also stainless steel) comprised a pair of electrodes when they were electrically charged. The perspex jacket collected the permeate and returned it to feed tank. Some key dimensions of the membrane are:

membrane tube inner diameter:	ϕ13.5mm;
effective length:	380mm,
central bar diameter:	ϕ8mm;
nominal pore size:	5μm for the small pore size membrane, and 25μm for the large pore size membrane.
filtration area:	0.019m^2

Photographs of the membrane as assembled and disassembled are shown in Figure 3-3(a) and Figure3-3(b), respectively.

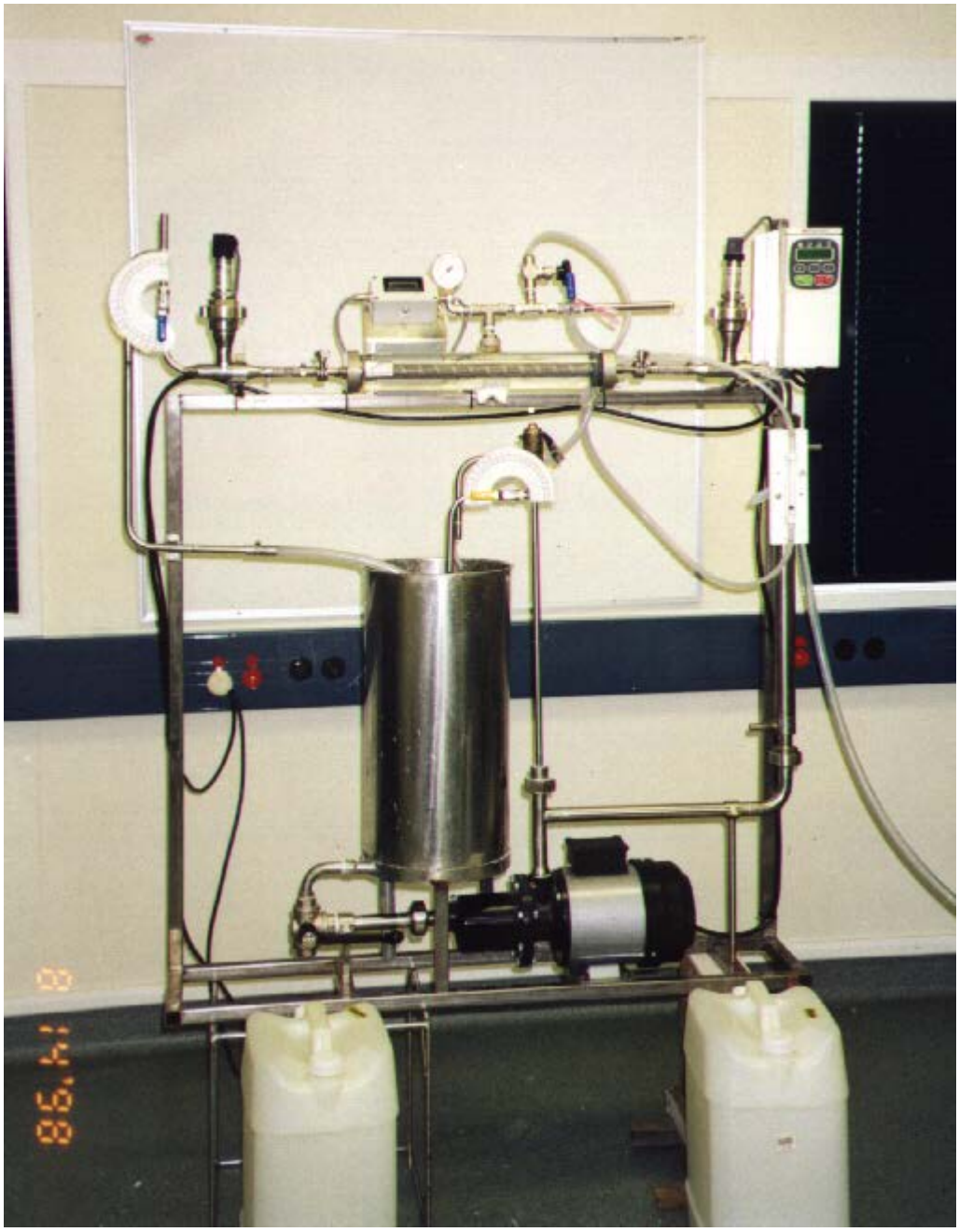

Figure 3-1. Picture of the experimental apparatus

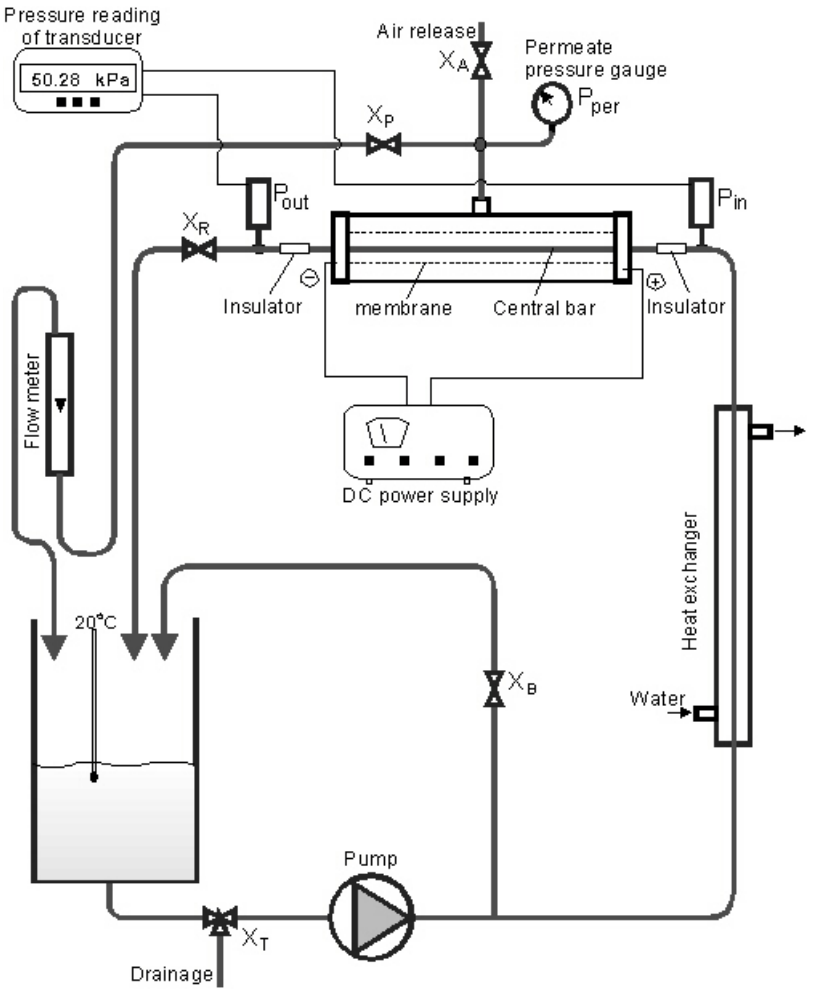

Figure 3-2. Schematic diagram of the system arrangement

(a) assembled module (b) disassembled module

Figure 3-3. The membrane module

3.1.2. DC Power Supply

The membrane was charged with a Goldstar DC power supply (Model GP-503, made by LG Precision Co. Ltd., USA) to create an electric field in the annular space between the

membrane and central bar. A voltage gradient in the range of 0~180 V/cm and a current density of 0~158 A/m^2 on the membrane were used in this work. The capacities of the DC power supply are 0~3 A, and 0~50 V; both may be regulated.

3.1.3. Pressure and Flow Measurement

The pressure of the feed and retentate streams were measured with a pair of pressure transducers (0~4 bar), and the readings were displayed on a monitoring LCD. The accuracy of measurement was ±0.5 kPa. A standard Bourdon gauge of 0~250 kPa was used to measure permeate pressure. It was found the readings of this gauge needed calibration against a water manometer in the low pressure range of 0~10 kPa. The permeate was measured with a rotation flowmeter with a range of 0~300 ml/min.

3.2 Overview of Experiment Design

Particulate suspensions of Alamin or calcite were used as the filtration liquid in this work at concentrations of 0.07%~1%(w/v). The most common concentration was 0.7%(w/v). The suspension was prepared and stored in the cylindrical feed tank, and was pumped to feed the tubular membrane module, with the retentate recycled back to the tank. A by-pass stream was maintained with valve X_B to achieve dual functions: firstly, to assist in agitating the suspension in the tank, and secondly to adjust the feed pressure (coupled with the adjustment of pump speed and the opening of the retentate valve, X_R). The pressure of the feed stream ($\mathbf{P_{in}}$) and retentate stream ($\mathbf{P_{out}}$) were measured with an inlet and an outlet transducer, respectively. Permeate pressure ($\mathbf{P_{per}}$) was measured with a gauge. A flowmeter was used to measure the permeate flow before it returned to the tank.

As the feed stream could be warmed during several hours running, or the temperature could deviate from its desired setting because of the temperature difference with the environment, a heat exchanger was employed to maintain a constant temperature of 20°C.

Since gas formed at the electrodes when an electric field was applied, a gas-release tube was used to minimize the disturbance of the flowmeter readings by gas bubbles. In order to give physical and chemical stability to the apparatus, the main parts of it were made of stainless steel. The membrane and the central bar were electrically isolated with plastic junctions, and the membrane module was electrically isolated with the rest of the apparatus by a pair of plastic tubes at its inlet and outlet (Figure 3-2).

Another aspect was the requirement of the effective control to some important variables, such as transmembrane pressure ($\Delta\mathbf{P_{TP}}$), permeate flux (**J**), cross-flow velocity (**u**), temperature (**T**), and membrane voltage and current. These are discussed below.

3.2.1. Transmembrane Pressure Control

As the driving force of the membrane filtration process, the transmembrane pressure ($\Delta\mathbf{P_{TM}}$) is expressed as:

$$\Delta\mathbf{P_{TM}} = \frac{\mathbf{P_{in}} + \mathbf{P_{out}}}{2} - \mathbf{P_{per}} \qquad (3\text{-}1)$$

The first term on right hand side of Eq. (3-1) represents the average pressure of the retentate stream, the second term ($\mathbf{P_{per}}$) is the permeate back pressure. Pressure drop along the membrane tube ($\mathbf{P_{in}}$-$\mathbf{P_{out}}$) is a function of cross-flow velocity (**u**) and permeate flux (**J**). There are three control variables that can affect the transmembrane pressure: (1) the pump speed; (2) opening of retentate valve X_R; and (3) opening of permeate valve X_P . It is important to choose reasonable setting for the valve-opening and pump speed to achieve and maintain the designed operating conditions. For example, closing retentate valve X_R and permeate valve X_P while keeping the by-pass valve X_B open and the pump running can provide an equal hydrostatic pressure condition for $\mathbf{P_{in}}$, $\mathbf{P_{out}}$ and $\mathbf{P_{per}}$ to permit calibration of the pressure gauge and transducers. Alternatively, fully opening the retentate valve X_R and the by-pass valve X_B ,and keeping a low pump speed while adjust the opening of permeate valve X_P , can achieve an adjustable low transmembrane pressure condition for constant flux or critical flux experiments. The valve X_{per} on permeate side was a needle valve which allowed accurate flux control. The other valves were ball valves.

3.2.2. Permeate Flux Control

Because of the existence of fouling, the permeate flux achieved with porous media always be characterized as an attenuation function of filtering time. In contrast the pure water flux ($\mathbf{J_w}$) is independent of time (**t**) and cross-flow velocity (**u**), and is directly proportional to the pressure applied, as shown by the *Darcy* equation:

$$\mathbf{J_w} = \frac{\Delta \mathbf{P_{TM}}}{\mu \mathbf{R_m}} \qquad (3\text{-}2)$$

where μ is the permeate viscosity (Pa·s), and $\mathbf{R_m}$ is the resistance of the membrane (m^{-1}).

Control of the initial flux was found to be important. High $\Delta \mathbf{P_{TM}}$ and initial flux would cause serious pore plugging and rapid flux decline. On the other hand, cross-flow microfiltration (CMF) normally operates in low pressure range (1~5 Bar) where adjustment to the feed pressure $\mathbf{P_{in}}$ is limited. By adjusting the needle valve X_P on the permeate side, the $\Delta \mathbf{P_{TM}}$ can be manually controlled, so as to control the permeate flux. However to manually achieve a constant flux control was difficult. This was only obtained in the lower **TMP** (e.g. less than 8 kPa) and the lower flux region (e.g. 45~65 LMH) on the 5μm membrane.

3.2.3. Cross-flow Velocity Control

Cross flow velocity was determined manually by measuring the volume of retentate collected in a limited time. To achieve a given velocity in an experimental run, the operating conditions were pre-set with pure water. Figure 3-4 shows the relationships of cross flow velocity at different transmembrane pressures on the 5μm membrane. There are two operating tactics can be identified to obtain a different cross flow velocity in the iso-transmembrane-pressure condition:

(1)Reduce the pump speed and turn down the opening of retentate valve X_R accordingly to obtain a lower cross flow velocity at the same transmembrane pressure, while keeping the other valves unchanged.

(2)Increase the pump speed and turn down the opening of permeate valve X_{per} accordingly to give a higher cross flow velocity at the same transmembrane pressure, while keeping the other valves unchanged.

For instance, at point A of Figure 3-4 the transmembrane pressure is 50kPa, and the cross flow velocity 2.28m/s (many sets of runs were operated at these conditions in this study). Reducing the pump speed will bring both the velocity and pressure down, e.g. to the point B, then turning the valve X_R down accordingly will restore the pressure to 50kPa at point C (but at a lower cross flow velocity). A reverse operation by increasing the pump speed and turning the valve X_P down is shown in Figure 3-4 by the path A→B'→ C'.

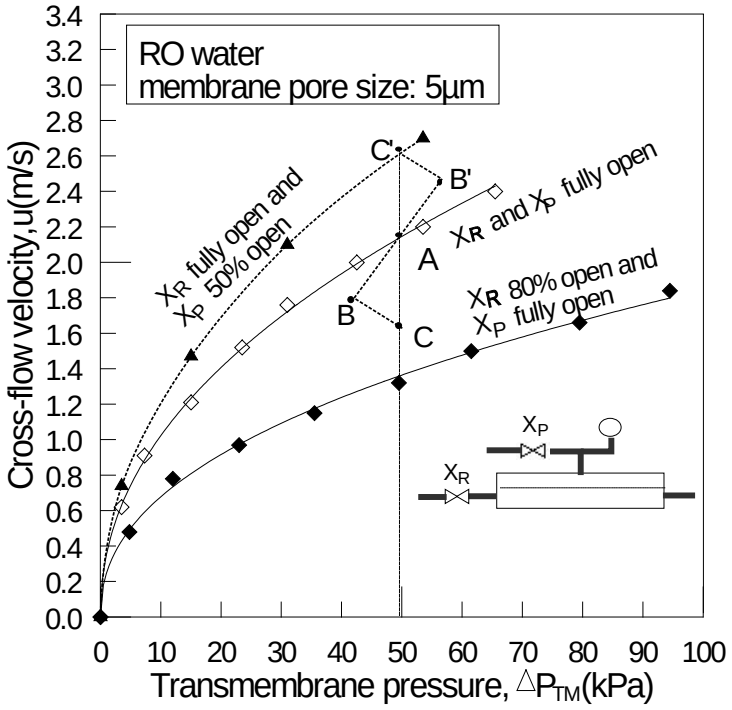

Figure 3-4. Cross flow velocity vs transmembrane pressure at different operating conditions

3.2.4. Temperature Control

Retentate temperature was measured with a digital thermometer and controlled with the jacket heat exchanger. The temperature was set to 20°C for most experiments.

3.2.5. Membrane Voltage and Current Control

As the membrane was electrically charged, an electric field was formed between the membrane and central bar, and particles then migrated under the action of the electric field force. Nevertheless, some electrochemical reactions took place simultaneously with the formation of gas bubbles, consuming more energy and influencing particle movement. Secondly, we can not ignore the influence of electrochemical reactions on the properties of membrane and solution. Thus the electric current density on membrane also needed to be carefully controlled. This was done by pre-setting the output current and voltage of the DC power supply.

3.2.6. Cleaning Procedure

The microporous membrane and all the inner surfaces of the system would be fouled after each run by a deposit layer arising from absorption or adherence. Thorough cleaning is necessary to restore the original filtration capacity of the membrane. A regular cleaning procedure, developed by examining and comparing the test results, was used after each run (see more details in Chapter 6):

1) Backflush tap water for 10 minutes at above 100kPa backpresure.
2) Recirculate acid solution (0.2% nitric acid) for 15~20 minutes at about 30kPa and 20°C
3) Recirculate RO water (10 litrefeed volum) at low pump speed and low pressure. Then drain the water, including the residue water in the membrane jacket which is slight acidic (pH at 3.5~4.), from the system.
4) Recirculate the same amount of RO water again for 2 minutes, then drain. The reason for rinsing twice is to replace the residual water in the membrane jacket completely.

Moreover, besides the routine cleaning, an additional alkaline washing procedure (with 0.2% NaOH solution) was added after acid washing when the membrane had been run for 4-5 times (i.e. about one week duration). Cleaning in this way restored the membrane performance to over 98% to its original value. Even though the fouling layer was a little harder to remove in experiments involved applying an electric field (see details in chapter 5).

3.3 Calibration of the Readings of Pressure Gauge and Transducers

When the retentate valve (X_R) and permeate valve (X_P) are both completely closed with the pump running and by-pass loop valve X_B open, these will result in: (1) cross-flow velocity **u**=0 , and (2) permeate flux **J**=0 . The first result brings about the condition of $P_{in}=P_{out}$, and the second result bring about $\Delta \mathbf{P_{TM}}=0$. According to Eq. (3-1), we have $\frac{1}{2}\mathbf{(P_{in}+P_{out})-P_{per}=0}$, and $\mathbf{P_{in}=P_{out}=P_{per}}$. i.e. an iso-hydrostatic pressure condition was obtained.

A vertical water column coupled through the air releasing valve (X_A) was used to calibrate the readings of the pressure gauge and transducers in the low pressure range (0~10kPa). The valve (X_A) was fully opened, and the valve (X_B) or the pump seed were adjusted to obtain different hydrostatic pressure (Figure 3-2). Table 3-1 show that the readings of the transducer for ($\mathbf{P_{out}}$) were correct within the test range, but readings for ($\mathbf{P_{in}}$) and ($\mathbf{P_{per}}$) needed correction. The results in Table 3-1 and Table 3-2 are plotted in Figure 3-5 and Figure 3-6, respectively.

Table 3-1. Calibration of the readings of pressure gauge and transducers in low pressure condition

H_2O Column Hight (mm)	0	40	200	400	500	600	700	800	900	1000	criteria
Gauge Readings, P'_{per} (kPa)	0	0	8	10	12		13.8	---	----	16	need correcting
Inlet transducer readings, P'_{in} (kPa)	0	-	-	5	6	7	8	9	10	11	need correcting
Outlet transducer readings, P'_{out} (kPa)	0	-	2	4	5	6	7	8	9	10	correct

note: 1000mmH_2O = 10kPa

It was assumed that the readings of ($\mathbf{P_{out}}$) at higher pressures would remain correct, and could be a reference to calibrate the readings of ($\mathbf{P_{in}}$) and ($\mathbf{P_{per}}$). Table 3-2 show the calibration of readings of ($\mathbf{P_{in}}$) and ($\mathbf{P_{per}}$) on higher pressures.

Table 3-2. Calibration of the readings of ($\mathbf{P}_{per}$) and ($\mathbf{P}_{in}$) in higher pressure condition

Outlet transducer Readings, P'_{out} (kPa)	5	9.5	15	25	35.5	46	56	66.5	76	85.5	96.5	107
Inlet transducer Readings, P'_{in} (kPa)	6	10.5	16.5	26	36.4	47	57.1	67.6	77	86.6	97.6	108.1
Gauge Readings, P'_{per} (kPa)	10	15	20	30	40	50	60	70	80	90	100	110

Outlet transducer Readings, P'_{out} (kPa)	116.5	126.5	136	148.5	158	166.5	178	188	197.5
Inlet transducer Readings, P'_{in} (kPa)	117.6	127.5	137	149.5	159.1	167.7	179.2	189.2	198.7
Gauge Readings, P'_{per} (kPa)	120	130	140	150	160	170	180	190	200

In the low pressure range of 0 ~ 10kPa, a regression curve of the gauge reading ($\mathbf{P'_{per}}$) and pressure ($\mathbf{P_{per}}$) was given by Figure 3-5 which took the form of a polynomial

$$\mathbf{P_{per}} = 0.046(\mathbf{P'_{per}})^2 - 0.142\mathbf{P'_{per}} + 0.424, \quad (0 < \mathbf{P_{per}} < 10\mathbf{kPa}) \qquad (3\text{-}3)$$

In the higher pressure range above 10kPa, the calibration relationship became a straight line shown in Figure 3-6, and expressed as

$$\mathbf{P_{per}} = 1.016\mathbf{P'_{per}} - 5.23, \quad (\mathbf{P_{per}} > 10\mathbf{kPa}) \qquad (3\text{-}4)$$

Combining Eq. (3-3) and (3-4) we can get:

$$\mathbf{P}_{per} = \begin{cases} 0.046(\mathbf{P'}_{per})^2 - 0142\mathbf{P'}_{per} + 0.424, & (0 < \mathbf{P}_{per} 10k\mathbf{Pa}) \\ 1.016\mathbf{P'}_{per} - 5.23, & (\mathbf{P}_{per} > 10k\mathbf{Pa}) \end{cases} \qquad (3\text{-}5)$$

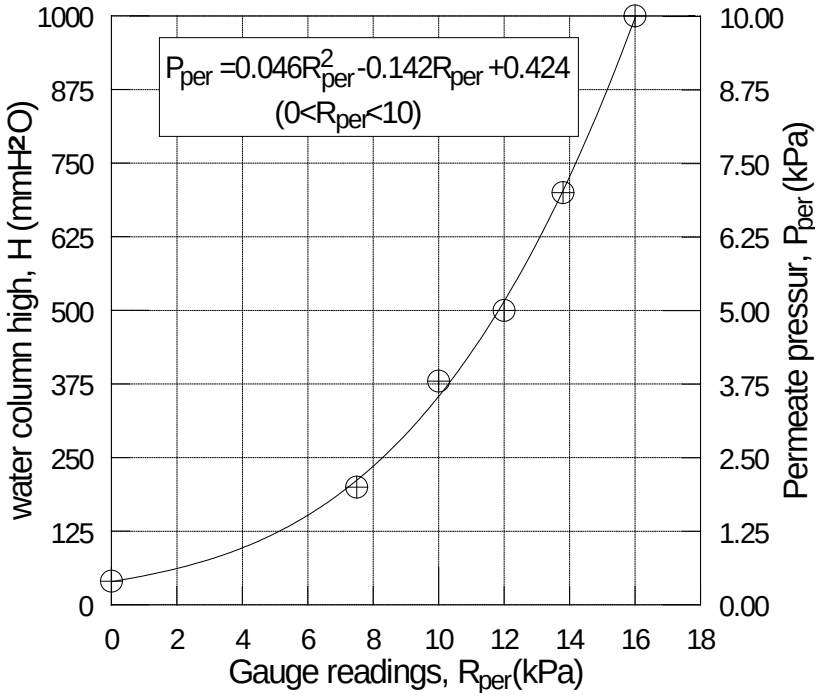

Figure 3-5. Calibration of the gauge readings in the low pressure range

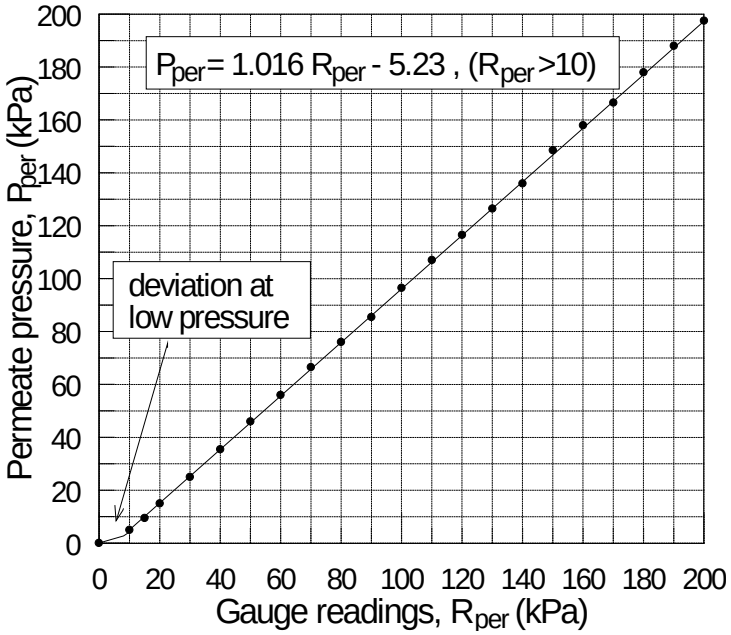

Figure 3-6. Calibration of the gauge reading in the higher pressure range

3.4 Experimental Materials

In this study two kinds of particle were used : calcite and Alamin. The former was prepared by chemical deposition. The latter was a by-product of dairy industry which was separated from whey (see more details in Chapter 2). Their particle morphologies are similar. The major focus was on the behaviour of the Alamin suspension and the calcite was used for comparison.

3.4.1. Preparation of Calcite Particle

The method of preparation followed that used by Reeve (1997):

(1) Principle

$$\mathbf{CaCl_2 + Na_2CO_3 = CaCO_3 \downarrow + 2NaCl} \qquad (3\text{-}6)$$

(calcite)

(2) Chemicals

Anhydrous Calcium chloride [$CaCl_2$] :	111 g
Sodium carbonate [Na_2CO_3] :	106 g
Sodium chloride [NaCl] :	176 g
Ethanol :	600 ml
Distilled water :	enough

(3) Procedure

(a)Dissolve the anhydrous calcium chloride in distilled water to make up 3000 ml $CaCl_2$ solution ***A,*** then add 300 ml ethanol to it to obtain solution ***AE.***

(b)Dissolve the sodium carbonate in distilled water to make up 3000 ml Na_2CO_3 solution ***B***.

(c)Dissolve the sodium chloride in distilled water to make up 3000 ml NaCl solution ***C*** , then add 300 ml ethanol to it to get solution ***CE***.

(d)Mix solution ***AE*** and ***CE*** to get about 6600 ml water solution ***ACE*** of $CaCl_2$, NaCl and ethanol. This is an acidic solution.

(e)Slowly add solution ***B*** to ***ACE*** with vigorous stirring to give a milky suspension. Then leave to stand for about two hours to allow the calcite particles to settle down. The solid content of the suspension before solid-liquid separation was about 1%(w/v). About 100g calcite powder was obtained after sufficient washing, suitable filtration and drying.

The solubility of calcium carbonate at 25°C is 1.53×10^{-3} (g/100ml H_2O) and the solubility product K_{sp} is 3.1×10^{-7} [23].

3.4.2. Alamin

Alamin is a white powder, having a pleasant, slight whey-like smell, which is separated from whey concentrate. It is a complex substance mainly composed of calcium phosphorous, but the structure is different from any known crystalline calcium phosphate. Alamin was supplied by the NZ Dairy Board.

3.4.3. Physical Properties of the Particles Relevant to Microfiltration

The particle behavior was observed with a light microscope. Some characteristics of the particles, such as mean size, dispersibility in water, and electrophoretic mobility were also studied (see Table 3-3).

Table 3-3. Some characteristics of calcite and Alamin particles

	Calcite particles	Alamin particles
Appearance	white powder, particles are transparent in water under the examine of microscope	white powder, particles are transparent in water under the examine of microscope
Particle mean size[(1)], (μm)	8.15	4.63
Standard deviation[(1)], SD(μm)	6.46	3.53
Deposit time[(2)] (hrs)	~1	>10
Dispersibility in water	Good	good
Iso-electric point		
Specific weight(g/ml)	2.70~2.95	2.274[(3)]
Dissolving pH		4.9
Porosity		68.8% [(3)]
Chemical properties	--	suspension is a amphoteric, buffer solution
Microbial stability	Good	good in solid; perishable in suspension

note:(1) Number of counted particles is 200, examined with biological microscope in 10x40-fold.

(2) Deposit time: Time required to obtain 50% of clear water separation in a 500ml measuring cylinder by gravity deposition (Figure 3-7).

(3)See appendix for the method of measurement.

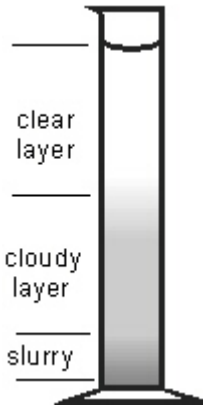

Figure 3-7. The gravity deposition of Alamin

Though their particle size and particle specific density are relatively similar, the particle deposit time of the Alamin is much longer than that of the calcite. This can be explained by the difference of their hydrophilic properties. Alamin particles, since they are generated from whey, might possess more available hydrogen bonds with water molecules, which

would result in stronger hydrophilicity. Another reasonable explanation is that the Alamin contain many more tiny particles (e.g. smaller than 0.1μm) than the calcite, since a triple layer liquid distribution was observed through a gravity deposition (Figure 3-7), deposition for those tiny particles require much longer time.

4. Electromicrofiltration: Experimental Results and Discussions

4.1. Water Flux of Membranes

Water flux is one of the important parameters that characterizes a membrane's performance. Two pore size membranes were used in this study, and reverse osmotic (RO) water was used for water flux test. Results are shown in Figure 4-1 and Figure 4-2 for the 5μm membrane and the 25μm membrane, respectively. The membrane resistance ($\mathbf{R_m}$) of the 5μm membrane is 8.16 times higher than the 25μm membrane. Both flux profiles are linear with $\Delta\mathbf{P_{TMP}}$ in the region examined indicating the water flux obeys *Darcy's* Law.

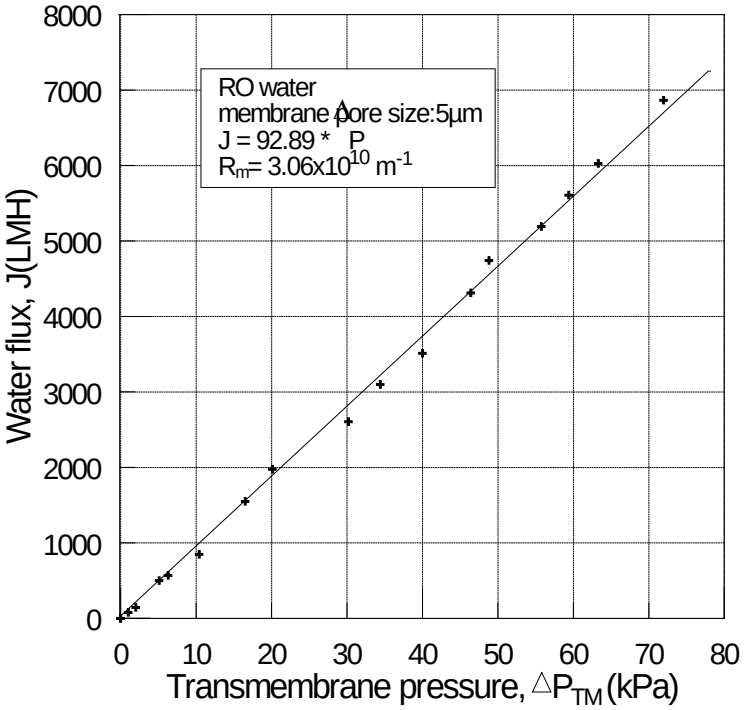

Figure 4-1. Water flux of the 5μm membrane

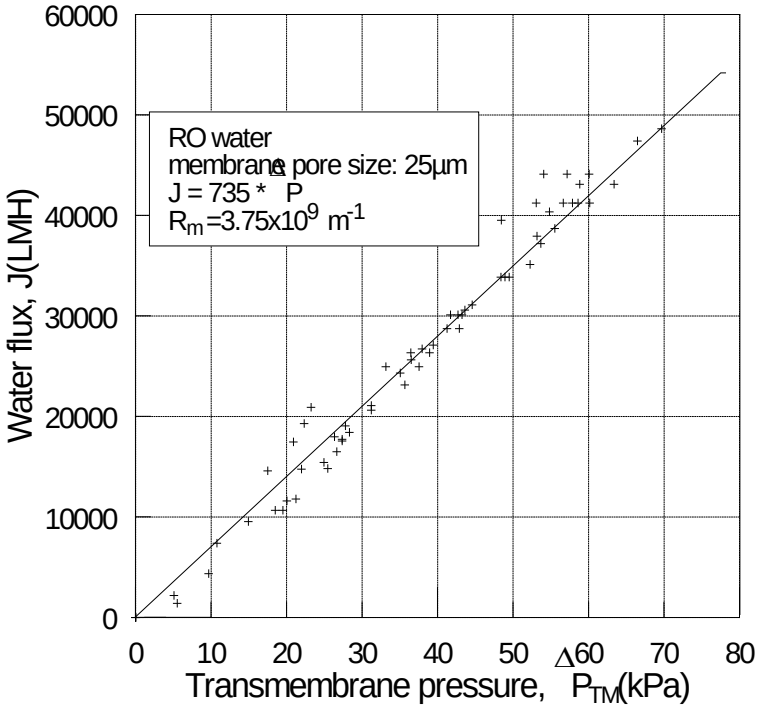

Figure 4-2. Water flux of the 25μm membrane

4.2. The Membrane Pore Size

Membrane pore size is also an important parameter characterizing the membrane, It determine the retained particle size to a major extent, and indirectly influences the porosity of the membrane. The pore tunnel characteristics of the membrane are generally denoted by mean pore size, pore size distribution and porosity. The nominal mean pore sizes of the membranes used in this study were 5μm and 25μm, respectively. The maximal pore size of the membrane was measured in this research with the so-called bubble-point method. This method was found applicable to microfiltration membrane. In this method, the membrane surface is flooded with a liquid (in this case water), and the air is introduced beneath the membrane from the feed side. The air pressure is increased gradually till the first air bubble appears. The pressure at this point is known as the bubble-point pressure and the pressure (**P**) and pore size ($\mathbf{d_m}$) are related in the following manner:

$$\mathbf{d_m} = \frac{4\gamma \cdot \cos\beta}{\mathbf{P}} \qquad (4\text{-}1)$$

here $\mathbf{d_m}$ is the pore size of membrane (μm); γ the surface tension of liquid (e.g. water, $\gamma=72.67\times10^{-3}$ N·m^{-1} [23]. β the contact angle between liquid and solid (i.e. water and stainless steel), and p the pressure of the bubble-point. The formula (4-1) indicates that a larger pore size always leads to bubble formation at a lower pressure, so the result will be the maximum pore size of the membrane.

Since β could not be found from literature, a tiny droplet of water on stainless steel was observed under a microscope against a transparent angle scale to give an estimate of the contact angle of $\beta = 19° \pm 2°$.

The pressures at the bubble-point were measured with a pressure transducer with an accuracy of ±1kPa. For the 5μm membrane, it was 22kPa; for the 25μm membrane, it was 4kPa. According to Eq. 4-1, the maximum pore size of the former is

$$\begin{aligned}\mathbf{d_m} &= \frac{4\times(72.67\times10^{-3}\mathbf{N\cdot m^{-1}})\times(\cos(19^\circ \pm 2^\circ))}{(22\mp1)\times10^3\mathbf{Pa}} \\ &= \frac{4\times(72.67\times10^{-3}\mathbf{N\cdot m^{-1}})\times(\cos(19^\circ \pm 2^\circ))}{(22\pm1)\times10^3\mathbf{Pa}} \\ &= 12.5\pm0.7\mu\mathbf{m}\end{aligned} \qquad (4\text{-}2)$$

Some results are summarized in Table 4-1. Notice that although a larger air bubble might perhaps correspond to a larger membrane pore size, the bubble size is not involved in Eq. 4-2 which implies that the maximal pore size is independent to the bubble size. In fact observation with magnifying lens showed that the air bubbles were almost all the same dimension. A schematic diagram of the principle of this method is shown in Figure 4-3.

Table 4-1. Measurement results of the maximum pore size

	Surface tension Of water, γ	water-stainless steel contact angle, β	bubble-point pressure, P	maximum membrane pore size, d_M
5μm membrane	72.67×10^{-3} N·m^{-1}	19° ±2°	22kPa	12.5±0.7μm
25μm membrane	72.67×10^{-3} N·m^{-1}	19° ±2°	4kPa	73.5±19.2μm

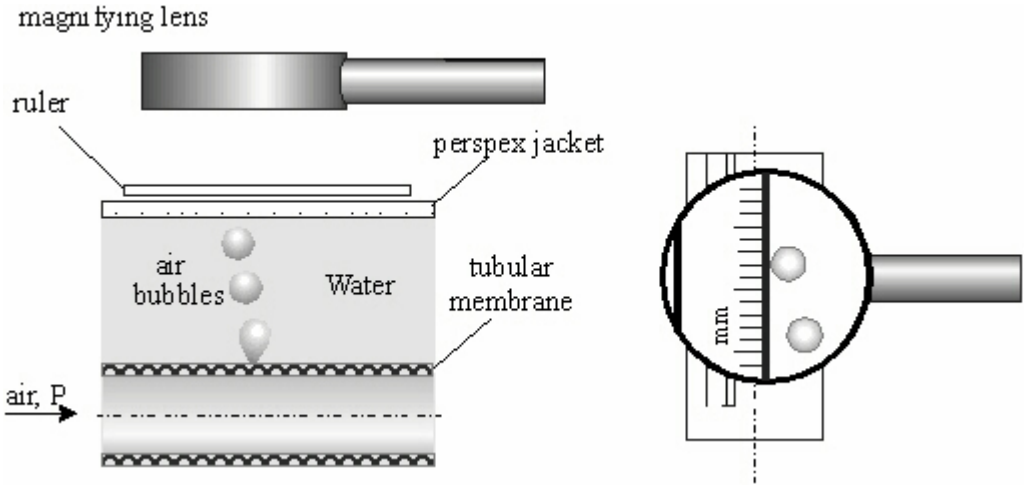

Figure 4-3. Schematic diagram of the bubble-point method.

4.3. Hydrodynamic Properties of the Tubular Membrane Module

In practical application the module hydrodynamic properties have a great influence on the process operation and control. Some hydrodynamic properties of the system were therefore evaluated.

4.3.1. Equivalent Diameter of The Module

The central bar which generally works as an anode, has a diameter d_1=8mm, and the tubular membrane has a diameter d_2=13.5mm. The equivalent diameter of the module is

$$\mathbf{d_e} = \mathbf{d_2} - \mathbf{d_1} = 13.5 - 8 = 5.5(\mathbf{mm}) \qquad (4\text{-}3)$$

The gap between the central bar and the membrane is

$$\varepsilon = \frac{\mathbf{d_2} - \mathbf{d_1}}{2} = \frac{1}{2}\mathbf{d_e} = 2.75(\mathbf{mm}) \qquad (4\text{-}4)$$

The effective length of the tubular membrane in the module is

$$\ell = 380(\mathbf{mm}) \qquad (4\text{-}5)$$

4.3.2. Flow Velocity and Pressure

As in dead end filtration, pressure difference is the driving force for separation in cross

flow filtration. The only difference is that in cross flow filtration the pressure drop from inlet to outlet provide a tangential flow velocity to reduce the membrane fouling. Clearly, there are two related pressure drops to be distinguished: the hydrostatic pressure drop ($\Delta P_H = P_{in} - P_{out}$) and the transmembrane pressure drop ($\Delta P_{TM} = \frac{1}{2}(P_{in} + P_{out}) - P_{per}$).

For most biological applications, once fouling is established, the permeate flow is always insignificant compared to the retentate flow. The permeate flux would not have a major influence on the hydrostatic pressure drop of the module, and the permeate valve X_P can approximately be considered closed when we contemplate the relation between flow velocity and pressure drop along the membrane. Figure 4-4 shows the results of measurement of velocity and pressure drop along the membrane with the permeate valve X_P closed. Since the structural parameters for both the 5μm and the 25μm module are the same, this results are applicable to both of them.

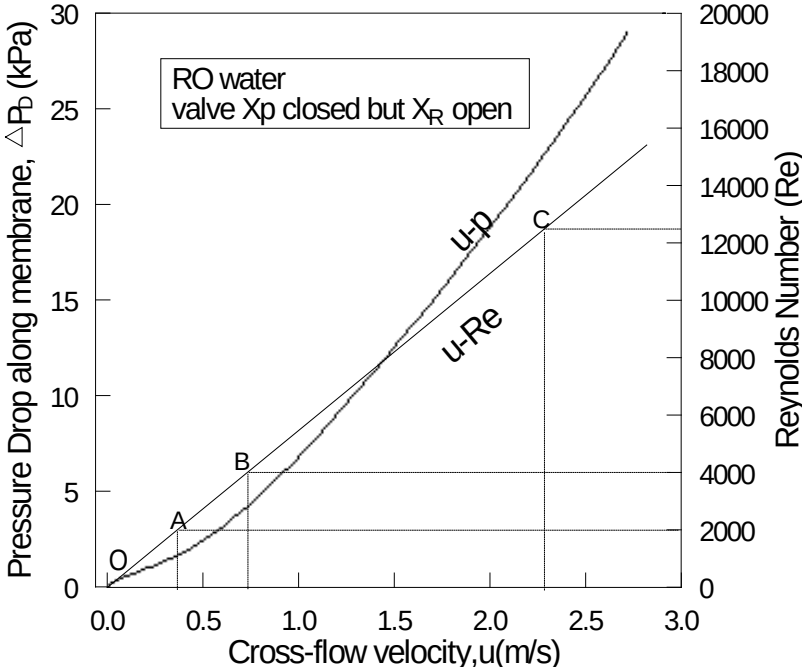

Figure 4-4. Cross-flow velocity vs pressure drop and *Reynolds* Number, permeate valve X_P was closed during the measurement

In this research many of the experiments were performed under the cross flow velocity of 2.28m/s (see figure 4-4 at point C), the corresponding *Reynolds* number was

$$\mathrm{Re} = \frac{\mathbf{d_e u}\rho}{\mu} = \frac{5.5\times10^{-3}(\mathbf{m})\times 2.28(\mathbf{m}\cdot\mathbf{s}^{-1})\times 998.2(\mathbf{kg}\cdot\mathbf{m}^{-3})}{100.42\times10^{-5}(\mathbf{Pa}\cdot\mathbf{s})} = 1.25\times10^{4} \qquad (4\text{-}6)$$

where $\mathbf{d_e}$ the equivalent diameter of the module, **u** the cross flow velocity, ρ the density of fluid (e.g. ρ=998.2kg/m^3 for water at 20°C), and μ the viscosity of fluid (e.g. μ=100.42×10^{-5} Pa·s for water at 20°C).

As we can see from Figure 4-4, in low flow velocity range OA(e.g. from 0 to 0.4m/s), where the flow pattern is in the laminar region, the pressure drop along the membrane tuber is directly proportional to the cross flow velocities **u**, and the corresponding *Reynolds* number is under 2000. The relation is given by *Poiseuille*'s equation:

$$\Delta\mathbf{P_H} = \frac{32\mu\ell\mathbf{u}}{\mathbf{d_e^2}} \qquad (4\text{-}7)$$

In the higher velocity range the curve u-p began to deviate from the straight line. The flow range AB, where the *Reynolds* number lies between 2000 ~ 4000 (velocity 0.4~0.7 m·s^{-1}) is known the transitional region. The laminar flow is rapidly changing to the turbulent flow, and the flow resistance will change from linear area to the so called resistant two power area, i.e. the value of pressure drop will be proportional to the flow velocity to the 1.8 ~ 2 power (i.e. $\Delta\mathbf{P_H} = \propto \mathbf{u^n}$, and n=1.8~2).

4.3.3. Momentum Equation of the Boundary Layer [38]

Cross flow membrane filtration in tubular modules are normally operated at a high flow velocity to reduce membrane fouling, especially in microfiltration, and the flow patterns are consequently usually turbulent. To obtain a higher cross flow velocity will also result in a greater hydrostatic pressure drop, so the hydrodynamic properties of the module are important to the process of cross flow microfiltration. Moreover, since the separation is achieved by flow through the membrane, significant tangential velocity and radial velocity gradients exist in the vicinity of the membrane surface, thus the characteristics of the flow velocity boundary layer will reflect the hydrodynamic properties of the module.

On the other hand, if a electric field is applied during the microfiltration, electrophoretic movement of the particles will result. Compared to the tangential velocity of the bulk solution, however, the radial electrophoretic velocity is always much slower. The effect of the electric field will be mainly located in the flow velocity boundary layer on the membrane surface.

Boundary layer theory considers that a thin fluid layer exists in the vicinity of solid wall at high *Reynolds* number flow, in which there is a high velocity gradient perpendicular to the solid wall. The tangential flow velocity increases from zero at the wall surface to the value of the outer edge bulk solution velocity $\mathbf{u_s}$ within a extremely short distant. When a fluid flows over a flat surface, formation and development of the boundary layer occurs as shown in Figure 4-5. The thickness of the laminar boundary layer at the distant **x** from the leading edge can be expressed as the function of *Reynolds* number with respect to distant **x:**

$$\frac{\delta}{\mathbf{x}} = \frac{4.96}{\sqrt{\mathrm{Re}_{\mathbf{x}}}} \qquad (4\text{-}8)$$

where

$$\mathrm{Re}_{\mathbf{x}} = \frac{\mathbf{u}_s \mathbf{x} \rho}{\mu} \qquad (4\text{-}9)$$

and $\mathbf{u_s}$ is the flow velocity in the outer edge of the boundary layer. When $\mathrm{Re}_{\mathbf{x}}$ exceeds a certain value, the flow pattern in the boundary layer will transform from laminar flow to turbulent flow, nevertheless, between the turbulent boundary layer and the wall surface there will still exist a thinner laminar sub-layer and a buffer layer above, which can normally be ignored. From laminar boundary layer to turbulent boundary layer, the transition area falls into the range of $\mathrm{Re}_{\mathbf{x}}=5\times10^5\sim3\times10^6$.

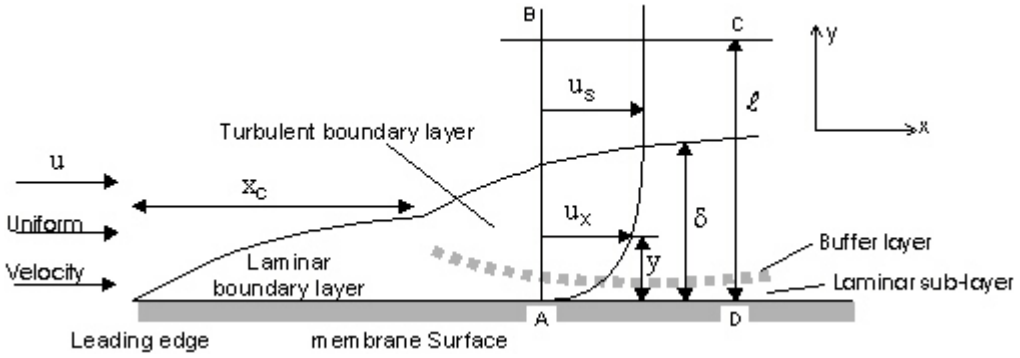

Figure 4-5. Formation and development of the flow boundary layer.

At the outlet of the membrane module used in this study, according to Eq. (4-9), the *Reynolds* number with respect to distant **x** is 1.12×10^6 when the average flow velocity is u=2.28m·s^{-1} , and axial velocity $\mathbf{u_s}$=2.28/0.81 =2.81m·s^{-1}, so the boundary layer is already turbulent.

When applying *Newton's* second law to a fluid unit which contain the thickness of the boundary layer (e.g. the square □ABCD in figure 4-5), the integrative momentum equation describing the boundary layer can be deduced, which is also known as the *Karman* integrative momentum equation:

$$\rho\frac{\partial}{\partial \mathbf{x}}\int_0^{\ell}(\mathbf{u_s}-\mathbf{u_x})\mathbf{u_x}\mathbf{dy} = -\mathbf{R}_0 \qquad (4\text{-}10)$$

where ρ is the density of fluid, $\mathbf{R_0}$ the shear force acting on the surface, $\mathbf{u_s}$ the flow velocity outside the boundary layer, $\mathbf{u_x}$ the flow velocity inside the boundary layer in X-direction, ℓ the distance from the surface which is greater than the boundary layer thickness δ. In engineering, commencing from the *Karman* integrative momentum equation, the solutions and results are often used to analyze and calculate approximately the hydrodynamic properties of the flow boundary layer

4.3.4. Critical length x_c

This is a length beyond the leading edge after which the boundary layer would develop into the turbulent regime. One of the results from the solution of *Karman* equation is:

$$\delta = 0.376\mathbf{x}^{0.8}\left(\frac{\mu}{\mathbf{u_s}\rho}\right)^{0.2} \tag{4-11}$$

where δ is the thickness of fully developed flow boundary layer. In this study δ equals the half gap between the central bar and the membrane, i.e. $\delta=\varepsilon/2=(d_2-d_1)/4=1.375$mm, (see Figure 4-6), so

$$\begin{aligned}\mathbf{x_c} &= \left[\frac{\delta}{0.376}\left(\frac{\mathbf{u_s}\rho}{\mu}\right)^{0.2}\right]^{1.25} \\ &= \left[\frac{1.37\times10^{-3}\mathbf{m}}{0.376}\left(\frac{2.78\mathbf{m\cdot s^{-1}}\times 998.2\mathbf{kg\cdot m^{-3}}}{100.42\times10^{-5}\mathbf{Pa\cdot s}}\right)\right]^{1.25} \\ &= 3.68\times10^{-2}\mathbf{m} = 3.68\mathbf{cm}\end{aligned} \tag{4-12}$$

The effective membrane tube length is 38cm, or about ten times $\mathbf{x_c}$. This means the flow pattern in almost the whole length of the tube is fully developed turbulent flow.

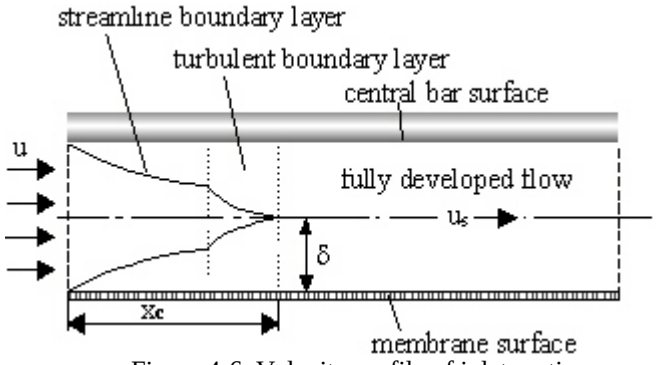

Figure 4-6. Velocity profile of inlet section

4.3.5. Flow Velocity Distribution In The Tube

The velocity distribution under turbulent flow condition can be assumed to obey the *Prandtl* one-seventh power law and is given by the *Blasius* equation as follows:

$$\frac{\mathbf{u_x}}{\mathbf{u_s}} = \left(\frac{\mathbf{y}}{\mathbf{r}}\right)^{1/7} = \left(\frac{\mathbf{y}}{\delta}\right)^{1/7} = \left(\frac{2\mathbf{y}}{\varepsilon}\right)^{1/7} \qquad (0<y<\delta) \tag{4-13}$$

or

$$\begin{aligned}\frac{\mathbf{u_x}}{\mathbf{u}} &= \frac{1}{0.82}\left(\frac{2\mathbf{y}}{1.375\times10^{-3}}\right)^{1/7} \qquad (0<y<\delta) \\ &= 2.32\mathbf{y}^{1/7}\end{aligned} \tag{4-14}$$

where **u** is the mean velocity of flow, $\mathbf{u}_x$ the cross flow velocity in x-axial direction at position **y**, $\mathbf{u}_s$ the maximum velocity, and the integration result of $\mathbf{u}=0.82\mathbf{u}_s$ was applied.

Nevertheless, the *Blasius* equation can not be applied to the point of y=0 , because its differentiation with respect to y (i.e. the velocity gradient) gives an infinite value:

$$\left.\frac{\partial \mathbf{u}_x}{\partial \mathbf{y}}\right|_{\mathbf{y}=0} = \left.\frac{1}{7}\mathbf{u}_s\delta^{-1/7}\mathbf{y}^{-6/7}\right|_{\mathbf{y}=0} \to \infty \qquad (4\text{-}15)$$

This is in contradiction to the conditions which have been seen to exist in the stream. However, little error will be introduced by using this relation for the whole of the boundary layer in the momentum equation, since the velocities and hence the momenta near the surface are very low and it gives the correct value of the velocity at the edge of the boundary layer.

In the laminar sub-layer, since it is very thin, the velocity gradient within it can therefore be taken as constant:

$$\frac{\partial \mathbf{u}_x}{\partial \mathbf{y}} = \frac{\mathbf{u}_b}{\delta_b}, \qquad (0 \le \mathbf{y} \le \delta_b) \qquad (4\text{-}16)$$

and

$$\mathbf{u}_x = \left(\frac{\mathbf{u}_b}{\delta_b}\right)\cdot \mathbf{y}, \quad (0 \le \mathbf{y} \le \delta_b) \qquad (4\text{-}17)$$

where δ_b is the thickness of the laminar sub-layer and $\mathbf{u}_b$ the velocity at the edge of the laminar sub-layer. They will be given in the next two sections, respectively (4.3.6 and 4.3.5) This result proves to be useful when analyzing the fluid drag force acting on a deposited particulate on the membrane surface (see 5.4.1).

4.3.6.Thickness of The Laminar Sub-layer on The Membrane

When the average velocity is $u=2.28 m\cdot s^{-1}$, the corresponding *Reynolds* number in the module is $Re=1.25\times10^4$ (see section 4.3.2.). The thickness of the laminar sub-layer is then given as:

$$\begin{aligned}\delta_b &= 56.52\mathbf{d}_e\,\mathrm{Re}^{-7/8} \\ &= 56.52\times 5.5\times 10^{-3}\times(1.25\times 10^4)^{-7/8} \\ &= 81\times 10^{-6}\,\mathbf{m} = 81\mu\mathbf{m}\end{aligned} \tag{4-18}$$

This is many times of the Alamin particle mean size (see section 3.4.2.).

4.3.7. The Velocity at The Edge of The Laminar Sub-layer

This value ($\mathbf{u_b}$) is needed when calculating the velocity gradient within the laminar sub-layer mentioned in 4.3.5. It is related with the axial velocity $\mathbf{u_s}$ by the following equation:

$$\frac{\mathbf{u_b}}{\mathbf{u_s}} = 1.87\left(\frac{\mu}{\mathbf{u_s}\delta\rho}\right)^{1/8} \tag{4-19}$$

where δ is the thickness of the flow boundary layer for a fully developed flow in the membrane module used in this study (See 4.3.4. and Figure 4-6). The thickness of boundary layer δ can be expressed as half of the gap between two cylinders,

$$\delta = \frac{\varepsilon}{2} = \frac{\mathbf{d}_2 - \mathbf{d}_1}{4} = \frac{1}{4}\mathbf{d_e} \tag{4-20}$$

where $\boldsymbol{\varepsilon}$ is the gap between the membrane and the central bar, $\mathbf{d}_2$ and $\mathbf{d}_1$ the diameters of the membrane tube and the central bar respectively, and $\mathbf{d}_e$ the equivalent diameter of the module. Since $\mathbf{u}=0.82\mathbf{u_s}$, so

$$\begin{aligned}\frac{\mathbf{u_b}}{\mathbf{u}} &= \frac{1.87}{0.82}\left(\frac{0.82\times 4\mu}{\mathbf{d_e u}\rho}\right)^{1/8} \\ &= 2.65\,\mathrm{Re}^{-1/8}\end{aligned} \tag{4-21}$$

or

$$\begin{aligned}\mathbf{u_b} &= 2.65\mathbf{u}\cdot\mathrm{Re}^{-1/8} \\ &= 2.65\times 2.28\times(1.25\times 10^4)^{-1/8} \\ &= 1.86\,\mathbf{m/s}\end{aligned} \tag{4-22}$$

This value is about 82% of the average flow velocity ($\mathbf{u}$) and 67% of the axial velocity ($\mathbf{u_s}$).

4.3.8. The Shear Stress on The Membrane Surface

Blasius has given an approximate expression for the shear stress ($\mathbf{R_0}$) at a plane smooth surface over which a fluid is flowing with a velocity $\mathbf{u}_s$ for conditions where $Re_x < 10^7$. The equation is as follows:

$$\frac{\mathbf{R}_0}{\rho_{\mathbf{w}}\mathbf{u}_{\mathbf{s}}^2} = 0.0228\left(\frac{\mu}{\mathbf{u_s}\delta\rho_{\mathbf{w}}}\right)^{0.25} \qquad (4\text{-}23)$$

Substituting the δ and $\mathbf{u}=0.82\mathbf{u_s}$ to the *Blasius* equation, we have

$$\begin{aligned}\mathbf{R}_0 &= 0.0456(\rho_{\mathbf{w}}\cdot\mathbf{u}^2)\,\mathrm{Re}^{-1/4}\\ &= 0.0456\times 998.2\mathbf{kg}\cdot\mathbf{m}^{-3}\times(2.28\mathbf{m}\cdot\mathbf{s}^{-1})^2\times(1.25\times10^4)^{-1/4}\\ &= 22.38\mathbf{N}\cdot\mathbf{m}^{-2}\end{aligned} \qquad (4\text{-}24)$$

A mean size Alamin particle with 4.63μm in diameter occupies an area of 1.55×10^{-11} (m^2) on membrane surface. This area will share a shear stress of $\mathbf{R_0}\cong3.47\times10^{-10}$ (N). It is about one-sixth of the viscous drag force ($\mathbf{F_D}$) acting on this particle (see 5.2.1 for details).

4.4. Uncharged Membrane Microfiltration

4.4.1. Microfiltration of Calcite and Alamin

The newborn calcite particle* suspension was first used in an experiment where no electric charge was applied. The solids content of the suspension was about 1%(w/v). The permeate was initially slight turbid and the light absorbance was measured with a spectrophotometer at 360nm. The absorbance, like the flux, declined until a clear permeate was obtained. For the 5μm membrane the permeate became visibly clear (absorbance<0.01) within 5 minutes of the start of filtration(Figure 4-7). For the 25μm membrane this took about 7 to 8 minutes (Figure 4-8). The reason that the initial permeate was slight cloudy can be explained by the existence of a large number of tiny particles in the newborn calcite suspension. The dimension of these particles were below the nominal membrane pore size, but

* A suspension of calcite particles obtained from chemical deposit reaction and not yet subject to washing or filtration.

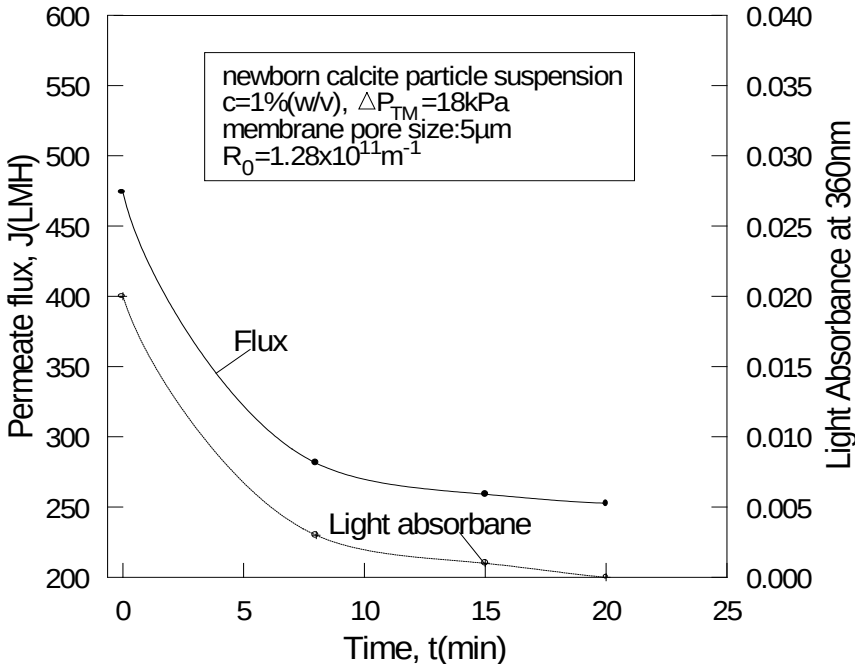

Figure 4-7. Permeate flux and light absorbance for processing of Newborn calcite with the 5μm membrane

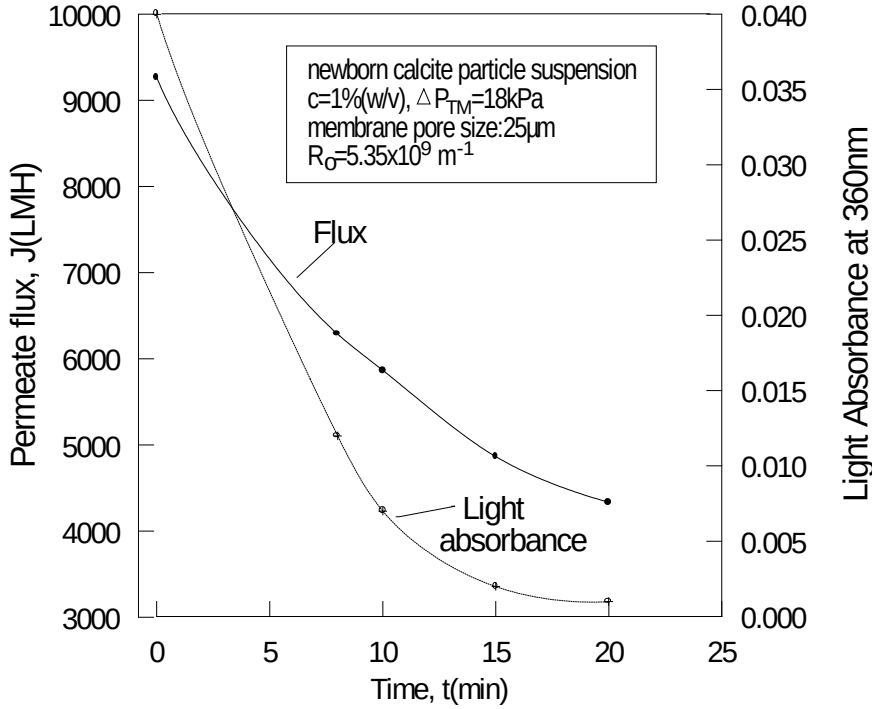

Figure 4-8. Flux and light absorbancy of newborn calcite on 25μm membrane

their mass comprised just a very small part of the total mass of calcite particles. The clarification of the permeate stream indicated that the retention of these particles on a filtration cake on the membrane surface or inside the pore mouths was established.

The behavour of the normal calcite suspension[1] filtered with the 25μm membrane is shown in Figure 4-9. The initial permeate flux in the first 10 minutes showed a rapid decrease, indicating serious membrane fouling under the transmembrane pressure of 35kPa. A steady state permeate flux was achieved about 100 minutes later. This result is consistent with the work of Reeve(1997). If the pump speed and all valve openings remained unchanged, the transmembrane pressure was observed to increase from 35kPa in the beginning to 65kPa at the end of the run.

For the 5μm pore size membrane, the experimental result is shown in Figure 4-10. The profile of permeate flux versus time was similar on the 25μm membrane, when the transmembrane pressure and the cross flow velocity were controlled at approximately the same levels. The results indicated: (1)the steady state permeate flux of the 25μm membrane was 10-fold that of the 5μm membrane, and (2)the transmembrane pressure on the 25μm membrane underwent a significant change (from 36kPa to 65kPa), while it was almost stable on the 5μm membrane if valve openings remained unchanged during the filtration period. This is a remarkable difference between the two kinds of membrane. The reason for this was the high permeate flux and its greater relative amplitude change on the 25μm membrane (e.g. from 14050 decreased to below 1000 LMH). The initial flow velocity in the permeate line was so high that the permeate back-pressure $\mathbf{P_{per}}$ was thus considerably increased. For instance, the $\mathbf{P_{per}}$ was 15kPa at the beginning and approached to zero after about 60mins in the experiment shown in Figure 4-9. However the permeate back-pressure $\mathbf{P_{per}}$ on the 5μm membrane was always at a low level (e.g. <5kPa)

[1] The particle suspensions after being filtrated and washed

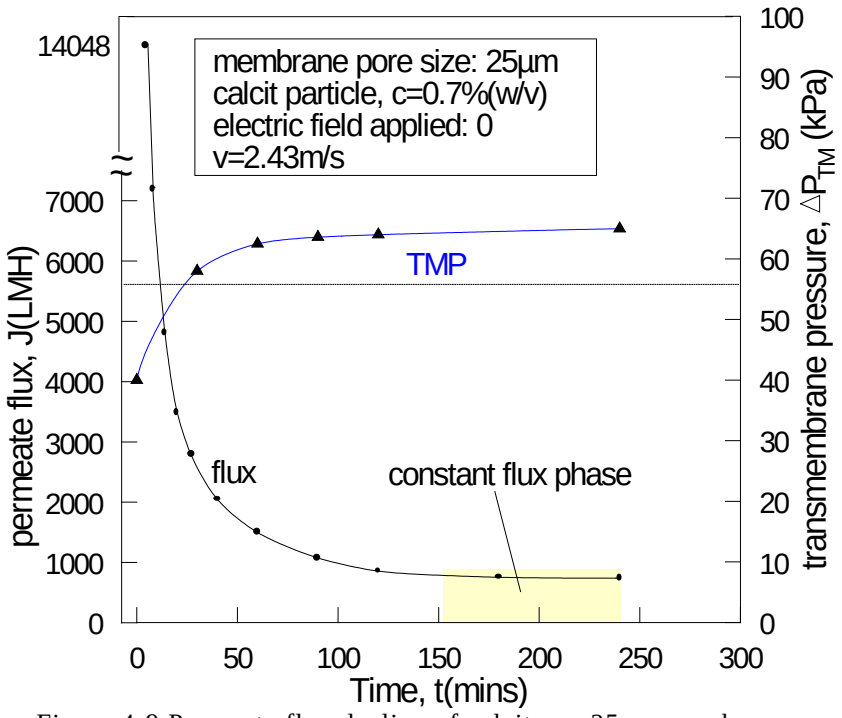

Figure 4-9 Permeate flux decline of calcite on 25µm membrane

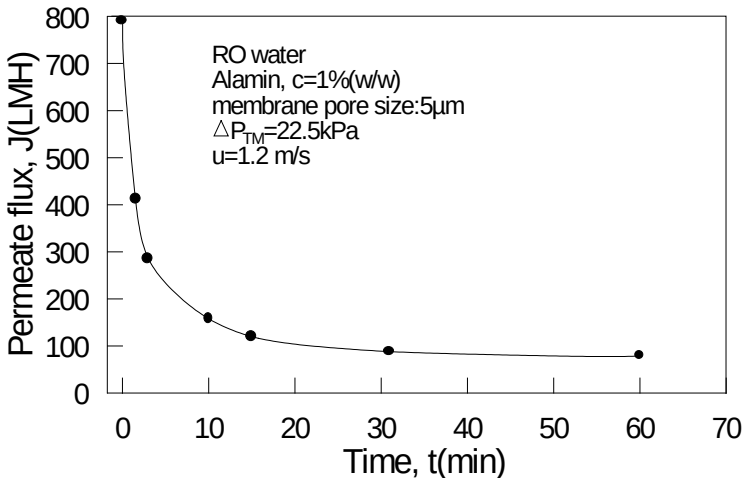

Figure 4-10. Permeate flux decline for the Alamin on the 5µm membrane

4.4.2. Effect of Cross Flow Velocity

The influence of cross flow velocity was also studied (Figure 4-11). Experiments were performed on the 5µm membrane under the same transmembrane pressure(50kPa) but at different cross flow velocities (2.28m/s;1.54m/s;1.25m/s).

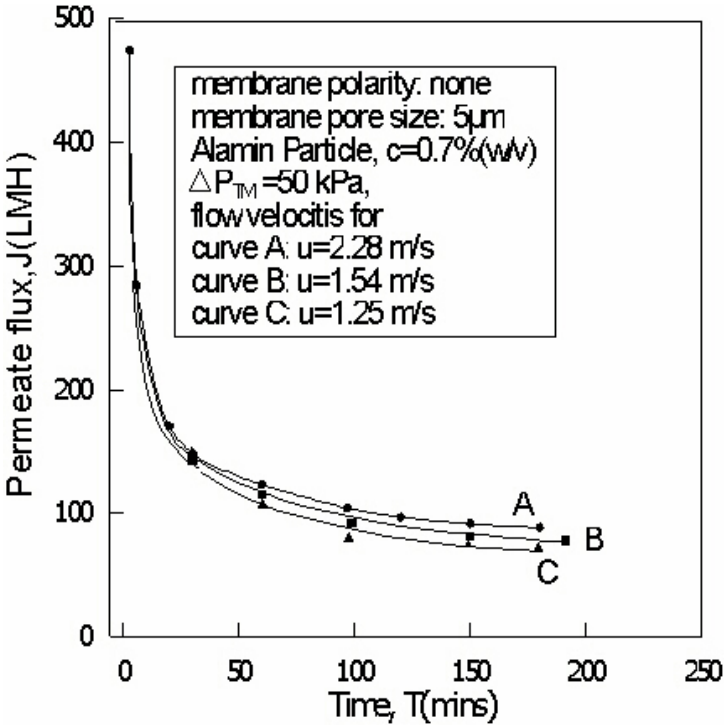

Figure 4-11. Flux decline at different cross-flow velocities.

The profiles of the permeate flux curves in three runs are similar. About 16% of steady-state permeate flux gain was obtained (from 78LMH to 90LMH) when the cross flow velocity increased by 82% (from 1.25m/s to 2.28m/s). This result can be compared with the work of Reeve (1997) who observed that when the cross flow velocity increase from 1.1m/s to 1.8m/s (increased by 64%), the steady-state permeate flux increased from 1000LMH to 1500LMH (flux gain was 50%) on the 25μm membrane. If all the particles is retained by the membrane ($\mathbf{C_p}$=0), one of the analytical expression for permeate flux is [1]:

$$\mathbf{J} = \mathbf{k}\ln(\mathbf{C_m}/\mathbf{C}) \qquad (4\text{-}25)$$

where $\mathbf{C_m}$ is the particle concentration on the membrane surface; **C** is the particle concentration in bulk solution and **k**(=D/δ) the transport coefficient. In turbulent flow:

$$\mathbf{k} = 0.023\frac{\mathbf{u}^{0.8}\mathbf{D}^{0.67}}{\mathbf{d_h}^{0.2}}\left(\frac{\rho}{\mu}\right)^{0.47} \qquad (4\text{-}26)$$

Where **D** is the diffusion coefficient of the particle; $\mathbf{d_h}$ the equivalent dydraulic diameter; μ the viscosity of the solvent (e.g. water). Therefore the flux is:

$$\mathbf{J} = 0.023\frac{\mathbf{u}^{0.8}\mathbf{D}^{0.67}}{\mathbf{d_h}^{0.2}}\left(\frac{\rho}{\mu}\right)^{0.47}\ln(\mathbf{C_m}/\mathbf{C}) \quad \text{or } \mathbf{J}=\mathbf{K'}\cdot\mathbf{u}^{0.8} \qquad (4\text{-}27)$$

Where $\mathbf{K'} = 0.023\frac{\mathbf{D}^{0.67}}{\mathbf{d_h}^{0.2}}\left(\frac{\rho}{\mu}\right)^{0.47}\cdot\ln(\mathbf{C_m}/\mathbf{C})$ is again a positive constant[1]. So the Eq.(4-27) shows that a higher cross flow velocity (**u)** generally gives a higher permeation rate. However, one can not unlimitedly increase the velocity to get higher flux rate for a given membrane module.

For example, the results for this set of runs were obtained under the same transmembrane pressure but at different cross flow velocities (by reducing the pump speed and turning down the retentate valve X_R , while keeping the permeate valve X_P fully opened). Although the cross flow velocity could be further increased to a higher level (e.g., u>2.5m/s) under the same transmembrane pressure (by reversely increasing the pump speed and reducing the valve opening on permeate line, while keeping the retentate valve X_R fully opened), a repeatable higher steady-state permeate flux was not observed. Tarlton and Wakeman (1994) also observed some unusual results where a nominal pore size membrane of 0.2μm was used for the filtration of calcite suspensions. When the feed stream contained a greater proportion of larger, ungrounded particles with a mean size of 24μm, the filtration rate was seen to fall with increasing cross-flow velocity ($\mathbf{u}_{cf}$) despite a substantial thinning of the fouling layer at the higher cross flow. They suggest that this may be due to the cake at the membrane surface consisting of smaller particles being preferential deposited with increasing crossfllow velocity. These observations indicate that there exist a value of cross flow velocity beyond which a higher permeate rate can not be obtained by increasing the cross flow velocity. This shows the limitation of Eq. (4-27). To understand this better, a further discussion followes and is illustrated with Figure 4-12.

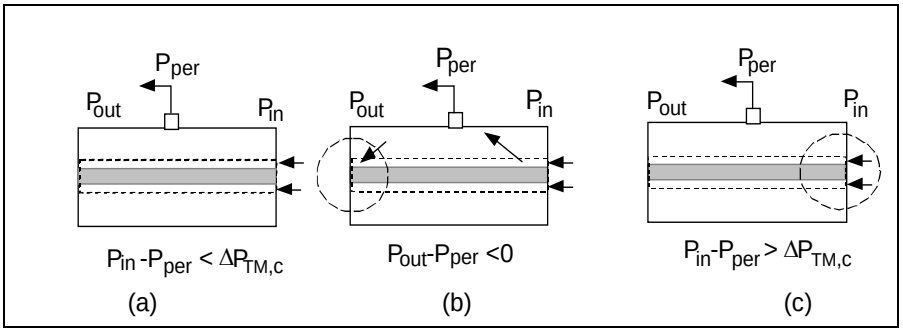

Figure 4-12. Three operating condition and the fouling mechanisms

When experiments are performed under a moderate condition of transmembrane pressures and cross flow velocities, increase of the cross flow velocity generally results in an improved permeate flux (Figure 4-12a). However, higher cross flow velocity will unavoidably cause a greater hydrodynamic pressure drop along the membrane tube and a increase of average feed pressure. In order to maintain an iso-transmembrane-pressure condition, the valve X_{per} on permeate side has to be turned down to raise permeate back pressure ($\mathbf{P_{per}}$). When the feed stream pressure increases to a certain extent, two consequences would possibly occur:

Firstly, the permeate back pressure ($\mathbf{P_{per}}$) surpass over the retentate outlet pressure ($\mathbf{P_{out}}$), so a portion of the permeate will return to the feed side of the membrane. Reeve (1997) noticed the possibility of the effect as well[15]. This precludes any increase in permeate flux by further raising the cross flow velocity (Figure 4-12b). Nevertheless, this situation is unlikely to occur unless the flow resistances both along the membrane tube and on the permeate line are so high (e.g. by improperly placing baffles to enhance flow turbulence, or the ratio of length and diameter of the membrane module, ℓ/d, being too high), they force the feed stream to 'detour' from the permeate side back to the feed side again, as shown in Figure 4-12b. Proper design of the membrane module can prevent this happening.

Secondly, the local transmembrane pressure close to the inlet section can be so high that a 'critical transmembrane pressure' ($\Delta\mathbf{P_{TM,c}}$) is achieved or exceeded . Here it is supposed there exists a threshold of pressure difference across the membrane ($\Delta P_{TM,c}$) beyond which the scouring action of the cross flow on the deposition is surpassed by pore plugging and membrane caking. This effect can develop from the entrance to the entire membrane (Figure 4-12c), and the situation can be aggravated if the particles used have a wide range of size distribution and a smaller mean size than the nominal membrane pore size.

The above discussion can be illustrated mathematically based on the transmembrane pressure equation (3-1), i.e. $\mathbf{\Delta P_{TM}=(P_{in}+P_{out})/2 - P_{per}}$, which can be modified as:

$$\Delta\mathbf{P_{TM}} = \tfrac{1}{2}(\mathbf{P_{in}} - \mathbf{P_{per}}) + \tfrac{1}{2}(\mathbf{P_{out}} - \mathbf{P_{per}}) \qquad (4\text{-}28)$$

There are three operating conditions that can be identified from this equation. They are:

(a) $\mathbf{P_{in}-P_{per}<\Delta P_{TM,c}}$, this is the normal operating condition under which increasing cross flow velocity results in an improvement of permeate flux. It corresponds to the situation in Figure 4-12a.

(b) $\mathbf{P_{out}-P_{per}<0}$, this is the consequence of over increasing of the cross flow velocity by over applying the feed pressure, while restricting the permeate flux to control the transmembrane pressure. It results in the permeate re-entering the membrane feed side (Figure 4-12b).

(c) $\mathbf{P_{in}-P_{per}>\Delta P_{TM,c}}$, the reason by which this occurs is the over raising of transmembrane pressure. It is commonly characterized by a sharp initial drop of permeate flux and is corresponds to the case of Figure 4-12c.

4.4.3. Effect of pH

The Alamin suspension was a strong buffer solution, because considerable HNO_3 or NaOH was needed to adjust its pH. For example, to reduce the pH of 10 liters of 0.7% (w/v) Alamin suspension from pH7 to pH5, about 11ml of HNO_3(70%) were needed (for RO water, no more than 1ml of HNO_3 was needed). This was not surprising, as phosphate is commonly used in various buffer solutions. Following acidification, the upper liquid layer of the Alamin suspension after deposition looked clearer than it was before, implying that some of suspended particles in the solution might have dissolved. This is because the smallest crystal particles, according to the theory of crystallization, have a higher solubility than the macro-size particles (the so-called Gibbs–Thomson effect[7]). Observation with a microscope revealed that the dissolving pH of Alamin particle is at about 4.9, but the dissolving pH will likely be higher for those particles under ~10^{-1} μm.

The results of processing Alamin suspensions at different pH are shown in Figure 4-13. In this set of runs, the solid content of the suspension was not measured after adjusting the pH. Nevertheless the lower permeate flux obtained at a high pH (pH>9)

is consistent with the work of Reeve (1997) where calcite particles were used. These results can be explained by the solubility of calcium salts which is sensitive to the variation of pH. After the Alamin solution was alkalized, large number of newly-formed tiny particles of calcium salt would appear in the solution.

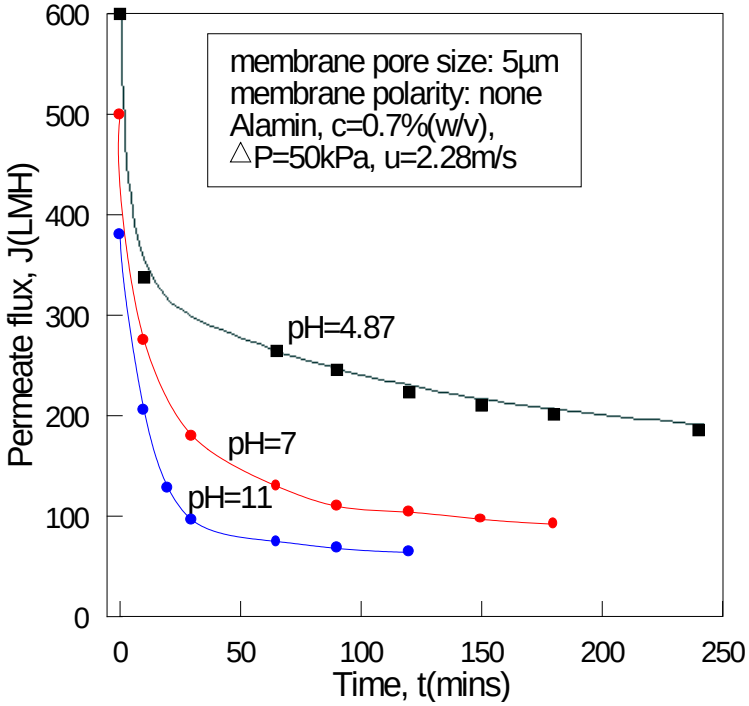

Figure 4-13. Flux decline in different pH conditions for Alamin

This behavior of the Alamin solution will be further revealed when the clear permeate is made alkaline by electrolysis and will be discussed in the next section (4.5). Since the solubility of calcium salt is very low compared to the solid content of the suspension (e.g. the solubility of calcium carbonate is 1.53×10^{-3} g/100gH_2O at room temperature [34]. Whereas the solid content in the suspension for this study was ~0.7g/100gH_2O), these newborn particles will not greatly alter the solid content of the suspension. However because of their surface activity and their being much smaller than the nominal membrane pore size, they are probably more susceptible to be adsorbed by the membrane and to induce serious fouling. The inference from this results provides further evidence that the major fouling mechanism on the membrane used in this study is pore plugging and/or inner pore adsorption.

4.5. Charged Membrane Microfiltration

The justification for applying an electric field is the charge property of particles in colloidal system (e.g. particles are usually negatively charged). If the membrane is negatively charged, particles will be subject to electric repulsion by the membrane and consequently the membrane fouling will be reduced. The electric force acting on the charged particles will be analyzed in chapter 5. In this section the characteristics of charged microfiltration for Alamin were studied, and calcite was used in final experiments for comparison.

4.5.1. Membrane Polarity and Its Characteristics

Some electrochemical characteristics of the membrane are shown in Figure 4-14 and Figure 4-15 where the membrane worked as cathode and anode, respectively. The electrode current in both cases was approximately proportional to the voltage applied. It was found that when the membrane was negatively charged (worked as a cathode), the membrane current was double the case where the membrane was positively charged at the same voltage. Since the area of the membrane was about 1.7-fold that of the central bar, and taking the membrane's surface roughness into consideration, the actual area of membrane would be almost double that of the central bar. This implies that the cathode area dominate the electrolytic current in this system. It can be explained by the fact that the hydrogen ion (H^+) has the fastest electrophoretic velocity amongst all the ions and it is the only ion that is subject to the electrode reaction on the cathode. Thus larger cathode area will allow more hydrogen ions to reduce to hydrogen gas at the same time and result in a higher electrode current.

In the solution, the RO water itself has a very low electrical conductivity. The electrical conductivity was mainly attributed to the calcite (or Alamin) particles

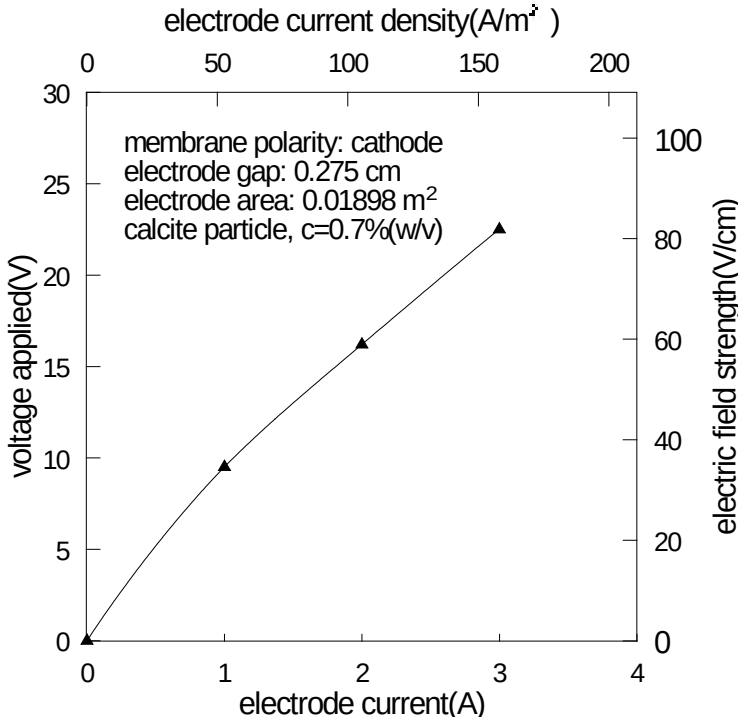

Figure 4-14. Dependence of electrode current on voltage applied when the membrane was negatively charged

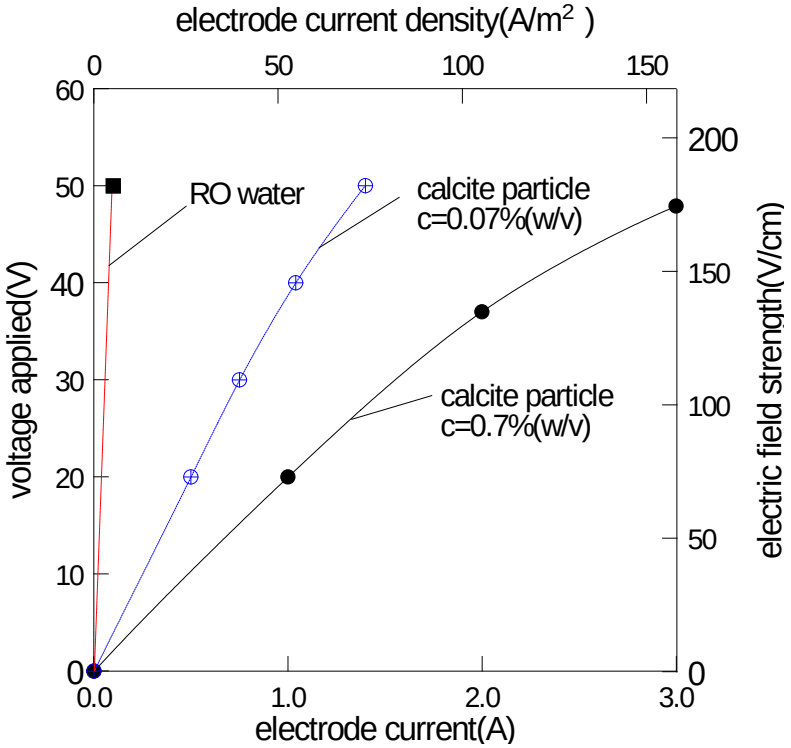

Figure 4-15. Dependence of electrode current on the voltage applied when the membrane was positively charged.

and the impurities that came with the particles.

The experiments shown in Figure 4-14 and Figure 4-15 were performed on the 25μm membrane. Since the electric resistance is independent of the membrane pore size, these electric properties are also applicable to the 5μm membrane.

4.5.2. EMF with a Negatively Charged Membrane

Figure 4-16 show the result of microfiltration of Alamin in which the electric field was applied at about 40 minutes after the filtration started. When the DC power was switched on, the permeate flux increased almost immediately. After reaching to a maximum, it started to decline again gradually. The initial flux gain ($\Delta\mathbf{J}$) was about 20 $l \cdot m^{-2} \cdot h^{-1}$ compared to the operation without electric field. The lower dashed line on the figure represents a virtual permeate flux for uncharged operation.

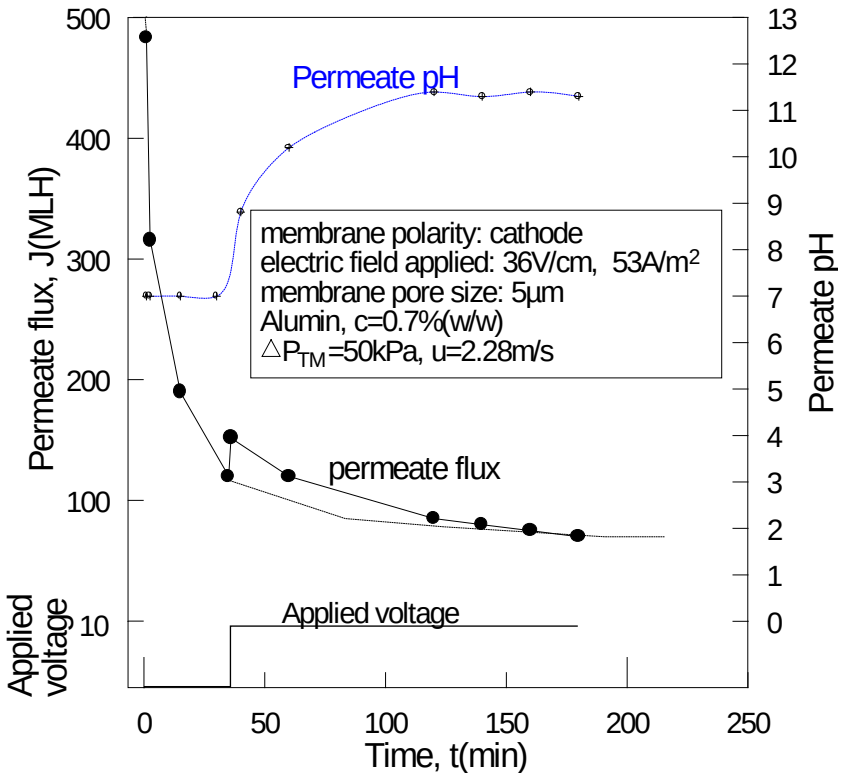

Figure 4-16. Influence of the electric field to the flux decline

Discontinuous application of the electric field was also examined and the data are shown in Figure 4-17, where the membrane was negatively charged. The amplitude of

voltage was 50V(DC), i.e. about 180V·cm^{-1} electric field strength. The electric charge time was 2 minutes. The membrane current was 1.2A, i.e. giving a current density of 63 A·m^{-2} .

It was observed that the permeate carried some volumes of cathode gas bubbles produced by electrochemical reaction and the permeate flowmeter reading increased as a result of applying the electric field. The volume of gas bubbles would certainly have disturbed the flow measurement and increased measurement error. For this reason the experimental rig was modified to provide a gas-releasing channel to reduce the bubbles influence (Figure 3-2). However a few gas bubbles still pass through the flowmeter occasionally. Moreover, the period required to establish the voltage was very short and a large amount of gas bubble formed in the permeate after the power was switched on. The volume of these bubbles would push the flowmeter reading up straight away, despite the gas bubbles having not arrived at the flowmeter yet.

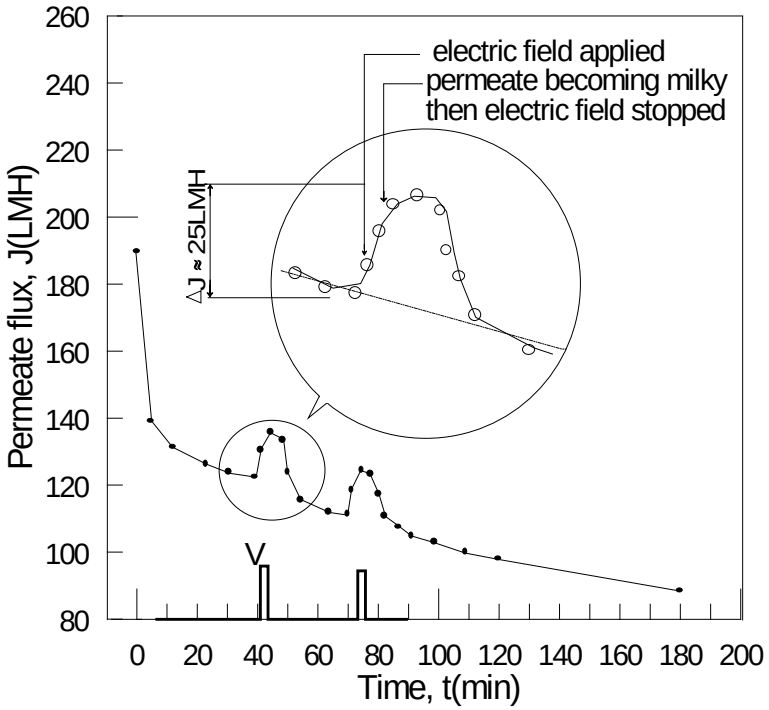

Figure 4-17. Segmented application of electric field to the microfiltration of Alamin
membrane pore size: 5μm
pH=7, $\triangle P_{TM}$=6.5KPa, u=0.7m/s
EF: 180V/cm, 63.22 A/m^2

The reason for emphasizing the bubble effect is that this seems not to be mentioned and taken into consideration by some researchers (Wakemam,1986; Wakemam & Sabri 1995; Reeve, 1997). For example, the permeate flux gain obtained by Wakeman and co-workers[10] was 1000~2000LMH, where the microfiltration of titanium dioxide was performed on a stainless steel membrane at pH 3.9, transmembrane pressure 241kPa, crossflow velocity 2.3m·s^{-1} , and the electric voltage 50V(DC) giving an electric strength of 167V·cm^{-1}. The content of titanium dioxide in suspension was 0.33%(v/v), and the particle mean size was 0.5μm (about 1 order smaller than the particle mean size of this study). No gas releasing channel was described. Though their electric strength and the transmembrane pressure were no more than one order higher than this study, the permeate flux gain was more than two orders higher. That the smaller particles are more sensitive to the electric field may be another reason for this.

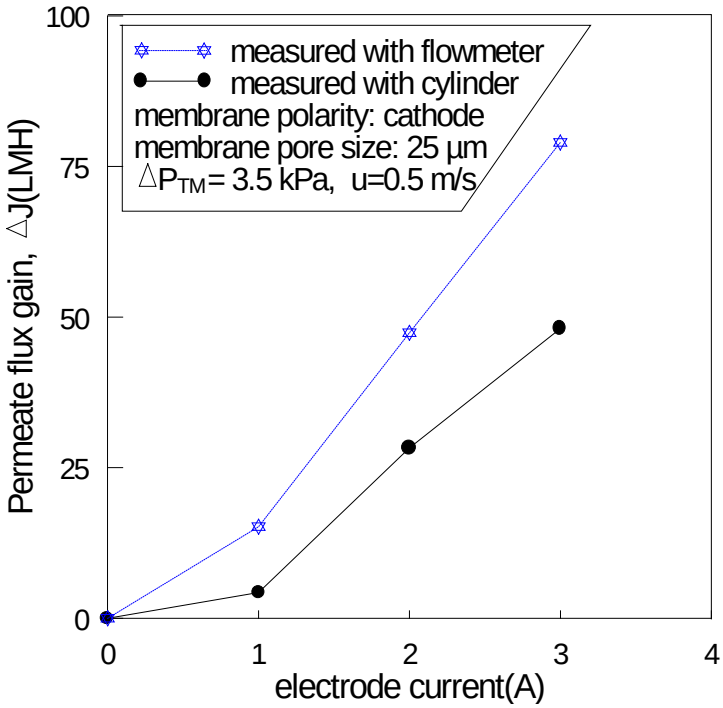

Figure 4-18. Dependence of the flux gain **ΔJ** on the cathode current
Measured with flowmeter and measuring cylinder respectively,
in which the gas-releasing channel was closed

To distinguish the bubble influence from the true permeate flux, a measuring cylinder and stop watch were used to measure the flow rate and compared with the result of

the flowmeter. The results are shown in Figure 4-18. The permeate flux gain measured with the flowmeter was 50% higher than the actual value.

The permeate flux gain was measured at a low transmembrane pressure of 3.5kPa where the flux (possibly lower than the critical flux) could be maintained stable for quite a long time without obvious decline. Note the gas-releasing channel was closed in order to examine the influence of gas bubbles. However in the other EMF experiments of the study, the gas-releasing channel was fully opened, so the permeate fluxes mentioned in other parts of this paper were the "true" fluxes. After the electric field was applied, the permeate flux increased and reached a maximal value after about 5~10 minutes. The higher the voltage applied, the stronger the membrane current and the larger the flux gain obtained. After the flux came to its maximal value, it decreased again no matter whether the electric field persisted or not. Thus the variation of the flux produced a peak value. This flux change was the so-called permeate flux gain, and is shown as the ordinate in Figure 4-18.

According to *Faraday's* electrolysis law, it can be estimated that every one ampere of cathode-current will produce about 7.5ml·min^{-1} cathodic gas at 20°C and 1atm, corresponding to about 23(LMH) additional permeate flux in this experimental system. More details will be given in section 6.2.

The third phenomenon noticed after applying the electric field was that the permeate pH increased (to pH>11), and the clear permeate turned slight milky (the absorbance rose from 0 to 0.176 at 360nm). These effects were also the result of electrochemical reactions and are shown in Figure 4-16 and figure 4-17. The reactions occuring on membrane will be further discussed in Chapter 5. Figure 4-19 shows another pulsatile application of the electric field in which the average steady state permeate flux was improved about 30%. Although the cathode reaction on the membrane will result in permeate alkalizing and lead to calcium salt deposition, the production of gas bubbles, on the other hand, can potentially blow the deposit cake off the membrane surface. This effect can cooperate with the electric field repulsion of the particles to

reduce fouling and explains why the permeate flux increases when electric field is applied.

Compared with the electro-microfiltration of titania (titanium dioxide) performed by Wakeman et al.(1995), some negative results caused by electrolysis, such as cathode deposit and increased membrane fouling were found with both Alamin and calcite filtration in this study. Titanium dioxide, however, has much lower solubility in water which almost does not change across a wide range of pH. This property makes it more suitable for charged membrane filtration.

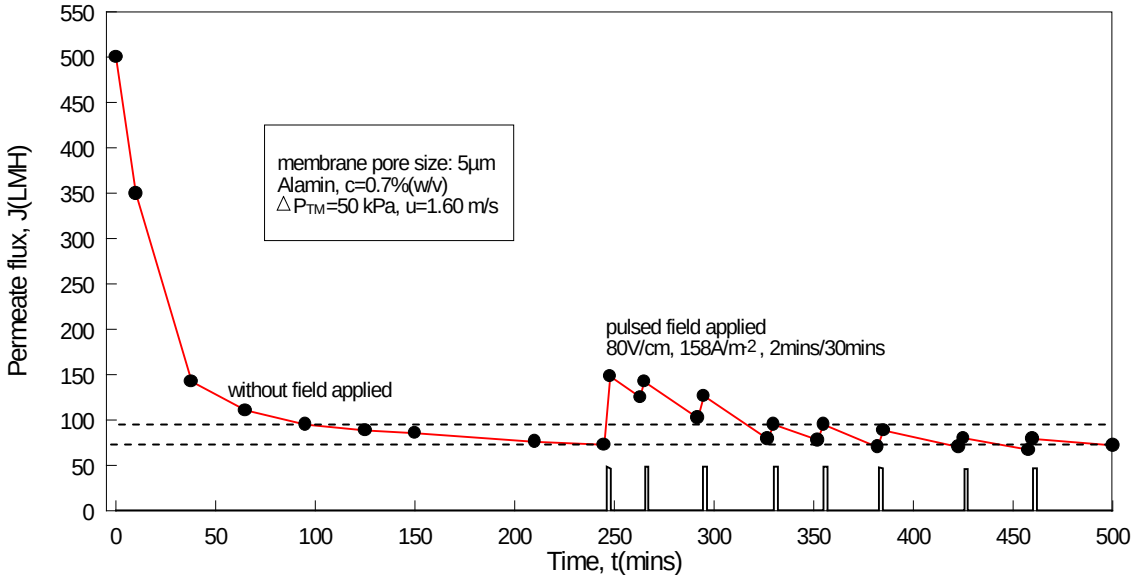

Figure 4-19. Manually controlled pulsatile application of electric field after the permeate flux reach to the steady state

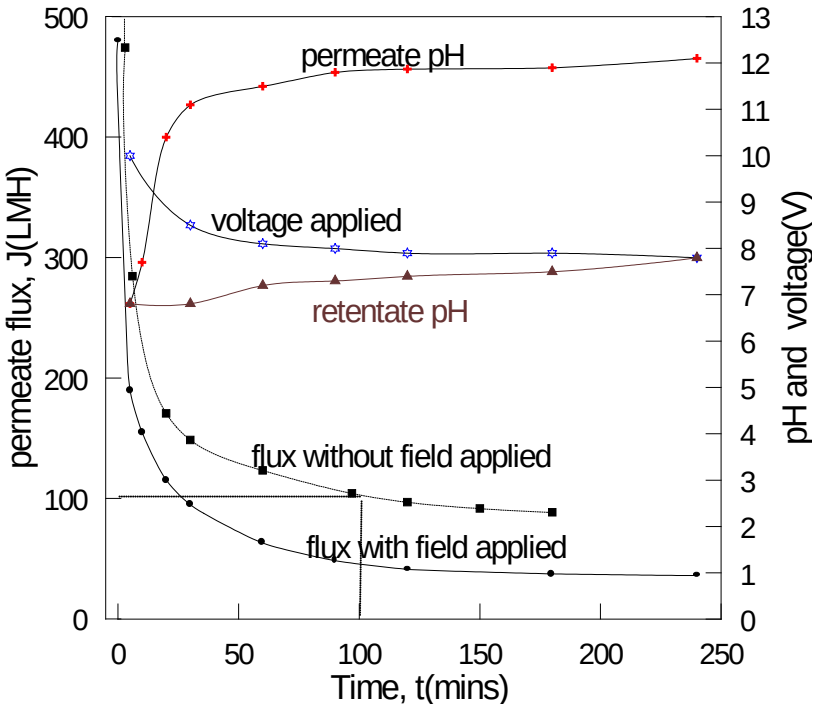

Figure 4-20. Continuous application of electric field at 1A (52.6A·m^2 current density), 10~7.8V (36~28 electric field strength), Alamin content c=0.7%(w/v), transmembrane pressure ΔP_{TM}=50kPa, cross flow velocity u=2.28m·s^{-1} . membrane polarity: cathode.

Data for the continuous application of an electric field is shown in Figure 4-20, where the membrane current was fixed on 1A and the corresponding current density was 52.6A·m^{-2} . The voltage that maintained this current was 10V(DC) at the beginning, and gradually fell to 7.8V(DC) at the end of this run. Because of the electrolysis, the permeate pH increased rapidly, and the calcium salt precipitated as a result. It was found that continuous application of an electric field for long times aggravated the membrane fouling, i.e., the permeate flux declined more rapidly than that without an electric field being applied. A comparison of the appropriate runs is shown in Figure 4-20 by the dashed line. The so-called “solvent electrolysis” effect (Wakeman et al. 1995) was not found in this study when membrane was negatively charged. However, this effect does exist when the membrane works as an anode (next section).

4.5.3. EMF with A Positively Charged Membrane

The experiments shown so far were all with the membrane negatively charged or uncharged. Results for positively charged membrane microfiltration will be presented and discussed in this section (Figure 4-21 and Figure 4-22). In contrast to the negatively charged operation, the permeate pH was reached to a low value in this set of runs (e.g., pH<3.5), and the permeate flux at 150 minutes was 65% higher and about 300% higher than the uncharged and negatively charged operation, respectively.

Obviously, the consumption of hydroxyl ions on the anode (membrane) caused by electrolysis was the reason for permeate acidification. This would result in dissolving of calcium salts and reduced membrane fouling, despite the electric attraction of the (negatively charged) particles to the membrane. The overall effect was that the permeate flux increased compared to filtration without an electric field being applied.

The difference between the runs shown in Figure 4-21 and Figure 4-22 was that in Figure 4-22 the jacket of the membrane cell was empty at the beginning, but in Figure 4-21, the jacket of membrane cell was filled with residual RO water. This remained from rinsing after cleaning. In the latter case the permeate had to mix with this water in the jacket and this in turn retarded the pH variation. According to Figure 4-22, the permeate pH exhibited a minimum at the initial time.

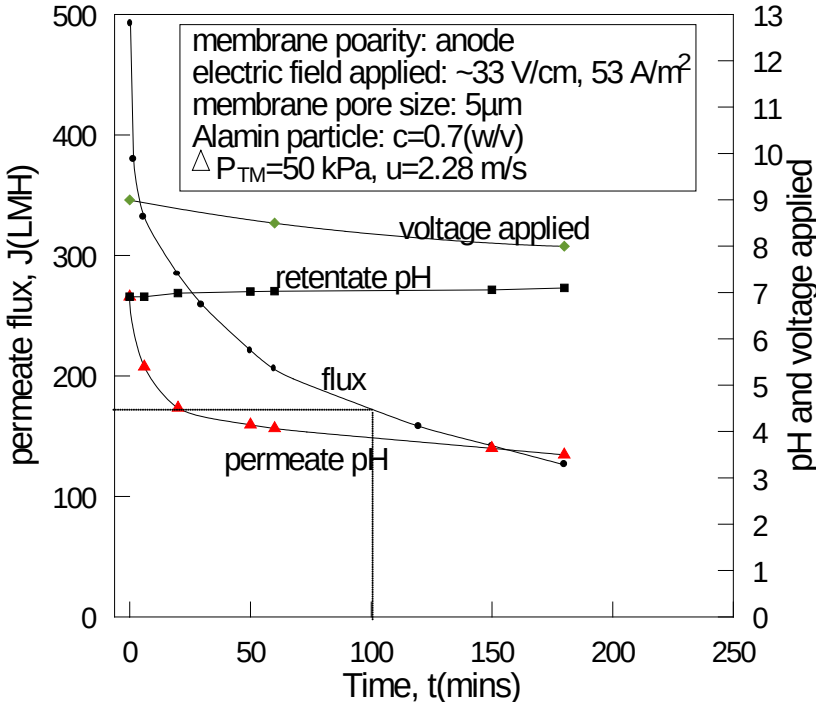

Figure 4-21. Continuous application of electric field where the membrane was positively Charged and the jacket was filled with RO water at the beginning

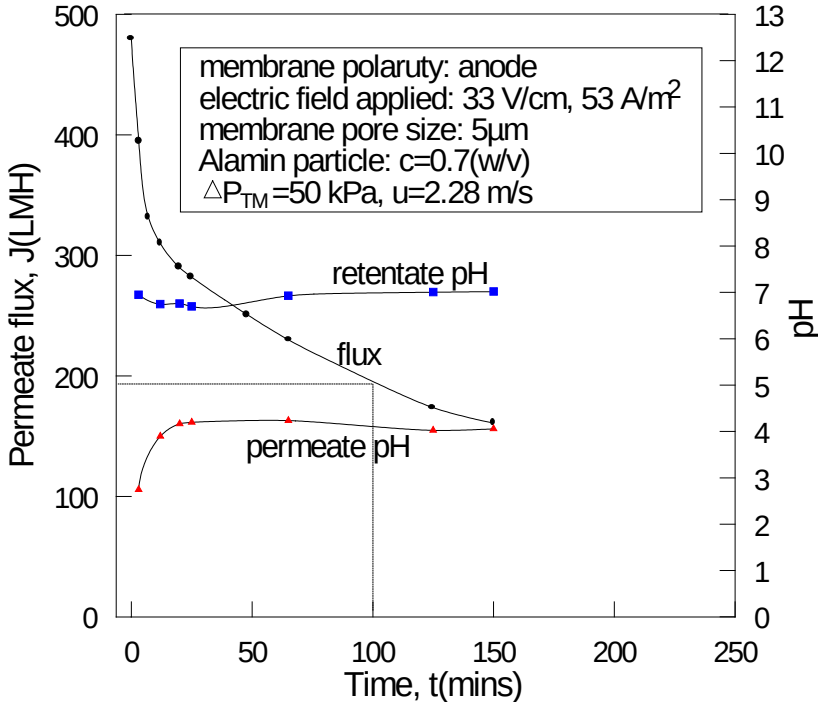

Figure 4-22. Continuous application of electric field where the membrane was Positively charged and the jacket was empty at the beginning.

Though the permeate flux can be apparently improved by using a positively charged membrane, the side-effects, such as the anode corrosion on the stainless steel membrane and the change of physico-chemical properties of the filtrate caused by electrochemical reaction cannot be ignored. For this reason the duration of operating time was 180 minutes only, while for the negative charged operation it was 240 minutes. The aspect of electrochemistry which results in anode corrosion will be further discussed in Chapter 5.

Another set of runs designed to investigate the behavior of calcite was carried out on the 25μm membrane. Some results are shown in Figure 4-23 and Figure 4-24. The permeate flux dropped rapidly in the first 20 minutes and came to a stable, slowly declining phase about 50 minutes later. Because the permeate flux was so high in the initial period, the pressure drop due to high flow velocity from the jacket (where the pressure gauge was mounted) to the outlet of the loop back tube could not be ignored. At the beginning of filtration, the permeate pressure P_{per} could be as high as 25~30kPa. This was a remarkable difference to the behavior of 5μm membrane, in which the permeate pressure was always at low level and never higher than 5kPa even in the initial period.

The results from this set of runs provide further evidence that the electro-microfiltration of different calcium salts have some basic characteristics which can be explained by the electrolytic effect and the pH-sensitive solubility of calcium salts.

Other characteristics of permeate flux decline on the charged and uncharged membrane were very similar to the runs with Alamin on the 5μm membrane (Figure 4-24).

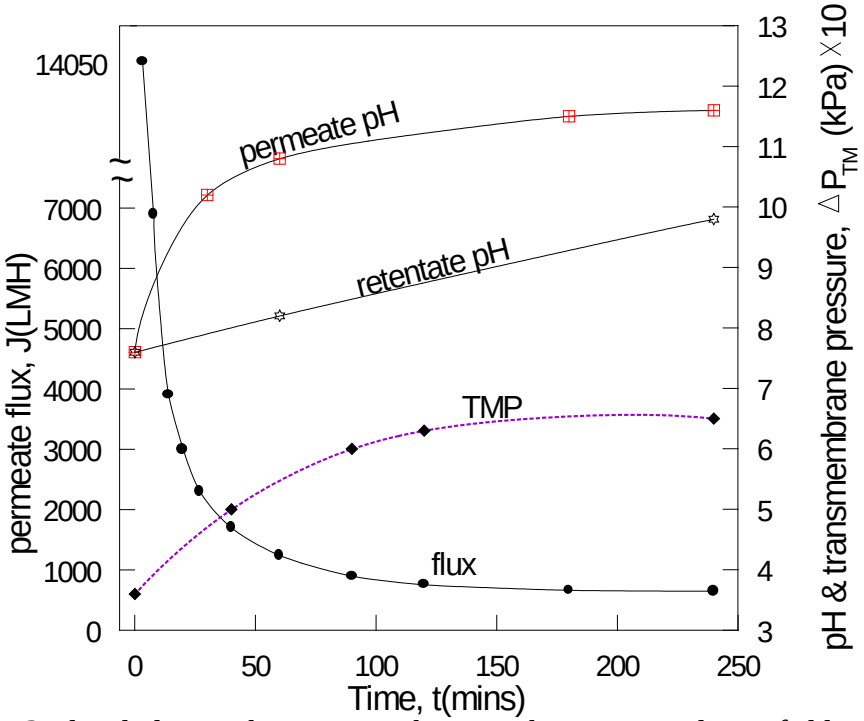

Figure 4-23. Flux decline on the 25μm membrane with continuous electric field ap membrane polarity: cathode, field strength:158V/cm, current density: 80A/m^2, $\triangle P_{TM}$ =36~67kPa, calcit content c=0.7%(w/v), u=2.43m/s

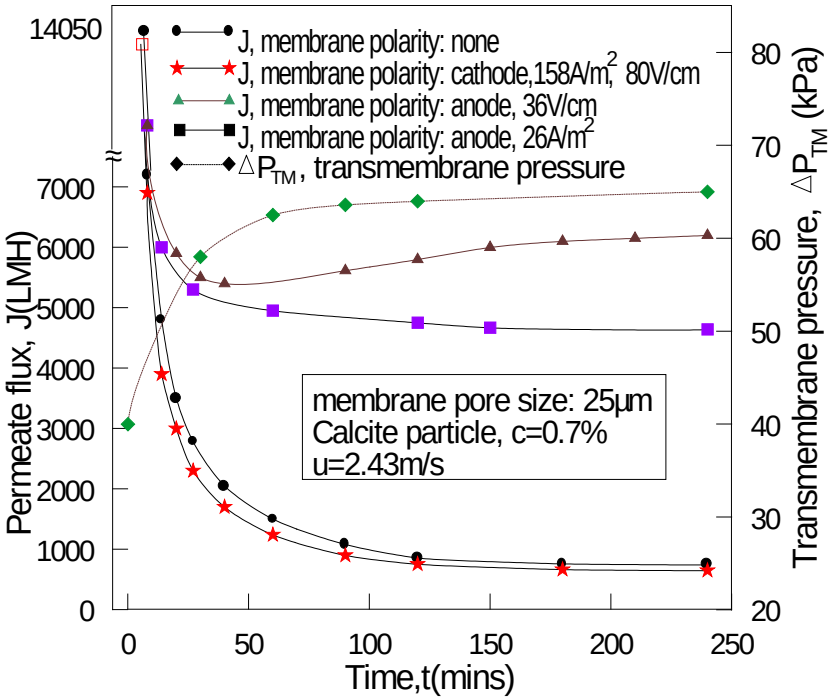

Figure 4-24. Comparison of flux decline on the 25μm membrane at different electric field strengths

4.6. Constant Flux and Critical Flux

In general, the constant-flux filtration was obtained with moderately increasing transmembrane pressure. This approach is shown to have some advantages over normal constant-pressure filtration because it clearly provides the possibility of avoiding over fouling and so reduces the severity of fouling.

The filtration results in Figure 4-25, 4-26 and 4-27 at low TMP and low flux indicate a relatively small degree of fouling. In these experiments a combination of moderate pump speed and low valve opening on the permeate side was employed, i.e., the permeate valve X_P was almost closed at the beginning. Another key point is that the jacket on the permeate side must be filled up with water. The presence of water in the jacket can prevent too high an initial flux and consequent fouling. Among the several elements responsible for the constant-flux operation, a low initial flux is definitely essential.

The particle size and size distribution also affect the available value of constant-flux. For example, the calcite particle has a mean size of 8.15μm, and standard deviation of 6.46μm; whilst for Alamin the average dimensions are 4.63μm (See 3.4.2). As the calcite particle was larger than the Alamin in this study, constant-flux operation for the calcite particle on the 5μm membrane was easier to achieve than that for the Alamin.

The critical-flux hypothesis is that on start-up there exists a flux below which a decline of flux with time does not occur. According to Field et al (1995)., “the critical flux should not be confused with the limiting flux found in ultrafiltration which occurs independently of fouling and is due to concentration polarization.” “ The critical flux would seem to correspond to the flux with just avoids cake deposit.”

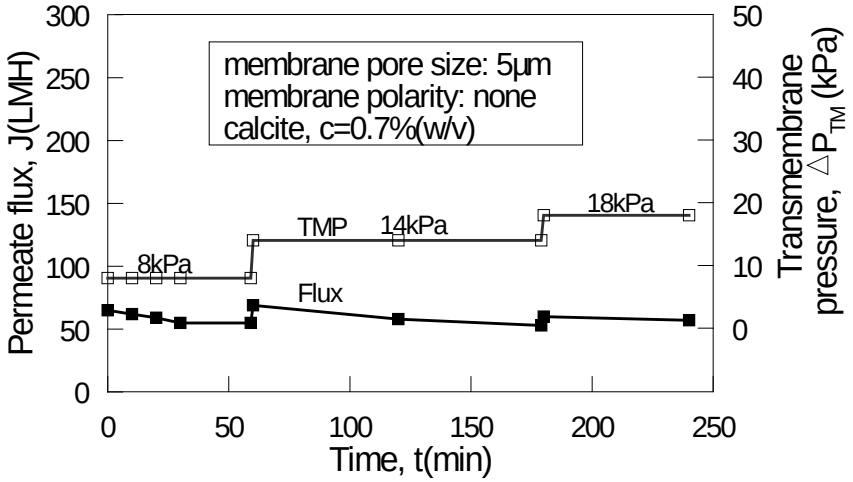

Figure 4-25. Moderate increase of transmembrane pressure to keep a constant flux

Some results are shown in Figure 4-26 and Figure 4-27 in which the rates of flux decline were very low, and the system perhaps approached the so called critical flux. The membrane surface was also found to be visibly free of cake. But the operation without flux decline on the 25µm membrane was not achieved in this work. This may be attributed to the relative large pore size of the membrane and the fouling mechanism of pore plugging. The scouring effect of the cross flow thus could not provided sufficient lift force to remove the pore-plugging particle to lessen the membrane fouling.

These results also indicated that a pore size smaller than the particles is one of the elements for achieving critical flux operation. For instance, Howell and Field et al [40,41,42,26], who proposed the concept of critical flux, carried out the critical flux experiments on a 0.2µm pore size Ceramesh membrane at 10-20kPa TMP. The treated particles were yeast and calcium carbonate, both of which were larger than the membrane pore size. Another element to necessary achieve critical flux operation was a low TMP which was normally below 20kPa.

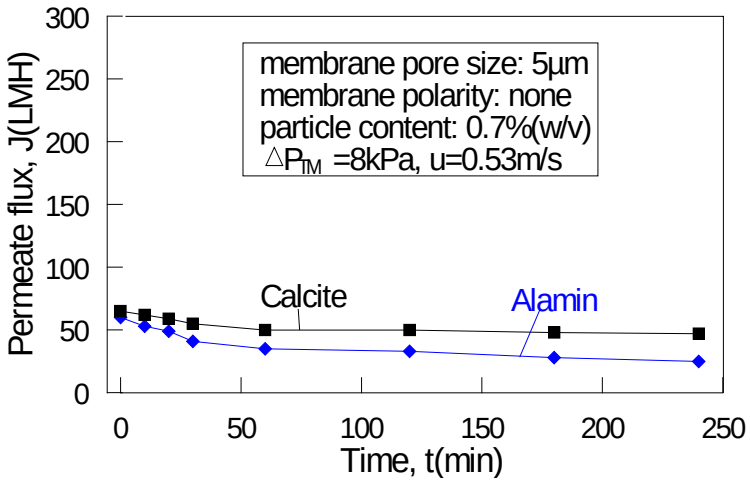

Figure 4-26. Comparison of flux decline of Alamin and calcite particle(I) on the 5μm membrane

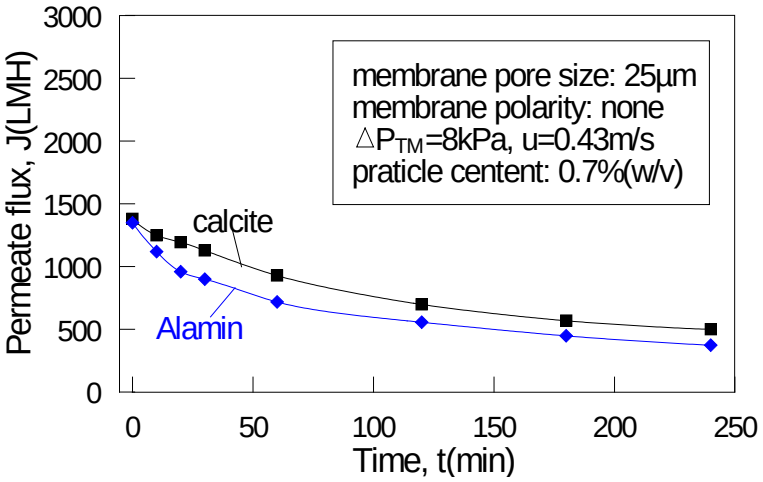

Figure 4-27. Comparison of flux decline of Alamin and calcite particle(II) on the 25μm membrane

5. Effects of Electric Field

5.1 Electrophoretic Migration of Particles

A pair of stainless steel wires, ϕ0.3mm in diameter, were anchored 1.1mm apart with epoxy resin on a glass slide. These served as electrodes when charged by the DC power supply (Figure 5-1).

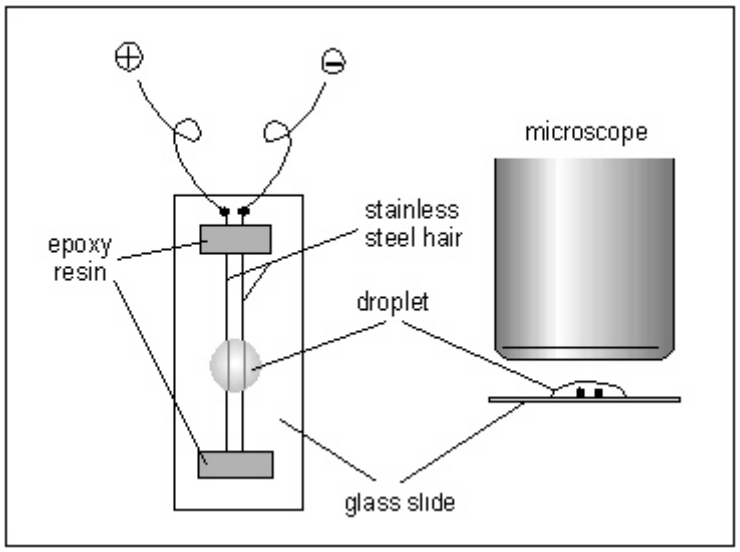

Figure 5-1. Small electrode arrangement for examining electrophoretic movement of particles

Droplets of particle suspension were put on to the slide surface between the electrodes, and the particle behaviour under an applied field was examined with a microscope. Since the Zeta potential of the Alamin particles is negatively charged in the neutral range of pH, so they are attracted by the anode, or repulsed by the cathode when the electric field was applied. However it was observed that only those particles roughly under 1μm had visible electrophoretic mobility under a reasonable electric field strength (e.g. 36V/cm); larger particles deposited onto the slide floor and did not show any electrophoretic mobility. Under this condition, in the vicinity of the anode, the electrophoretic speed of the particles around 1μm in size were ranged from 38.17 to 49.85 μm/s in five replicates, giving an average value of ~43μm/s. Some measured results were shown in Table 5-1.

Table 5-1. Electrophoretic speed of Alamin particle

Concentration (w/v) & pH	Electric field strength(V/cm)	Electrophoretic Distance (μm)	Particle diameter (μm)	Time elapsed (s)	electrophoretic speed (μm/s)	average speed (μm/s)
0.7%, 6.96	36	500	~1	11.52,13.10, 11.73, 10.03, 12.23	38.17~ 49.85	42.65

The maximal electrophoretic speed measured was 50 μm/s under the electric field strength of 36V/cm which was a typical value applied on the membrane in this research. Since the particle electrophoresis is a uniform movement, according to *Newton's* second law, the vector sum of forces acting on the particle is zero:

$$\vec{\mathbf{F}}_{\mathbf{E}} + \vec{\mathbf{F}}_{\mathbf{D}} = 0 \qquad (5\text{-}1)$$

where the $\vec{\mathbf{F}}_{\mathbf{E}}$ is the electric field force and $\vec{\mathbf{F}}_{\mathbf{D}}$ the viscous drag force acting on the particle. The value of the electric field force can be expressed as the product of charge and field strength.

$$\mathbf{F}_{\mathbf{E}} = \mathbf{q} \cdot \mathbf{E} \qquad (5\text{-}2)$$

where **q** is the particle charge and **E** the electric field strength.

There are two flow conditions for which the expression of the viscous drag force can be derived. When the *Reynolds* number with respect to the particle is less than 1, *Stokes' Law* applies[24]:

$$\mathbf{F}_{\mathbf{D}} = \Phi \mathbf{r} \mathbf{v} \mu \quad (\mathrm{Re} < 1) \qquad (5\text{-}3)$$

where **r** is the radius of the particle, **v** the relative velocity of fluid and particle, μ the fluid viscosity, and ϕ the shape coefficient of particle. For a spherical object, $\phi = 6\pi$, so

$$\mathbf{F}_{\mathbf{D}} = 6\pi \cdot \mathbf{r} \mathbf{v} \mu, \quad (\mathrm{Re} < 1) \qquad (5\text{-}4)$$

When the *Reynolds* number with respect to the particle is ≥ 1, the drag force F_D will approximately be proportional to u^2 , and can be expressed as

$$\mathbf{F_D} = \mathbf{C_D A_p} \cdot \frac{\rho_w \mathbf{v}^2}{2}, \quad (\mathrm{Re} \geq 1) \tag{5-5}$$

where $\mathbf{A_p}=\pi \cdot R^2$, the cross-sectional area of the spherical particle, $\frac{\rho_w \cdot \mathbf{v}^2}{2}$ is the kinetic energy per unit volume of fluid with velocity **v**, and $\mathbf{C}_D$ is the drag coefficient (which must be obtained from measurement). Experiments for $\mathbf{C}_D$ showed that $\mathbf{C}_D$ is nearly constant[24]; it varied among 0.3 and 3.0 as the *Reynolds* number (**Re)** varies from 10 to 10^6 .

As we have seen the relative velocity between the 1μm particle and the liquid, i.e., the electrophoretic speed, is about 50μm/s under the electric field strength of 36V/cm. The *Reynolds* number for this particle is

$$\begin{aligned} \mathrm{Re} &= \frac{\mathbf{v} \cdot \mathbf{r} \cdot \rho_w}{\mu} \\ &= \frac{(50 \times 10^{-6} \mathbf{m} \cdot \mathbf{s}^{-1}) \times (0.5 \times 10^{-6} \mathbf{m}) \times (1000 \mathbf{kg} \cdot \mathbf{m}^{-3})}{100.42 (\mathbf{Pa} \cdot \mathbf{s})} \\ &= 2.5 \times 10^{-5} << 1 \end{aligned} \tag{5-6}$$

The viscous drag force to the particle thus has the value of

$$\begin{aligned} \mathbf{F_D} &= 6\pi \cdot \mathbf{r} \cdot \mathbf{v} \cdot \mu \\ &= 6 \times 3.1416 \times (0.5 \times 10^{-6} \mathbf{m}) \times (50 \times 10^{-6} \mathbf{m} \cdot \mathbf{s}^{-1}) \times (100.42 \mathbf{Pa} \cdot \mathbf{s}) \\ &= 4.73 \times 10^{-13} \mathbf{N} \end{aligned} \tag{5-7}$$

From Eq. (5-1), the electric field force will be:

$$\mathbf{F_E} = -\mathbf{F_D} = -4.73 \times 10^{-13} \mathbf{N} \tag{5-8}$$

Where the negative sign means the electric field force has the same value as the viscous drag force, but in the opposite direction. Consequently, the charge of the particle can be estimated as:

$$\mathbf{q} = \frac{\mathbf{F_E}}{\mathbf{E}} = \frac{-4.73\times10^{-13}\,\mathbf{N}}{36\times10^{2}\,\mathbf{V}\cdot\mathbf{m}^{-1}} = -1.314\times10^{-16}\,\mathbf{C} \tag{5-9}$$

The weight of the Alamin particle, for comparison, can be calculated as:

$$\mathbf{W} = \mathbf{g}\cdot\rho_{\mathbf{p}}\cdot\frac{\pi\cdot\mathbf{d}_{\mathbf{p}}^{3}}{6} = 9.81\mathbf{m}\cdot\mathbf{s}^{-2}\times2.274\times10^{3}\mathbf{kg}\cdot\mathbf{m}^{-3}\times\frac{3.1416\times(1\times10^{-6}\mathbf{m})^{3}}{6} = 1.17\times10^{-14}\,\mathbf{N} \tag{5-10}$$

giving:

$$\frac{|\mathbf{F_E}|}{\mathbf{W}} = \frac{4.73\times10^{-13}\,\mathbf{N}}{1.17\times10^{-14}\,\mathbf{N}} = 40.43 \tag{5-11}$$

Thus the electric field force is about 40 times of the weight of those Alamin particles around 1μm in size

To estimate the electric field force for a mean size Alamin particle (d'=4.63μm), we can assume that the charge density on the particle surface is approximately the same, so the total charge **q'** on an individual mean size particle is proportional to its surface area A'.

$$\mathbf{q'} = \mathbf{A'}\cdot\frac{\mathbf{q}}{\mathbf{A}} = \frac{4}{3}\pi\cdot\mathbf{d'}^{2}\times\frac{\mathbf{q}}{\frac{4}{3}\pi\cdot\mathbf{d}^{2}} = \frac{\mathbf{q}\cdot\mathbf{d'}^{2}}{\mathbf{d}^{2}} \tag{5-12}$$

For a mean particle size of 4.63μm (see section 3.4.2),

$$\mathbf{F'} = \mathbf{q'}\,\mathbf{E} = \frac{\mathbf{q}\cdot\mathbf{d'}^{2}}{\mathbf{d}^{2}}\cdot\mathbf{E} = \frac{-1.314\times10^{-16}\,\mathbf{C}\times(4.63\times10^{-6}\,\mathbf{m})^{2}\times(36\times10^{2}\,\mathbf{V}\cdot\mathbf{m}^{-1})}{(1\times10^{-6}\,\mathbf{m})^{2}} = -1.014\times10^{-11}\,\mathbf{N} \tag{5-13}$$

and

$$\frac{|\mathbf{F'}|}{\mathbf{W'}} = \frac{1.014\times10^{-11}\,\mathbf{N}}{(9.81\,\mathbf{m}\cdot\mathbf{s}^{-2})\times(2.274\times10^{3}\,\mathbf{kg}\cdot\mathbf{m}^{-3})\times\frac{1}{6}\times3.1416\times(4.63\times10^{-6}\,\mathbf{m})^{3}} = 8.75 \quad (5\text{-}14)$$

The electric field force in this case is about 9 times the particle weight.

5.2 Analysis of Forces Acting on A Particle Depositing on The Membrane

As the cross flow velocity was 2.28m/s, the average residential time of the particle in the module(~0.17 second) was much shorter than the time a particle migrating across the laminar sub-layer(~2 second). The electric field force is therefore only effective to those particles in the closest vicinity of the membrane (<10μm). There are four main states for an individual particle passing through the membrane module. These are shown in Figure 5-2:

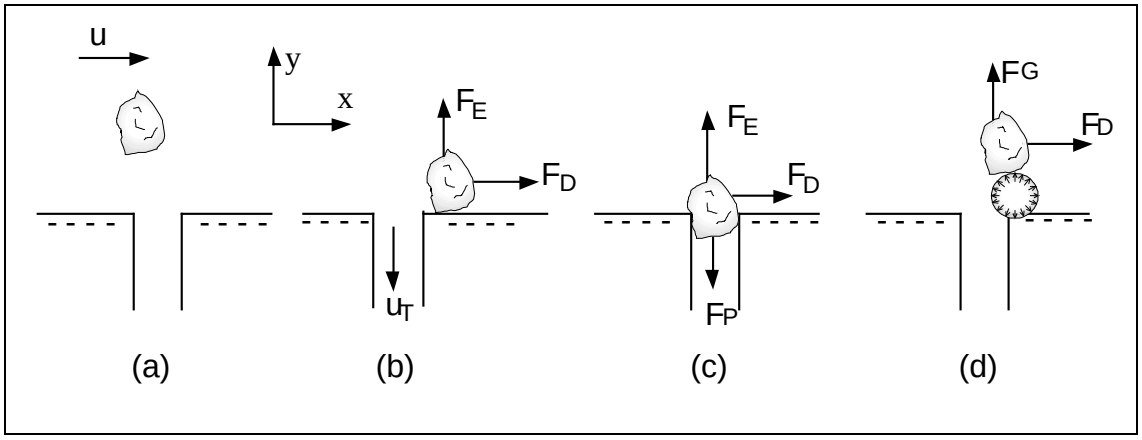

Figure 5-2. Four states of the particle in the membrane unit

(a)The particle is in suspension in the fluid;

(b)The particle has deposited on the membrane surface, but neither blocks the entry nor plugs the pore.

(c)The particle has entered into the pore tunnel and remains there, either because of adsorption or physical entrapment (e.g. due to tortuosity of pore, or bridging).

(d)The particle is just being rejected by a newly formed cathode gas bubble.

Most of particles in the module, from inlet to outlet, will probably always be in the suspended state. However, our concern is the combination of forces or events that lead to deposition, or removal of deposited particles.

In Figure 5-2, **u** is the mean velocity of the feed stream; $\mathbf{F}_E$ is the repulsive force of the electric field acting on the particle which is supposed to be negatively charged; $\mathbf{F}_D$ is the viscous drag force of fluid acting on the deposited particle**.** $\mathbf{F}_P$ is the force the transmembrane pressure exerts on the particle blocking in the pore tunnel, and $\mathbf{F}_G$ the rejective force acting on the particle due to the gas bubble formation.

5.2.1 The Viscous Drag Force F_D

When a particle deposits onto the membrane, i.e. in state (b), it will be subject to a drag force of fluid because of the relative velocity between the fluid and particle. The equivalent diameter of a mean size particle is about 4.63μm according to microscope measurement (see 3.4.2). This is much smaller than the thickness of the laminar sub-layer, which has a value of 81μm under the crossflow velocity of **u**=2.28 m/s (see 4.3.6). Because the laminar sub-layer is very thin, the velocity distribution within it can be considered linear and the value of the velocity gradient (**u**') is estimated as(also see 4.3.5 & 4.3.7):

$$\mathbf{u}' = \frac{\partial \mathbf{u}}{\partial \mathbf{y}} = \frac{\mathbf{u_b}}{\delta_\mathbf{b}} = \frac{1.86\mathbf{m}\cdot\mathbf{s}^{-1}}{81\times10^{-6}\mathbf{m}} = 2.30\times10^{4}\mathbf{s}^{-1} \qquad (5\text{-}15)$$

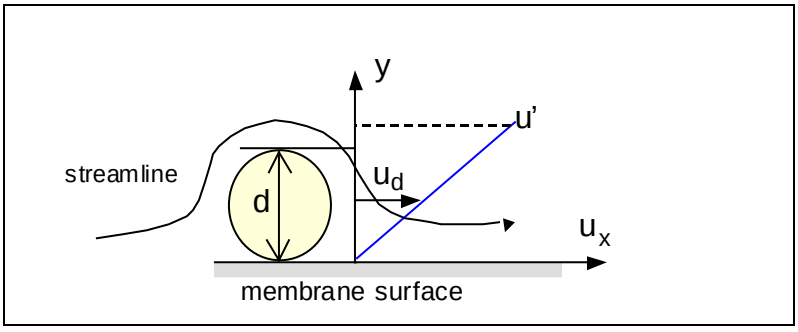

Figure 5-3. The relative velocity of deposited particle and fluid in the laminar-sub layer

At the height of the particle center ($\mathbf{y} = \frac{1}{2}\mathbf{d} = \frac{4.63}{2}\mu\mathbf{m} = 2.32\mu\mathbf{m}$) where the flow velocity is considered to be the average relative velocity to the particle, which can be calculated as:

$$\begin{aligned}\mathbf{u_d} &= \left(\frac{\partial u}{\partial y}\right)\cdot \mathbf{y} = \frac{\mathbf{u_b}}{\delta_b}\cdot\frac{\mathbf{d}}{2} \\ &= 2.30\times 10^{4}\,\mathbf{s}^{-1}\times\frac{4.63\times 10^{-6}\,\mathbf{m}}{2} \\ &= 5.32\times 10^{-2}\,\mathbf{m}\cdot\mathbf{s}^{-1} \quad \text{i.e. about 5cm per second}\end{aligned} \tag{5-16}$$

The *Reynolds* number with respect to the particle is:

$$\begin{aligned}\mathrm{Re} &= \frac{\mathbf{u_d}\,\mathbf{r}\,\rho_w}{\mu} = \frac{(5.32\times 10^{-2}\,\mathbf{m}\cdot\mathbf{s}^{-1})\times(4.63\times 10^{-6}\,\mathbf{m})\times(998.2\,\mathbf{kg}\cdot\mathbf{m}^{-3})}{2\times 100.42\times 10^{-5}\,\mathbf{Pa}\cdot\mathbf{s}} \\ &= 0.12 < 1\end{aligned} \tag{5-17}$$

The *Reynolds* number is less than 1 imply that the *Stokes'* Law for the drag force is again applicable:

$$\begin{aligned}\mathbf{F_D} &= 6\pi\cdot\mathbf{r}\cdot\mathbf{u_d}\cdot\mu \\ &= 6\times 3.1416\times(\tfrac{1}{2}\times 4.63\times 10^{-6}\,\mathbf{m})\times(5.32\times 10^{-2}\,\mathbf{m}\cdot\mathbf{s}^{-1})\times(100.42\times 10^{-5}\,\mathbf{Pa}\cdot\mathbf{s}) \\ &= 2.33\times 10^{-9}\,\mathbf{N}\end{aligned} \tag{5-18}$$

Equation (5-18) indicates that the viscous drag force is proportional to the particle size within the laminar-sub layer. If the particle size is larger than the laminar-sub layer, it will experience a much stronger drag force because the tangential flow velocity non-linearly increases rapidly in the outer edge of laminar-sub layer. On the other hand, the roughness of membrane surface will act to retain some particles to form a fine cake. This explains the fact that the particles in the fouling cake are always found smaller than those in the suspension which was observed by other researchers. The viscous drag force should be distinguished with the shear stress discussed in 4.3.8. The former is a force acting on a deposited particle and the latter is on the membrane surface which is supposed to be smooth and clean. When a spot on the membrane surface is occupied by a deposited particle, the shear stress at this tiny area will transform to the viscous drag force acting on the particle.

5.2.2 The Electric Field Force F_E

The electric field force $\mathbf{F}_E$ is the product of field strength **E** and particle charge **q**, and can be estimated through the particle electrophoresis test. For a mean size Alamin particle the corresponding electric field force is $\mathbf{F_E} = 1.01\times10^{-11}$ **N** (Eq. (5-13) in section 5.1). The ratio of drag and repulsion will be

$$\frac{\mathbf{F_D}}{\mathbf{F_E}} = \frac{2.33\times10^{-9}}{1.01\times10^{-11}} \approx 230 \qquad (5\text{-}19)$$

The weight of a mean size Alamin particle is:

$$\begin{aligned}\mathbf{W} &= \mathbf{g}\rho_w \cdot \frac{\pi\cdot\mathbf{d}'^3}{6} \\ &= 9.81\mathbf{m}\cdot\mathbf{s}^2 \times 2.274\times10^3\mathbf{kg}\cdot\mathbf{m}^{-3} \times \frac{3.1416\times(4.63\times10^{-6}\mathbf{m})^3}{6} \\ &= 1.16\times10^{-12}\mathbf{N}\end{aligned} \qquad (5\text{-}20)$$

so that

$$\frac{\mathbf{F_D}}{\mathbf{W}} = \frac{2.33\times10^{-9}\mathbf{N}}{1.16\times10^{-12}\mathbf{N}} \approx 2000 \qquad (5\text{-}21)$$

Therefore, the viscous drag force F_D is about 230 times the electric force F_E, and about 2000 times the particle weight. In the range of microfiltration, the particle size above 1 μm to 100μm, the fluid drag force is thus much stronger than the electric force.

5.2.3 The Driving Force F_P Associated with The Transmembrane Pressure

When the particle enters or blocks the membrane pore tunnel, the particle will also be subject to a driving force which tends to force the particle pass through the membrane barrier, i.e. state (c) in Figure 5-2. This driving force is proportional to the cross-sectional area of the particle and the transmembrane pressure, and can be expressed as

$$\mathbf{F_P} = \frac{\pi \cdot \mathbf{d}^2}{4} \cdot \Delta \mathbf{P_{TM}}$$
$$= \frac{3.1416 \times (4.63 \times 10^{-6}\mathbf{m})^2}{4} \times (50 \times 10^3 \mathbf{N} \cdot \mathbf{m}^{-2})$$
$$= 3.37 \times 10^{-6}\mathbf{N} \qquad (5\text{-}23)$$

To compare with the drag force, we have

$$\frac{\mathbf{F_P}}{\mathbf{F_D}} = \frac{3.37 \times 10^{-6}\mathbf{N}}{2.33 \times 10^{-9}\mathbf{N}} \approx 1450 \qquad (5\text{-}24)$$

i.e. $\mathbf{F_P}$ is ~1500 times larger than the drag force, in which the transmembrane pressure ($\Delta \mathbf{P_{TM}}$) is 50 kPa.

For ordinary microfiltration it is assumed that the flow regime inside the pore tunnel is laminar flow. The flow friction is considered to be the reason for the pressure drop through the pore tunnel and the pressure drop can be given by *Poiseuille* equation:

$$\Delta \mathbf{P} = \frac{32\mu \ell' \mathbf{u_T}}{\mathbf{d_T^2}} \qquad (5\text{-}25)$$

where $\Delta \mathbf{P}$ is the pressure loss from retentate side to permeate side through the pore tunnel (so it equals the transmembrane pressure **TMP**), $\mathbf{u}_T$ is the average flow velocity through the pore tunnel, $\boldsymbol{\ell}$ the tunnel length which is always greater than the thickness of membrane because of the tortuosity of the tunnel, $\mathbf{d_T}$ the equivalent diameter of pore tunnel, and μ the viscosity of water. The transmembrane pressure used in this research is mainly 30 ~ 50 kPa, and the nominal pore size is 5μm in diameter. Suppose the tunnel length $\boldsymbol{\ell}$ is two times of the membrane thickness, which is about 0.5mm, i.e. $\boldsymbol{\ell}$=2×0.5=1mm. Substitute these into the *Poiseuille* Equation, so that we can estimate the range of flow velocity in the membrane pore tunnel:

$$\mathbf{u_T} = \frac{\mathbf{d_T^2} \cdot \Delta \mathbf{P}}{32\mu \cdot \ell} = \frac{(5 \times 10^{-6}\mathbf{m})^2 \times (30 \sim 50) \times 10^3 \mathbf{Pa}}{32 \times (100.42 \times 10^{-5}\mathbf{Pa} \cdot \mathbf{s}) \times (1 \times 10^{-3}\mathbf{m})}$$
$$= 0.023 \sim 0.039 \mathbf{m} \cdot \mathbf{s}^{-1} \qquad (3\text{-}26)$$

The corresponding *Reynolds* number is:

$$\mathrm{Re} = \frac{\mathbf{u_T d_T}\rho_w}{\mu} = \frac{[(0.023 \sim 0.039)\mathbf{m \cdot s^{-1}}] \times (5 \times 10^{-6}\mathbf{m}) \times (998.2\mathbf{kg \cdot m^{-3}})}{100.42 \times 10^{-5}\mathbf{Pa \cdot s}}$$
$$= 0.114 \sim 0.194 < 1 \qquad (5\text{-}27)$$

The viscous drag force ($\mathbf{F_{DT}}$) on a mean size particle inside the pore tunnel, therefore, can be estimated by *Stokes* equation:

$$\mathbf{F_{DT}} = 6\pi \cdot \mathbf{d_T} \cdot \mathbf{u_T} \cdot \mu$$
$$= 6 \times 3.1416 \times (\tfrac{1}{2} \times 5 \times 10^{-6}\mathbf{m}) \times (0.023 \sim 0.039\mathbf{m \cdot s^{-1}}) \times (100.42 \times 10^{-5}\mathbf{Pa \cdot s})$$
$$= (9.7 \sim 16.6) \times 10^{-10}\mathbf{N} \qquad (5-28)$$

$\mathbf{F_{DT}}$ is much less than $\mathbf{F_P}$ ($\mathbf{F_P}$ /$\mathbf{F_{DT}}$ =2.03×10^3~3.47×10^3) indicating that inside the pore tunnel the pressure difference across the membrane is the major force that drives the particle overcross the membrane barrier.

5.2.4 The Rejection Force F_G Associated with the Generation of Cathode Gas

The generation rate of the cathode gas is associated with the electric field strength, the composition of the solution and the electrochemical property of the membrane electric pole surface. Generally a higher electric field strength will produce more gas in a given time, thus dislodging more deposited particles, but also results in greater electric energy consumption and perhaps forms more electrochemical reaction by-products at the same time. On the other hand the pressure in the gas bubble, which will be the same as the hydrostatic pressure of the feed stream, will not be higher if a higher electric field strength is applied. However, because a hydrophobic solid wall has a stronger affinity to the gas bubble than a hydrophilic solid wall does, the fouling removal by the gas bubble will be more effective for those particles which are hydrophobic.

5.2.5 Summary

When a particle deposit on the membrane surface and does not block the pore, if a electric field is applied, the sum of forces acting on the particle is:

$$\vec{\mathbf{F}} = \vec{\mathbf{F}}_{\mathbf{E}} + \vec{\mathbf{F}}_{\mathbf{D}} + \vec{\mathbf{W}} + \vec{\mathbf{H}} \qquad (5\text{-}29)$$

where $\vec{\mathbf{F}}_{\mathbf{E}}$ and $\vec{\mathbf{F}}_{\mathbf{D}}$ are the electric field force and viscous drag force respectively, and are given by from Eq. (5-1) to (5-4) and (5-18). $\vec{\mathbf{W}}$ is the weight of the particle which is given by Eq. (5-20). Compared with other forces, the particle weight is insignificant in UF and MF, and is negligible. $\vec{\mathbf{H}}$ is the *Van Der Waals'* force which depends on the interaction distance and is affected by the surface properties of the particle, membrane and the dispersing medium. Its value is inversely proportional to a six order of the interaction distant. $\vec{\mathbf{H}}$ plays an important role in UF and some MF, but vanishes rapidly as the particle size increases. However, as the particle size decreases, both the importance of the electric field force and the *Van Der Waals'* force increase.

If the particle enters into the pore mouth, the electric field force and the tangential viscous drag force will disappear, and the transmembrane pressure will act as a perpendicular driving force to push the particle through the membrane if the pore size is large enough.

5.3 Formation of Gas Bubbles

By slowly increasing the applied voltage after switching the power on, the condition at which the first gas bubble appeared at the anode and cathode, respectively, could be determined . The results are shown in Table 5-2.

Table 5-2. Condition of the gas bubble first appear

	voltage (V)	Electric field strength (V/cm)
On anode	~2.5	27.73
on cathode	~1	9.09

- Alamin concentration was 0.7%(w/v), pH6.96

Figure 5-4 shows a schematic diagram of the of Alamin particle distribution before and after the electric field was applied, which was drawn according to observations with a

microscope. Since the migration of particles was towards the anode in the electric field, particles were found accumulated in the vicinity of anode, and the generation of gas bubbles on the cathode also rejected the nearby particles. These cathode gas bubbles both appeared earlier and were generated more rapidly than bubbles formed on the anode.

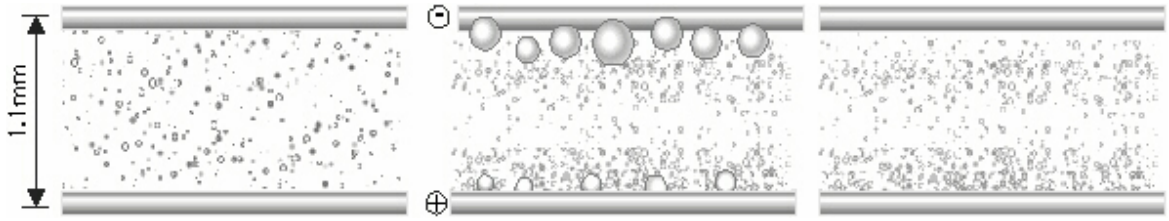

(a)Before electric field applied (b)Formation of Gas bubbles (c)After gas bubble released after electric field applied

Figure 5-4. Schematic diagram of the of Alamin particle distribution after electric field was applied (examined with microscope, 10x10)

According to the *Faraday* electrolysis law [33], the formation rate of gas bubbles is proportional to the membrane current.

$$\mathbf{Q}=\mathbf{n}\cdot\mathscr{F} \tag{5-30}$$

where $\mathscr{F}$ is the *Faraday*' constant (which equals 96520 Coulomb); **n** the number of electrochemical equivalents involved in the reaction and **Q** the amount of electricity (Coulomb) consumed in the electrochemical reaction. The half-cell reaction on the cathode is $2H^{+1} + 2e \rightarrow H_2\uparrow$ in this case. If the electrical current is 1A (1 Coulomb per second), the generation rate of hydrogen gas would be:

$$\mathbf{w_g} = \frac{1}{2\times 96520} = 5.18\times 10^{-6}(\mathbf{mol}\cdot\mathbf{s}^{-1}) \tag{5-31}$$

Provided that the hydrogen gas is the only product of cathode reaction, then the corresponding volume production rate of gas can be estimated by assuming the gas obey the ideal-gas-state equation:

$$\mathbf{V_g} = \mathbf{w_g}\cdot\frac{\mathbf{R_g T}}{\mathbf{P}} = \frac{5.18\times 10^{-6}(\mathbf{mol}\cdot\mathbf{s}^{-1})\times 0.08206(\mathbf{l}\cdot\mathbf{atm}\cdot\mathbf{K}^{-1}\cdot\mathbf{mol}^{-1})\times 293.15(\mathbf{K})}{1(\mathbf{atm})}$$
$$= 1.246\times 10^{-4}(\mathbf{l}\cdot\mathbf{s}^{-1})\ \mathbf{or}\ 7.48(\mathbf{ml}\cdot\mathrm{min}^{-1}) \tag{5-32}$$

where $\mathbf{R_g}$ is the universal gas constant (0.08206 l·atm·K^{-1}·mol^{-1}); **T** the thermodynamic temperature (when the experimental temperature is pre-set to 20°C then T is 293.15K); and **P** is the pressure on the permeate side, which is approximately atmosphere pressure. This gas volume production rate is nominally equivalent to ~24 liters per square meter per hour (LMH) permeate flux, i.e. $\mathbf{J_g} \cong 24$(LMH), which is consistent with the experimentally observed flux increase (4.5.1 -4.5.3) and can be considered as the disturbance caused by gas bubbles to the measurement of permeate flux.

5.4 Electrochemical Corrosion of Stainless Steel

5.4.1 Membrane Serving as the Electrode

If the membrane and the central bar are oppositely charged, they comprise, together with the feed stream, an electrolytic cell. Some electrochemical reactions will therefore take place during filtration. Since the cathode current tends to protect to the electrode, whereas the anode current tends to promote the corrosion of the electrode, and furthermore, since most of colloidal particles have a negative zeta potential in the normal pH range, these are likely reasons that many researchers preferentially established the membrane as the cathode in charged membrane filtration studies.

In some experiments of this research program, in which the membrane served as a cathode and the central bar served as a anode, where the duration was 24 hours, evidence of corrosion was found from the green color precipitate among the white Alamin powder (see Figure 5-5).

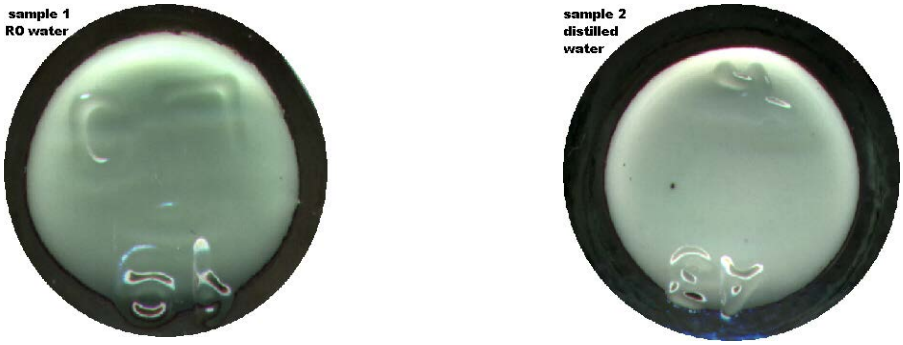

(a) RO water was used (b) Distilled water was used

Figure 5-5. Green color precipitate among Alamin powder(white) after 24 hour

Qualitative chemical analysis [39] was carried out to verify the presence of nickel in the deposit. Nickel is a component of stainless steel, and nickel dioxide exhibits a green color. Nickel was confirmed raising the question as to where this came from, from the anode or cathode?

Since the membrane unit had been used by some other researchers previously, the "frosted" surface of the central bar might be the result of anode chemical etching during filtration or the result of mechanical machining (see figure 5-6). Traces of corrosion etching were also observed on the membrane adapter (see Figure 5-7) indicating that the membrane might have been used as an anode by previous researchers.

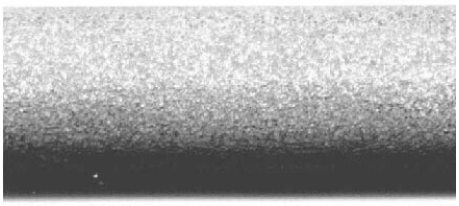

Figure 5-6. The "frosted" surface of the central bar (used as anode)

Figure 5-7. Corrosion trace on membrane adapter

5.4.2 Auxiliary Electrolysis Experiments

In order to study the electrochemical aspects of the membrane process, electrolysis experiments were carried out in a beaker to simulate the charged membrane in solution (see Figure 5-8).

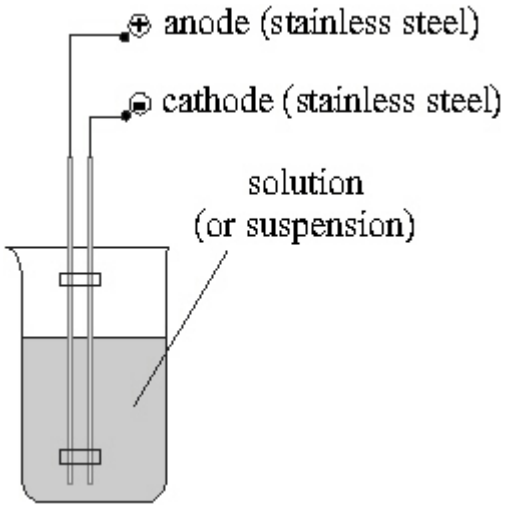

Figure 5-8. Simulative electrolyte experiment
Electrodes gap: 3mm. Electrode current:
0.08A(equivalent to 80A/m^2)

5.4.2.1 Experiment 1 — Anode Corrosion.

When a 0.7%(w/v) Alamin suspension (prepared with RO water) was used, after 24 hours, the anode was found corroded being covered with a layer of browny green, soft mud like deposit (see Figure 5-9). The suspension color changed from milky white to light brown. Brown precipitate was found on the beaker bottom. In contrast to the weight lost on anode, the cathode gained 4mg in weight, which could be considered the error of measurement.

Figure 5-9. Corrosion of the stainless steel anode after electrolyzing the Alamin solution for 24 hours. Alamin particle concentration was 0.7%(w/v). The electrode current was 0.08A(equivalent to 80A/m^2). Voltage applied was 10V(equivalent to 36V/cm of electric field strength).

After washing and cleaning the rust on the electrode with diluted nitric acid (see Figure 5-10 (a) and (b)), the anode weight loss was measured as 40 mg; the corrosion rate was thus equivalent to about 1932 $mg \cdot m^{-2} \cdot hr^{-1}$.

Figure 5-10. Cleaned electrodes. (a)Anode and (b)cathode

5.4.2.2 Experiment 2 — Cathode Deposit

The Alamin filtrate was used in this trial as the electrolyte, as this was expected to be particle free. Although the cathode should repel the negatively charged Alamin particles, the cathodic surface was covered with a tough white film of "deposit" after running overnight. This was similar in appearance to the scale found on the heating surface of a heat-exchanger, and could not easily be removed by rinsing or brushing only (see figure 5-11). Overall it appeared that the film was generated by precipitation from the (supersaturated) solution.

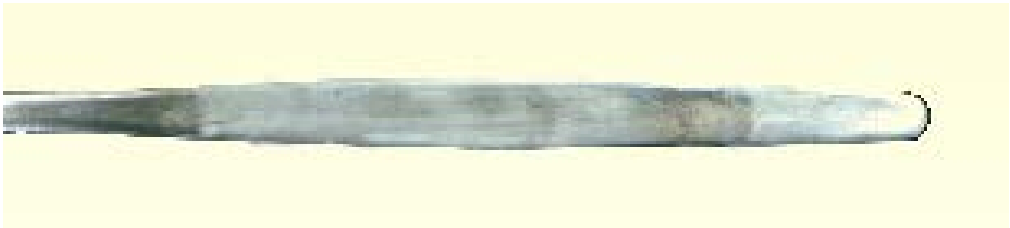

Figure 5-11. Cathodic deposit

5.4.2.3 Experiment 3 — Corrosion Associated With Tap Water

Tap water was used in this experiment to make up the Alamin suspension. The corrosion measured was very severe, giving a value of 1.13×10^{5} $mg \cdot m^{-2} \cdot hr^{-1}$. Relevant data are shown in Table 5-2.

Table 5-2. Corrosion rate of stainless steel in different Alamin suspension

	RO water only	Alamin suspension (0.7% w/v) in RO water	Alamin suspension (0.7% w/v) in tap water
Corrosion rate($mg \cdot m^{-2} \cdot hr^{-1}$)	$<1.37\times10^{3}$	1.93×10^{3}	1.13×10^{5}

5.4.2.4 Experiment 4 — Corrosion Rate at Different Chloride Ion Concentrations

Although many components or impurities in the Alamin solution can aggravate anode corrosion, the chloride ion, according to its electrochemical properties, is considered to be the major reason (see next part). The corrosion rates of the stainless steel anode at chloride concentrations from 0.1 to 1000 ppm were measured at a electric field strength of 33.3V/cm with the results shown in Figure 5-12.

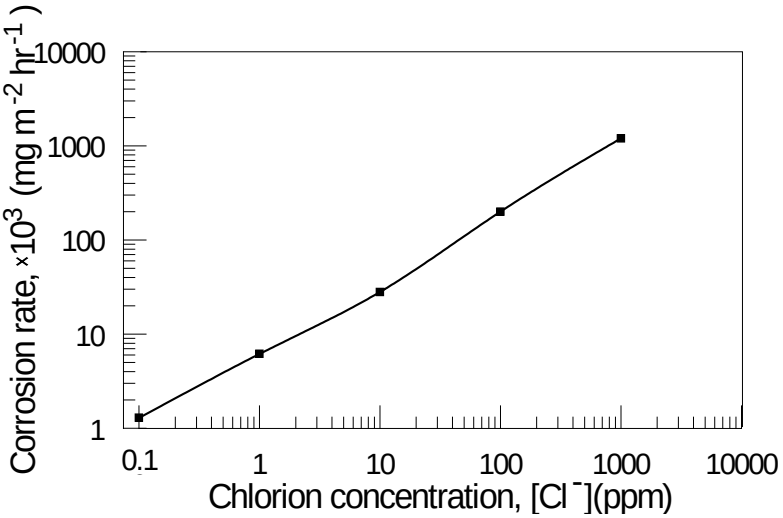

Figure 5-12. Dependence of corrosion rate on chlorion concentration (under electric field strength of 33.3V/cm)

5.4.3. Consideration of The Electrochemical Reactions

According to the results observed above, the following electrochemical reactions are proposed [33,43]. On the anode surface, the following reaction could take place even if only traces of chloride ion exist:

$$2Cl^{-} - 2e \rightarrow Cl_2 \qquad (5\text{-}33)$$

and the secondary reaction follows :

$$Cl_2 + H_2O \rightarrow HClO + H^+ + Cl^- \quad (5\text{-}34)$$

Some other negative charged ions or groups could lose electrons and become oxidizing. For example, hydroxyl may undergo the change:

$$4OH^- - 4e \rightarrow 2H_2O + O_2 \quad (5\text{-}35)$$

These reactions are either hydrogen ion generating or hydroxyl consuming which creates a local acidic environment on the anode surface. On the other hand, newborn hyperchloride or other species formed at the anode are strongly oxidizing in acidic conditions. Thus even the stainless steel can be etched by corrosion. For example, after dissolving the protective oxide film, hyperchloride can consequently oxidize the nickel atom leading to the formation of a nickel oxide precipitation, which is a green substance[37].

$$Ni + ClO^- \longrightarrow NiO\downarrow + Cl^- \quad (5\text{-}36)$$

Another consequence in the acidified vicinity of the anode is the dissolving of Alamin or calcite. Because of the feed stream was recycled in this study, the chloride in it would also undergo a circulation through the different oxidation states shown in Eq.(5-33), (5-34) and (5-36). These processes can be simplified as in Figure 5-13.

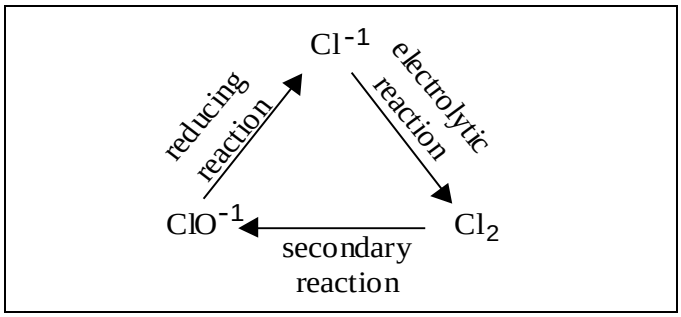

Figure 5-13. Circulation of the chloride in different oxidative state in a recycle filtration system

On the cathode surface at the same time, water molecules were split into hydrogen and hydroxyl ions creating a high pH local environment.

$$H_2O + 2e \rightarrow H_2 + 2OH^- \quad (5\text{-}37)$$

It was considered that the following balances existed in the Alamin solution:

$$Ca_3(PO_4)_2 \downarrow + H_2O \square CaHPO_4 + OH^- \qquad K_{sp(5)} = 2.0x10^{-29} \qquad (5\text{-}38)$$

$$CaHPO_4 \downarrow + H_2O \square Ca^{++} + H_2PO_4^- + OH^- \qquad K_{sp(6)} = 1x10^{-7} \qquad (5\text{-}39)$$

Since the value of $K_{sp(5)}$ is much less than that of $K_{sp(6)}$, a rise of pH would make the above equilibrium move to the left and a precipitate of $Ca_3(PO_4)_2$ would form as a result.

5.4.4 Anode Corrosion Examined with Microscope

As the electric field was applied, spots of corrosion on the stainless steel anode slowly appeared. Since the iron suffered the anodic oxidation:

$$Fe - 2e^- \longrightarrow Fe^{2+} \qquad (5\text{-}40)$$

and

$$Fe^{2+} - e^- \longrightarrow Fe^{3+} \qquad (5\text{-}41)$$

This gives:

$$4Fe + 12H_2O - 12e^- \longrightarrow 4\,Fe(OH)_3 + 12H^+ \text{ or } 4FeO(OH) + H^+ \qquad (5\text{-}42)$$

(brown floccule)

and a brown floccule of $Fe(OH)_3$ gradually appeared on the vicinity of the anode (See figure 5-13). Some of this material dispersed into the bulk solution, the remainder became dense slowly and formed a rusty layer on the anode surface finally.

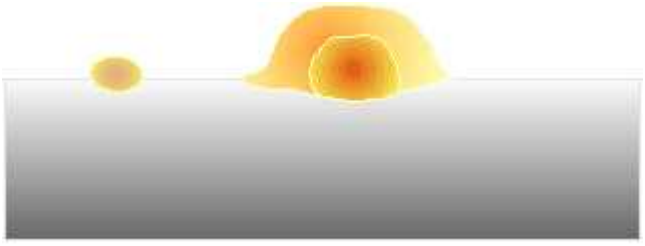

(a) Anode corrosion starts with metal component dissolving

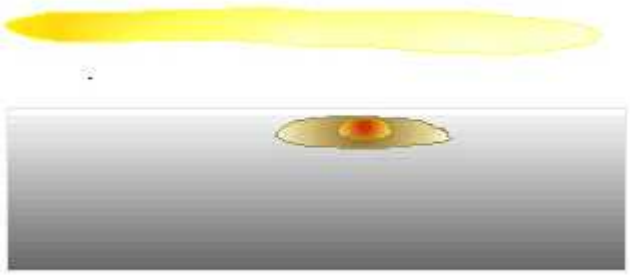

(b)Formation of the floccule

Figure 5-14. Initial period of anodic corrosion

5.5 Formation of Cathode Deposit: A Dynamic Filtering Layer

The cathode deposit on the membrane surface was believed to result from calcium salt crystallization from the solution. The species and content of calcium salts will therefore affect the deposit directly, and the solubility product of calcium salts will determine their precipitating sequence. For the Alamin in this study, since it comprised calcium and phosphorus, according to Eq. (5-38) and (5-39) the cathode deposit was mainly calcium phosphate ($Ca_3(PO_4)_2$). In the calcite solution, however, the following balance existed:

$$CaCO_3\downarrow + H_2O \square Ca^{+2} + HCO_3^- + OH^- \qquad K_{sp}=3.1\times10^{-7} \qquad (5\text{-}43)$$

So the cathode deposit would be calcium carbonate ($CaCO_3$).

The newly formed crystallites precipitated from supersaturated solution are adsorptive and/or likely to be absorbed because of their unsaturated surface charge. The cathode

deposit layer is therefore thin and compact, it could be a FIP* filtering layer itself to some particles or macro-molecular species.

According to the electric-magnetic field theory [24], the distribution of electric field strength upon the membrane surface is illustrated by the electric lines of force in Figure 5-15. This shows that the density of electric lines of force inside the membrane pore is zero, i.e., the electric field strength is zero inside the pore channel. The electric field only exists in the gap between the central bar and the membrane, and has the highest field strength around the pore mouth or on some tips of the membrane surface. The activated points upon which the electrochemical reactions take place are limited to these spots. Therefore the primary deposition caused by electrochemical reaction is limited to the membrane surface (specially around the pore mouth) instead of inside the pore tunnel. If the transmembrane pressure is maintained at zero during the cathode deposition, the deposit layer will just arise on the top of the porous matrix surface and pore blocking can be limited or avoided. This will give the newly formed cathode deposit layer some filtering characteristic. On the other hand this dynamic filtering layer can also be dissolved or dislodged off if the reverse voltage is applied. Further studies is suggested into the properties and the potential practical use of the cathode deposit layer.

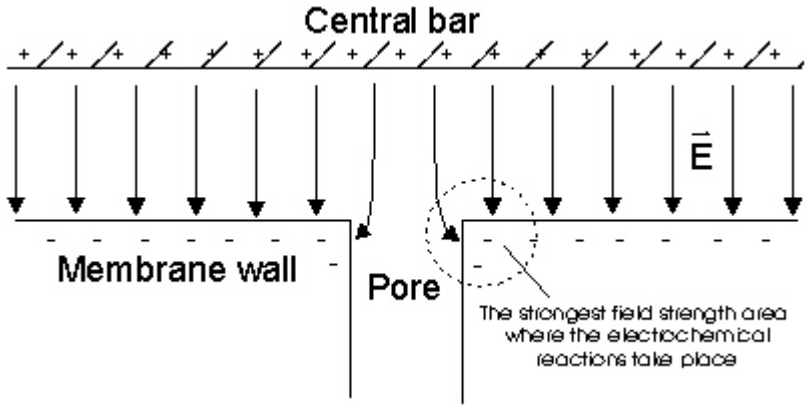

Figure 5-15. The distribution electric field strength on the membrane surface

* :FIP— Formed In Place

6. Fouling and Cleaning of the Membranes

6.1 Mechanisms of Fouling

The membrane will be fouled to a varying extent after each experiment. Examination of the membrane surface revealed no macroscopic deposit was formed for the experiments at 1.25 to 2.28m/s cross flow velocity (Figure 4-12 in 4.4.2), rather the filtering surfaces looked fairly clean no matter how much the membrane had been fouled. Note that the nominal membrane pore size is approximately equal to the value of the average particle dimension (see section of 3.4.2). According to the analysis of the forces acting on a particle deposited on the membrane surface (section 5.4), it can be concluded that the major fouling mechanism for this condition is pore plugging and/or inner adsorption — i.e. those particles smaller than the membrane pore size are expected to enter and stay in the membrane apertures.

When an external electric field is imposed it alters the fouling properties. Using the membrane as cathode tends to reject those negatively charged particles (or colloids) while producing an alkaline permeate by electrolysis. This in turn decreases the solubility of the calcium salts and eventually causes a deposit to form which is normally harder than the ordinary deposit cake (section 5.3.). When operated as an anode, the membrane tends to attract the particles (or colloid) because of their negative charge in the normal pH range (section 5.2.2 and Figure 5-4), and also produces an acidic permeate. The process is a solvent electrolysis to most of the calcium salts. However, anode corrosion will take place if the membrane is made of ordinary metallic materials including stainless steel; to avoid such corrosion the use of a sintered titanium membrane may be an option.

6.2 Cleaning and Restoration of Membrane Performance

The following cleaning methods were used in this study: backflushing; acid cleaning; alkali cleaning and mechanical brushing. The effectiveness of these methods was evaluated by testing the ability of the procedure to restore flux.

6.2.1 Backflushing

Backflushing proved effective if the pressure applied was high enough. In this study, tap water was used for this operation. The pressure tested was 50kPa, 100kPa and 200kPa for the 5μm membrane, and 30kPa and 50kPa for the 25μm membrane. Higher pressure will make the backflushing more effective. The results indicate that the backflush pressure for 5μm membrane should be at least 100kPa. A pressure at 200kPa or higher gave a better result with regard to flux restoration, but since the membrane jacket was made of perspex material, its strength limited the backflushing pressure that could be applied. Consequently the routine backflush cleaning pressure for the 5μm membrane was set to 100kPa. A 50kPa backflush pressure was used for the 25μm membrane, as it could be cleaned more easily. The major advantage of high pressure backflushing is that it reduces the consumption of chemical cleaner.

There was a significant difference in the effectiveness of backflushing between two membranes used. For example, 59% of filtration performance of the 25μm membrane could be restored by a simple stop-and-restart operation in which there is only about 15mm H_2O water column backflushing pressure provided by the permeate tube itself, and 85% filtration performance was restored at 30kPa backflushing pressure (see Figure 6-1). However, over 250kPa backflushing pressure had to be used to restore 85% filtration performance on the 5μm membrane if only backflushing was used.

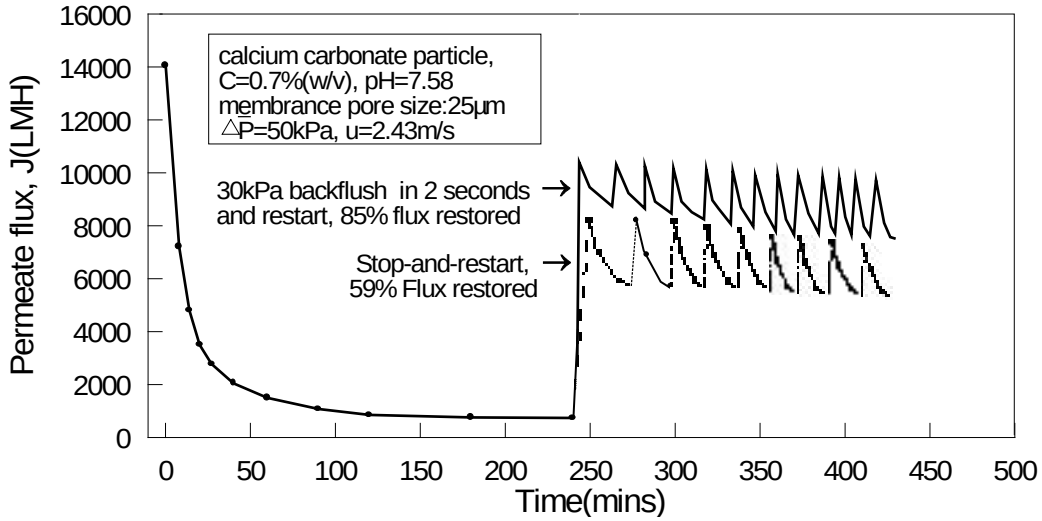

Figure 6-1. Effectiveness of backflushing on the 25μm membrane

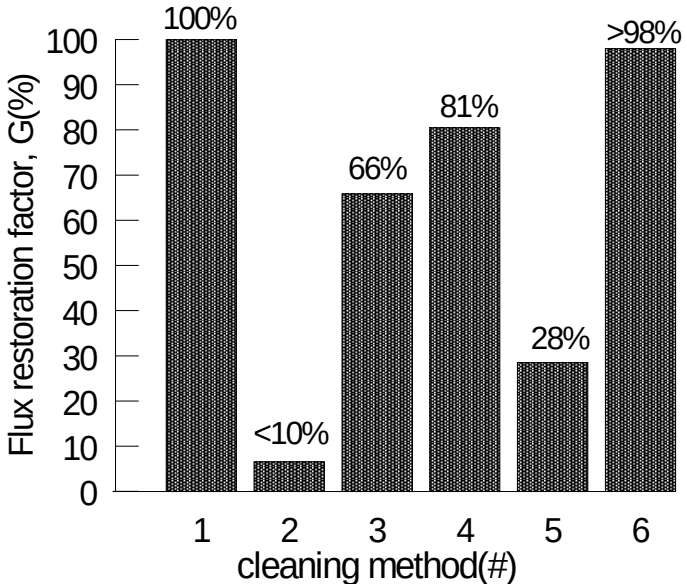

Figure 6-2. Effectiveness of different cleaning methods, single or in combination
#1: Original membrane
#2: 20L tap water backflushing at 50kPa
#3: 100L tap water backflushing at 100kPa
#4: 80L tap waters backflushing at100kPa, 0.2% Nitric acid washing for 10mins,
#5: mechanical brush and water rinse
#6: 4x20L tap water backflushing at 100kPa, 0.2% Nitric acid washing for 20mins, 10L RO water rinsing.

6.2.2 Acid Cleaning

Some foulant can only be removed through dissolution by using a chemical cleaner. Hydrochloride acid and nitric acid were tried in this study. However, since the concentrated chloride ion may be a corrosive to stainless steel [35], and the residue of hydrochloride acid in the system, if there is any, can cause the anode corrosion when the electric field is applied (chapter 5), nitric acid was selected for routine use as the chemical cleaner.

Figure 6-2 shows the effectiveness of these cleaning methods and their combinations. The standard routine cleaning procedure (see 3.2.6) was based on method #6. However the water remaining in the membrane jacket should be drained in order to minimized the residual acids. For this reason, two final rinsings were used.

6.2.3 Other cleaning options

Alkali cleaning using an NaOH solution (0.2%) was used once a week in addition to routine acid cleaning in order to clean those foulant that can not be removed by acid cleaning. Mechanical brushing was tested as well by using a extended testing-tube brush. However the effectiveness of the method in restoring the filtration performance was so poor implying that the fouling was located inside the membrane pore.

As discussed before in 4.5.3, a positively charged membrane can acidify its local environment in the vicinity of the membrane wall, so as to cause a dissolving effect to calcium salts. This can be utilized to enhance the cleaning operation, for example, to anodize the membrane while performing the backflushing operation providing that the chloride ion concentration in the backflushing water (e.g. tap water) is less than 0.1ppm, because the anodic corrosion on this chloride level is slight (section 5.4.2.4 and Figure 5-13). This may be helpful in reducing the cleaning time and the consumption of acid cleaner, and thus warrants further study.

7. Conclusions and Recommendations

The filtration fluid used in this study was a calcium-rich suspension derived from dariy processing. Application of electromicrofiltration resulted in a transient improvement of permeate flux after an electric field was imposed in which the membrane acted as the cathode. The reason for this phenomenon is (1) electrostatic repulsion of the particles from the charged membrane; and (2) the dislodging effect of the cathodic gas bubbles on deposited particles on the membrane. Continuous application of the electric field, however, can aggravate membrane fouling, because the electrolysis reaction alkalize the permeate, reducing the solubility of calcium salts and eventually causing cathode deposition. The result of a EMF in which a manually controlled pulsatile electric field was applied indicated that the permeate flux was increased. Thus the use of a DC power supply with adjustable pulse output function (e.g. 0-100V pulsation high, 0-5 minute pulsation width and 5-30 minute pulsation period) is therefore recommended in the future studies to benefit such dairy filtration processes.

Reversing the membrane polarity so that it works as an anode will improve steady state permeate flux by about 2- to 3-fold compared to filtration without an applied field. However the drawbacks of this method are the acidification of the permeate ($pH \leq 3.5$) and the oxidizing potential of the anodized membrane. Nevertheless, the calcium salt dissolving effect of the anodized membrane can be applied advantageously in the cleaning operation. For example, anodizing the membrane during backflushing operation could be an effective alternative to acid cleaning if the backflushing water is chloride free or at least under 0.1ppm content. This may reduce both the cleaning time and acid consumption in cleaning.

Electrophoretic examination showed that the Alamin particles were negatively charged in the normal pH range, and that the electrophoretic speed of a 1μm particle towards the anode was on average 42μm/s at 36V/cm electric field strength. On the other hand the hydrodynamic analysis indicated that the flow pattern was fully developed turbulent flow at the 2.28m/s crossflow velocity almost all over the membrane module and that the laminar sub-layer was 81μm at this condition. Since the average residential time of particles in the bulk solution through the membrane unit was very short (<0.17s) at this velocity, the effective extent of the electric field

where the electric repulsion could change the particle trajectories would be located within the laminar sub-layer and around 10μm above the membrane.

Fouling and cleaning have been one of the principal subjects for membrane research as they are key features in the application of membrane processes. The major fouling mechanism was found to be pore plugging in this particle-membrane system. An effective routine cleaning method was the combination of backflushing and acid washing. Alkaline washing was applied once a week to remove the foulants that could not be done by acid washing. Mechanical brushing, however, had a poor cleaning effect.

The cathode deposition of calcium salts due to the applied electric field was found to produce a compact film which can serve as a dynamic filtering layer. The formation of this on the surface of the porous stainless steel matrix constitutes an asymmetric membrane. In this way the drawback of large pore size and size distribution found with the sintered stainless steel membrane may be overcome. It is recommended that the formation and the utilization of this dynamic layer should be given more attention in any future study, or a compact skin layer on the top of the porous stainless steel should be investigated to prevent pore plugging. As it was mentioned in section 1.1 for the “Micro-Steel” and the “Scepter” stainless steel membranes[36,37] .

In summary, since the electrochemical oxidation-reduction involved in a EMF process may possibly change the chemical properties of the filtered substance, and alter the permeate pH as well, these aspects must be taken into consideration when applying the EMF or EUF for bioseparations.

8. Appendices — Measurement of the Specific Weight and Porosity of Alamin Particle

The specific weight of Alamin particles was measured with the volume-weight method. A 129.5ml (V) cylindrical container with apertures at the bottom was used to measured the apparent volume of the Alamin particle (Figure 9-1). Placing a circular filter paper on the bottom of it, the Alamin was then fully filled into the container. The net weight of the Alamin was measured to be $\mathbf{W_A}$ =91.830g. The cylinder was submerged into the water, so that water penetrated into the container through filter at the bottom. The Alamin (including the upper part) eventually become saturated by absorbed water by capillary effect, although this process was very slow and could take about 24 hours. The amount of absorbed water was calculated from the gain in weight which is $\mathbf{W_w}$ = 88.890g in this case; correspondingly the volume of this water is $\mathbf{V_w}$ = 89.050ml at 20°C. Thus the Alamin particle specific weight can be expressed as

$$\rho_p = \frac{\mathbf{W_A}}{\mathbf{V - V_w}} = \frac{91.830(\mathbf{g})}{129.5(\mathbf{ml}) - 89.050(\mathbf{ml})} = 2.27(\mathbf{g/ml})$$

The apparent specific weight of Alamin is

$$\rho' = \frac{\mathbf{W_A}}{\mathbf{V}} = 0.709(\mathbf{g/ml})$$

The porosity of Alamin is therefore

$$\Psi = \frac{\mathbf{V_w}}{\mathbf{V}} = \frac{89.050}{129.443} \approx 68.8\%$$

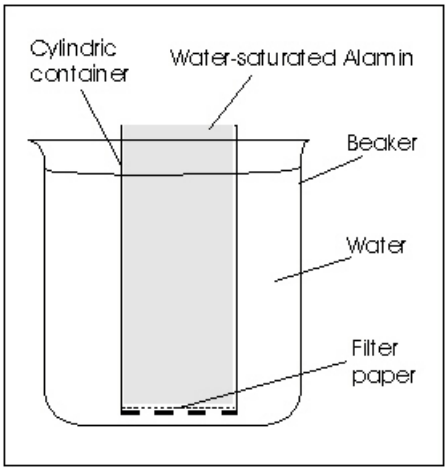

Figure 9-1. Measurement of the specific weight and porosity of Alamin

8. References

[1] Cheryan, Munir (1986). Ultrafiltration Handbook. Technomic Publishing Company, Lancaster.

[2] Rautenbach, R., and Albrecht, R. (1989). Membrane Processes. John Wiley & Sons Ltd.

[3] Loeb, S. & Sourirajan, S. (1963). Sea water demineralization by means of an osmotic membrane. *Am. Chem. Soc.*, Chem. Ser., ACS **38**: 117-132

[4] Scott, Jeanette (Editor). (1980). Membrane and ultrafiltration technology : recent advances. Park Ridge, N.J. : Noyes Data Corp.,

[5] http://membrane.ct.utwente.nl/serve/MTG/ (the World wide web site of Membrane Technology Research Group, University of Twente, Enschede, The Netherlands)

[6] Goudedranche, H., Maubois, J.L., Ducruet, P. & Mahaut, M. (1980). Utilization of the new mineral UF membrane for making semi-hard cheeses. *Desalination* **35**:243-258

[7] Ladd M.F.C. (1986). Introduction to physical chemistry, Cambridge [Cambridgeshire] ; New York : Cambridge University Press.

[8] Wakemam R.J. (1986). Eletriofiltration: Microfiltration plus eletrophoresis. *The Chemical Engineer* (**June**), 65-70.

[9] Wakemam R.J., & E.S. Tarleton (1986). Experiments using electricity to prevent Fouling in Membrane Filtration. Filtration and Separation. (**May**/**June**), 174-176

[10] Wakemam R.J., & M.N. Sabri (1995). Utilising Pulsed Flow Electriic Field in Crossflow Microfiltration of Titania Suspension. Transaction of the Institute of Chemical Engineers (a). 455-463

[11] Akay, G., R. J. Wakeman (1996). Electric field intensification of surfactant mediated separation. Chemical Engineering research and design.74(5):517-525,

[12] Henry, J.D.Jr., Lawler, L.F., Kuo, C.H.A. (1977). A solid/liquid separation process process based on cross flow and electrofiltration. American Institute of Chemical Engineers Journal.23(6). 851.

[13] Moulik, P. (1971). Physical aspects of electrofiltration. Environmental Science and Technology. 5(9): 771~776.

[14] Radovich, J.M., B.Behnam(1985). Steady-state modelling of electroultrafiltration at constant concentrations. Separation Science and Technology 20(4): 315-329

[15] Reeve, Clinton John. Master of Technology Thesis (1997): Characterisation of an electromicrofiltration unit for use in bio-separation processes. Massey University, New Zealand

[16] Lee, C.H., Gidaspow, D., Wasan, D.T. (1980). Cross-flow electrifilter for nonaqueous slurries. *Industrial Engineering and Chemical Fundamentals*. (**19**) 166-175.

[17] Bowen, W.R., Sabumi H.A.M.(1991): Electric enhanced membrane filtration at low cross-flow velocities. *Industrial Engineering Chemical Research.* (**30**) 1573-1579

[18] International Dairy Federation Special Issue No. 9201(1991). New Applications of Membrane Processes

[19] International Dairy Federation_Special Issue No. 9504.(1995). Fouling and Cleaning in Pressure Driven Membrane Processes.

[20] Walstra, P. and Jenness, R. (1984). Dairy Chemistry and Physics. John Wiley & Sons Ltd. New York

[21] Lyster, R.L.J. (1979) . The equilibria of calcium and phosphate ions with the micellar calcium phosphate in cow's milk . *Journal of Dairy Res*.46:343-346

[22] International Dairy Federation. (1985). New Dairy Products via New Technology. *IDF Seminar*, Atlanta, USA. **Oct**.

[23] David R. Lide (Editor-in-chief, 1995-1996): CRC Handbook of Chemistry and Physics, 76th ed. Page 6-159

[24] Joseph W. Kane, Morton M. Sternheim (1988). Physics, 3rd ed. New York : Wiley, Page 354-355.

[25] Hsieh, H.P., Bhave, R.R. & Fleming, H.L. (1988). Microporous alumina membranes. *J. Membrane Sci*. **39**:221-241

[26] Wu, D., Howell, J.A. & Field, R.W. (1993). Pulsatile flow filtration of yeast cell debris: Influence of preincubation on performance. *Biotechnol. Bioeng*. **41**: 998-1002

[27] Bier M. Br Patent 936805. (1963).

[28] Marshall, A.D. (1994). Microfiltration membrane fouling by dairy proteins. thesis submitted for the degree of Doctor of Philosophy at Massey University, New Zealand.

[29] http://www.irl.cri.nz/ (the World Wide Web site of Industrial Research Limited(NZ))

[30] http://www.kochmembrane.com/ (the World Wide Web site of Koch Membrane Systems, Inc.)

[31] Bowen, W.R. & Hughes, D.T.(1991). Properties of microfiltration membrane, Adsorption of bovine serum albumin at aluminium oxide membranes. *J. Memebr. Sci.*,**51**, 189-200

[32] Bowen, W.R. & Goenaga, X. (1989). Electrically enhanced membrane filtration. Cross-flow microfiltration and electrofiltration at aluminium oxide membranes. *Proceedings of the International Congress on Inorganic membranes*, ed. L. Cot. and J. Charpin, Montpellier

[33] Edmud C. (1956). Potter: Electrochemistry --Principles & Application,(Cleaver-Hume Press Ltd.)

[34] 印永嘉主编：大学化学手册。山东科学技术出版社。1985，page 99.
[Yin Yong Jia (Chief-Editor): Academic Chemistry Handbook. ShanDong Science and Technology Publishing Company. China. 1985. page 99.]

[35] Page, G. G. (George Geoffrey): Stainless steels for the food industry. Wellington, N.Z. : Science Information Publishing Centre, Dept. of Scientific and Industrial Research, 1984

[36] MSS. (1995). Micro-steel Caustic Recovery System; Mem-Brine System, Membane System Specialists, Wisconsin Rapids, WI

[37] Graver Separations. (1996) Lit. No.s-106, Glasgow, DE.

[38] Coulson, J.M. and Richardson, J. F. (1990-<1991>): Chemical Engineering, 4th ed. Oxford [England]; New York : Pergamon Press.

[39] Revised by G. Svehla PhD (Sixth Edition): Vogel's Qualitative Inorganic analysis. FRSC Reader in Analytical Chemistry, Queen's University, Belfast. Page 120

[40] Field R.W., D. Wu, J.A. Howell, B.B Gupta: Critical flux concept for microfiltration fouling, Journal of Membrane Science. 1995, 100, 259-272.

[41] Howell John A.: Sub-critical flux operation of mecrofiltration, Journal of Membrane Science. 1995, 107, 165-171

[42] Gupta B.B, J.A. Howell, D.X. Wu and Field: Helical baffle in cross -flow microfiltration. Journal of Membrane Science. 1995, 102, 31-42.

[43] 曹忠良 王珍云编：无机化学反应方程式手册 湖南科学技术出版社 1982，page 3,373
[Cao zhong liang and Wang yun zhen (1982): Inorganic Chemical Reaction Handbook. HuNan Science and Technology Publishing Company. China. 1982. page 2, 373.]

[44] Gordon M. Barrow (1996): Physical Chemistry. 6th Edition. The McGraw-Hill Companies, Inc. Page 39

9. Appendix — Measurement of the Specific Weight and Porosity of Alamin Particle

The specific weight of Alamin particles was measured with the volume-weight method. A 129.5 ml (V) cylindrical container with apertures at the bottom was used to measure the apparent volume of the Alamin particle (Figure 9-1). After placing a circular filter paper on the bottom of it, the Alamin was then fully filled into the container. The net weight of the Alamin was measured to be $\mathbf{W_A}$ =91.830 g. The cylinder was submerged into the water, so that water penetrated into the container through the filter at the bottom. The Alamin (including the upper part) eventually become saturated by absorbed water through the capillary effect, although this process was very slow and could take about 24 hours. The amount of absorbed water was calculated from the gain in weight which is $\mathbf{W_w}$ = 88.890 g in this case; correspondingly the volume of this water is $\mathbf{V_w}$ = 89.05 ml at 20°C. Thus the Alamin particle specific weight can be expressed as

$$\rho_p = \frac{\mathbf{W_A}}{\mathbf{V} - \mathbf{V_w}} = \frac{91.830(\mathbf{g})}{129.5(\mathbf{ml}) - 89.050(\mathbf{ml})} = 2.27(\mathbf{g/ml})$$

The apparent specific weight of Alamin is

$$\rho' = \frac{\mathbf{W_A}}{\mathbf{V}} = 0.709(\mathbf{g/ml})$$

The porosity of Alamin is therefore

$$\Psi = \frac{\mathbf{V_w}}{\mathbf{V}} = \frac{89.050}{129.443} \approx 68.8\%$$

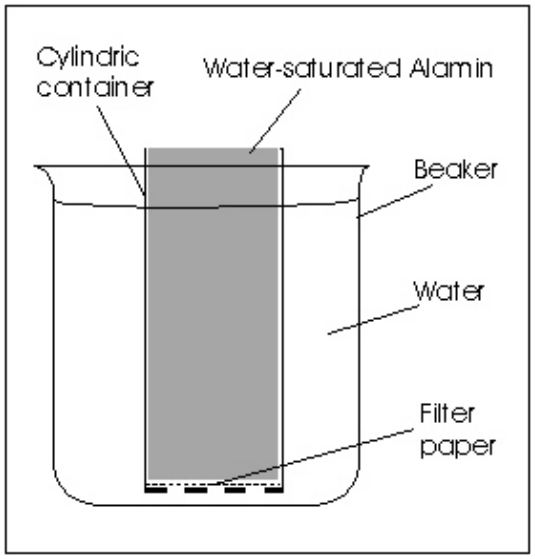

Figure 9-1. Measurement of the specific weight and porosity of Alamin

9. References

[1] Cheryan, Munir (1986). Ultrafiltration Handbook. Technomic Publishing Company, Lancaster.

[2] Rautenbach, R., and Albrecht, R. (1989). Membrane Processes. John Wiley & Sons Ltd.

[3] Loeb, S. & Sourirajan, S. (1963). Sea water demineralization by means of an osmotic membrane. *Am. Chem. Soc.*, Chem. Ser., ACS **38**: 117-132

[4] Scott, Jeanette (Editor). (1980). Membrane and ultrafiltration technology : recent advances. Park Ridge, N.J. : Noyes Data Corp.,

[5] http://membrane.ct.utwente.nl/serve/MTG/ (the World wide web site of Membrane Technology Research Group, University of Twente, Enschede, The Netherlands)

[6] Goudedranche, H., Maubois, J.L., Ducruet, P. & Mahaut, M. (1980). Utilization of the new mineral UF membrane for making semi-hard cheeses. *Desalination* **35**:243-258

[7] Ladd M.F.C. (1986). Introduction to physical chemistry, Cambridge [Cambridgeshire] ; New York : Cambridge University Press.

[8] Wakemam R.J. (1986). Eletriofiltration: Microfiltration plus eletrophoresis. *The Chemical Engineer* (**June**), 65-70.

[9] Wakemam R.J., & E.S. Tarleton (1986). Experiments using electricity to prevent Fouling in Membrane Filtration. Filtration and Separation. (**May**/**June**), 174-176

[10] Wakemam R.J., & M.N. Sabri (1995). Utilising Pulsed Flow Electriic Field in Crossflow Microfiltration of Titania Suspension. Transaction of the Institute of Chemical Engineers (a). 455-463

[11] Akay, G., R. J. Wakeman (1996). Electric field intensification of surfactant mediated separation. Chemical Engineering research and design.74(5):517-525,

[12] Henry, J.D.Jr., Lawler, L.F., Kuo, C.H.A. (1977). A solid/liquid separation process process based on cross flow and electrofiltration. American Institute of Chemical Engineers Journal.23(6). 851.

[13] Moulik, P. (1971). Physical aspects of electrofiltration. Environmental Science and Technology. 5(9): 771~776.

[14] Radovich, J.M., B.Behnam(1985). Steady-state modelling of electroultrafiltration at constant concentrations. Separation Science and Technology 20(4): 315-329

[15] Reeve, Clinton John. (1997): Characterisation of an electromicrofiltration unit for use in bio-separation processes. A thesis submited in partial fulfillment of the requirement for the degree of MASTER OF THCHNOLOGY in Massey University, New Zealand

[16] Lee, C.H., Gidaspow, D., Wasan, D.T. (1980). Cross-flow electrifilter for nonaqueous slurries. *Industrial Engineering and Chemical Fundamentals*. (**19**) 166-175.

[17] Bowen, W.R., Sabumi H.A.M.(1991): Electrical enhanced Membrane Filtration at Low Cross-flow Velocities. *Industrial Engineering Chemical Research.* (**30**) 1573-1579

[18] International Dairy Federation Special Issue No. 9201(1991). New Applications of Membrane Processes

[19] International Dairy Federation_Special Issue No. 9504.(1995). Fouling and Cleaning in Pressure Driven Membrane Processes.

[20] Walstra, P. and Jenness, R. (1984). Dairy Chemistry and Physics. John wiley & Sons Ltd. New York

[21] Lyster, R.L.J. (1979) . The equilibria of calcium and phosphate ions with the micellar calcium phosphate in cow's milk . *Journal of Dairy Res*.46:343-346

[22] International Dairy Federation. (1985). New Dairy Products via New Technology. *IDF Seminar*, Atlanta, USA. **Oct**.

[23] David R. Lide (Editor-in-chief, 1995-1996): CRC Handbook of Chemistry and Physics, 76th ed. Page 6-159

[24] Joseph W. Kane, Morton M. Sternheim (1988). Physics, 3rd ed. New York : Wiley, Page 354-355.

[25] Hsieh, H.P., Bhave, R.R. & Fleming, H.L. (1988). Microporous alumina membranes. *J. Membrane Sci*. **39**:221-241

[26] Wu, D., Howell, J.A. & Field, R.W. (1993). Pulsatile flow filtration of yeast cell debris: Influence of preincubation on performance. *Biotechnol. Bioeng*. **41**: 998-1002

[27] Bier M. Br Patent 936805. (1963).

[28] Marshall, A.D. (1994). Microfiltration membrane fouling by dairy proteins. thesis submitted for the degree of Doctor of Philosophy at Massey University, New Zealand.

[29] http://www.irl.cri.nz/ (the World Wide Web site of Industrial Research Limited(NZ))

[30] http://www.kochmembrane.com/ (the World Wide Web site of Koch Membrane Systems, Inc.)

[31] Bowen, W.R. & Hughes, D.T.(1991). Properties of microfiltration membrane, Adsorption of bovine serum albumin at aluminium oxide membranes. *J. Memebr. Sci*.,**51**, 189-200

[32] Bowen, W.R. & Goenaga, X. (1989). Electrically enhanced membrane filtration. Cross-flow microfiltration and electrofiltration at aluminium oxide membranes. *Proceedings of the International Congress on Inorganic membranes*, ed. L. Cot. and J. Charpin, Montpellier

[33] Edmud C. (1956). Potter: Electrochemistry --Principles & Application,(Cleaver-Hume Press Ltd.)

[34] 印永嘉主编：大学化学手册。山东科学技术出版社。1985，page 99.
[Yin Yong Jia (Chief-Editor): Academic Chemistry Handbook. ShanDong Science and Technology Publishing Company. China. 1985. page 99.]

[35] Page, G. G. (George Geoffrey): Stainless steels for the food industry. Wellington, N.Z. : Science Information Publishing Centre, Dept. of Scientific and Industrial Research, 1984

[36] MSS. (1995). Micro-steel Caustic Recovery System; Mem-Brine System, Membane System Specialists, Wisconsin Rapids, WI

[37] Graver Separations. (1996) Lit. No.s-106, Glasgow, DE.

[38] Coulson, J.M. and Richardson, J. F. (1990-<1991>): Chemical Engineering, 4th ed. Oxford [England]; New York : Pergamon Press.

[39] Revised by G. Svehla PhD (Sixth Edition): Vogel's Qualitative Inorganic analysis. FRSC Reader in Analytical Chemistry, Queen's University, Belfast. Page 120

[40] Field R.W., D. Wu, J.A. Howell, B.B Gupta: Critical flux concept for microfiltration fouling, Journal of Membrane Science. 1995, 100, 259-272.

[41] Howell John A.: Sub-critical flux operation of mecrofiltration, Journal of Membrane Science. 1995, 107, 165-171

[42] Gupta B.B, J.A. Howell, D.X. Wu and Field: Helical baffle in cross -flow microfiltration. Journal of Membrane Science. 1995, 102, 31-42.

[43] 曹忠良 王珍云编：无机化学反应方程式手册 湖南科学技术出版社 1982，page 3,373
[Cao zhong liang and Wang yun zhen (1982): Inorganic Chemical Reaction Handbook. HuNan Science and Technology Publishing Company. China. 1982. page 2, 373.]

[44] Gordon M. Barrow (1996): Physical Chemistry. 6th Edition. The McGraw-Hill Companies, Inc. Page 39

10. Nomenclature

Symbol	Description	Units
A_p	Cross-sectional area of the particle	m^2
C_D	Drag coefficient of fluid on the particle	
c	concentration	%(w/v)
d_1	Diameter of the central bar	mm or m
d_2	Diameter of the tubular membrane	mm or m
d_e	Equivalent diameter of the membrane module	mm or m
d_m	Maximal pore size of the membrane	μm or m
E	Electric field strength	$V \cdot cm^{-1}$
$\mathscr{F}$	*Faraday*' constant (≡96520 C)	C (Coulomb)
F_E , $\vec{F}_E$	Electric field force(F_E) or force vector ($\vec{F}_E$) acting on the particle	N
F_D , $\vec{F}_D$	Viscous drag force (F_D) or vector force ($\vec{F}_D$) acting on the particle	N
g	Weight acceleration constant(=9.81)	$m \cdot s^{-2}$
J	Permeate flux	$l \cdot m^{-2} \cdot hr^{-1}$ or LMH
J_w	Pure water flux	$l \cdot m^{-2} \cdot hr^{-1}$ or LMH
J_g	False permeate flux cause by cathode gas	$l \cdot m^{-2} \cdot hr^{-1}$ or LMH
K_{sp}	Constant of solubility product	
n	Number of electrochemical equivalent	
P	Pressure	kPa
P_{in}	Inlet pressure of feed stream	kPa
P'_{in}	Transducer reading of the feed pressure at inlet	kPa
P_{out}	Outlet pressure of feed stream	kPa
P'_{out}	Transducer reading of the feed pressure at outlet	kPa
P_{per}	Permeate pressure	kPa
P'_{per}	Gauge reading of permeate pressure	kPa
ΔP_{TP}	Transmembrane pressure	kPa
ΔP_H	Hydrostatic pressure drop	kPa
$\Delta P_{TM,C}$	Critical transmembrane pressure	kPa
Q	Amount of electricity consumed in the electrochemical reaction	C
q	Particle charge	C
R_0	Shear stress on the membrane surface	$N \cdot m^{-2}$
R	Total Resistance to the filtration	m^{-1}
Re	*Reynolds'* number	
R_m	Membrane resistance	m^{-1}
R_g	Universal gas constant (=0.08206)	$l \cdot atm \cdot K^{-1} \cdot mol^{-1}$
r	Radius	m
SD	Standard deviation	

Symbol	Description	Units
t	Time	s or min or hour
TMP	Transmembrane pressure, i.e. ΔP_{TM}	kPa
T (or θ)	Temperature	K or C°
u	Cross flow velocity	$m \cdot s^{-1}$
$\mathbf{u_b}$	Velocity at the edge of the laminar sub-layer	$m \cdot s^{-1}$
$\mathbf{u_d}$	Average relative velocity of particle and fluid for a mean size particle on membrane surface	$m \cdot s^{-1}$
$\mathbf{u_s}$	The maximum velocity in the membrane annular space	$m \cdot s^{-1}$
u'	Velocity gradient in the laminar-sub layer	$m \cdot s^{-1}$
V	Volume	ml or l or m^3
$\mathbf{V_g}$	Generation rate of hydrogen gas at the cathode (volume basis)	$l \cdot min^{-1}$
v	Electrophoretic speed of the particle	$\mu m \cdot s^{-1}$ or $m \cdot s^{-1}$
W	Weight	g
$\mathbf{w_g}$	Generation rate of hydrogen gas at the cathode(molor basis)	$mol \cdot s^{-1}$
X	Valve	
X_A	Valve for gas releasing	
X_B	Valve for by-pass stream	
X_D	Valve for drainage	
X_{per}	Valve for permeate	
X_R	Valve f or retentate	
x	Distance	mm or m
$\mathbf{x_c}$	Critical distance after which the flow pattern becomes fully developed turbulent flow	mm or m
y	Distance above the membrane surface	mm or m
Ψ	Porosity of Alamin powder	
β	Contact angle between liquid and solid	Degree(°)
ε	Gap between the central bar and the membrane	mm or m
ρ_w	Density of fluid (water)	$kg \cdot m^{-3}$
ρ_p	Density of the particle	$kg \cdot m^{-3}$
ϕ	Shape coefficient of particle, i.e. for a spherical object, $\phi=6\pi$	
γ	Surface tension of liquid	$N \cdot m^{-1}$
δ	Thickness of flow boundary layer	μm
δ_b	Thickness of laminar sub-layer	μm
μ	Viscosity	Pa·s